INFORMATION TO USERS

This manuscript has been reproduced from the microfilm master. UMI films the text directly from the original or copy submitted. Thus, some thesis and dissertation copies are in typewriter face, while others may be from any type of computer printer.

The quality of this reproduction is dependent upon the quality of the copy submitted. Broken or indistinct print, colored or poor quality illustrations and photographs, print bleedthrough, substandard margins, and improper alignment can adversely affect reproduction.

In the unlikely event that the author did not send UMI a complete manuscript and there are missing pages, these will be noted. Also, if unauthorized copyright material had to be removed, a note will indicate the deletion.

Oversize materials (e.g., maps, drawings, charts) are reproduced by sectioning the original, beginning at the upper left-hand corner and continuing from left to right in equal sections with small overlaps.

Photographs included in the original manuscript have been reproduced xerographically in this copy. Higher quality 6" x 9" black and white photographic prints are available for any photographs or illustrations appearing in this copy for an additional charge. Contact UMI directly to order.

Bell & Howell Information and Learning
300 North Zeeb Road, Ann Arbor, MI 48106-1346 USA
800-521-0600

HARVARD UNIVERSITY
Graduate School of Arts and Sciences

THESIS ACCEPTANCE CERTIFICATE

The undersigned, appointed by the

Division

Department of Physics

Committee

have examined a thesis entitled "Micro-Electromagnets for Particle Control"

presented by Marija Drndic

candidate for the degree of Doctor of Philosophy and hereby certify that it is worthy of acceptance.

Signature .....

Typed name .....Robert M. Westervelt, Chair.....

Signature .....

Typed name .....Michael Tinkham.....

Signature .....

Typed name .....Eric J. Heller.....

Date .....May 18, 2000.....

Micro-Electromagnets

for Particle Control

A thesis presented

by

Marija Drndic

to

The Department of Physics

in partial fulfillment of the requirements

for the degree of

Doctor of Philosophy

in the subject of

Physics

Harvard University

Cambridge, Massachusetts

May, 2000

UMI Number: 9972301

Bell & Howell Information and Learning Company
300 North Zeeb Road
P.O. Box 1346
Ann Arbor, MI 48106-1346

Micro-electromagnets for Particle Control

Robert M. Westervelt Marija Drndic

ABSTRACT

Micro-electromagnets were developed to control particle motion in electromagnetic field landscapes in vacuum near microfabricated surfaces. We describe the design and fabrication of atom mirrors (serpentine wire patterns), and traps (circular wire patterns). We also describe single and coupled three-dimensional (3D) traps, integrated 3D trap with a mirror and 3D guides for neutral particles in vacuum. Planar micro-electromagnets consist of micron-scale Au wires on sapphire substrates fabricated using photo-lithography and electroplating. Three-dimensional (3D) micro-electromagnets consist of multiple layers of micron-scale conductors separated by transparent insulators to create particle containers with deep, symmetric and time-dependent potentials, suitable for integration in quantum circuits with particles. Micro-electromagnets permit high currents ($10^8 A/cm^2$) and magnetic fields (0.3 T) with gradients $|\nabla B| \sim 10^3$ T/cm. Electrical conductor and substrate materials were chosen for their electrical and thermal properties. Devices were cooled to cryogenic temperatures and typically operated in a pulsed mode to reduce the average heat dissipation. Micro-electromagnet mirrors were used to deflect a thermal beam of metastable helium (He*) atoms at small (mrad) angles. The spatial distributions of deflected He* atoms were measured as functions of atom-mirror separations and mirror currents. Time-dependent mirror fields were used to compensate for the broadening of the deflected peaks due to the spread in atomic velocities and to narrow the peak distributions. The measured results agree well with numerical simulations. We also describe the use of micro-electromagnet mirrors to reflect a cloud of free-falling Rb atoms at normal incidence.

The fluorescence from the reflected cloud, dropped from a magneto-optical trap, was imaged and its size was measured as a function of mirror current. This experiment confirmed the nontrivial dependence of mirror specularity on mirror current and on mirror geometry: the measured corrugations reached a local minimum at an optimal finite current and mirrors with an odd number of wires are smoother than mirrors with even number of wires. Mirror specularity of ~ 10 mrad was achieved. Future improvements are discussed. Micro-electromagnets can be also used to manipulate charged particles. Micro-electromagnet traps for electrons in vacuum are proposed, and possible approaches to trap and detect electrons in small volumes are discussed.

ACKNOWLEDGMENTS

The past few years have been a time of learning and creating. I have been fortunate to be around exceptional people who have helped this work come true. I would like to use this opportunity and say thank you:

To my mentor, Prof. Robert Westervelt, for giving me freedom to define my own research directions, for his guidance to realize my goals, and for creating a supportive work environment. To Prof. Eric Heller and Prof. Mike Tinkham for being on my committee. To many Westervelt group students and alumni: Aram Adourian, Catherine Crouch, Junmin Hu, and Jordan Katine, who helped me with the experimental work, and shared their experiences with me in the first few months when I joined the group. To Mark Eriksson, Carol Livermore and Rex Beck who have, as more experienced group members, provided useful guidance in the following years of my Ph.D. Special thanks go to the Westerveltians who overlapped with me most: Mark Topinka and David Duncan for many stimulating discussions and help, Lester Chen for his help and teamwork in the last year of my Ph.D., and to Chungsok Lee for our enjoyable work together in the last two years of the micro-electromagnet project. I would also like to thank Ian Chan and Brian Leroy, who joined our group recently, for reinforcing my enthusiasm.

Special thanks go to Kent Johnson for working on the helium deflection experiment and for useful advice during my Ph.D. work. To Prof. Mara Prentiss and her students Joseph Thywissen, Gary Zabow and Nynke Dekker for our fruitful work together. To Prof. Alain Aspect and his group including Paul Featonby, Laurent Cognet, Veronique Savalli, Nathalie and Chris Westbrook for working with me on the reflection experiment and for their hospitality in Paris. To Bill Phillips for useful discussions of micro-electromagnets. To Prof. Mike Tinkham and his research group including Dolores Bozovic, Jeanie Lau, Drago Davidovic, Sarah Pohlen, Alexey Bezryadin and Mark Bockrath for making the second floor of the McKay Lab a lively and friendly place to be.

Special thanks go to Steve Shepard for his expertise and generous help with fabrication. To Joe Tien from Prof. Whitesides group for helpful suggestions regarding electroplating, and to Steve Peil from Prof. Gabrielse group for Penning trap discussions, help with electroplating and for taking an active interest in my work. To David Goldhaber-Gordon for inspiring discussions in the last year of my Ph.D. To Louis DeFeo and David Osier for machining the cryogenic equipment and for their useful suggestions. To Prof. Isaac Silvera for generously providing us with valuable copper braids from Holland.

To my dear family, my parents Dasa and Ognjen and my stepfather Darko for their support and love, and to my aunt Beba for her generosity and care. To Vanja, for his endless love and humor. Special thanks to my grandparents Danica and Nikola for their understanding and wisdom. To my late grandfather Ante for conveying to me his enthusiasm about physics and mathematics.

I would also like to acknowledge the support from the Clare Booth Luce Fellowship in the first two years of graduate school.

TABLE OF CONTENTS

Chapter 1

INTRODUCTION

1.1 Micro-Electromagnets for Particle Manipulation in Vacuum

The control of particles in vacuum can be achieved on a microscopic scale using electromagnetic field patterns, opening possibilities ranging from integrated matter-wave optics and quantum dots in vacuum to quantum computation with cold gases of bosons and fermions. With advances in particle cooling techniques [Metcalf H., van der Straten P., 1994] and microfabrication of complex structures [*Nanostructures and Mesoscopic Systems* (eds. Kirk W.P. and Reed M.A.), 1992], it is now feasible to study the quantum transport of low-energy atoms, molecules, and electrons inside low-dimensional structures of size approaching their wavelength. The wavelength of cold atoms is $\lambda_{dB} = 3.1/\sqrt{AT}\,(\mu m\sqrt{\mu K})$ with atomic number A and temperature T. For Cs atoms λ_{dB}= 0.1μm at T = 10 μK is achievable in a magneto-optical trap. Quantum transport of electrons inside semiconductor and metal nanostructures has shown what is possible [*Mesoscopic Electron Transport* (eds. Sohn L.L, Kouwenhoven L.P., and Schon G.), 1996].

Recent progress in the field of neutral atom manipulation was stimulated by the development of laser-cooling techniques and microfabrication. Light-atom interactions were used to demonstrate reflection, diffraction, focusing and trapping of atoms [Adams C.S. *et al.*, 1994], while microfabrication techniques were used to construct structures with small enough periods to diffract thermal atom beams [Ekstrom C.R. *et al.*, 1992]. Advances have also taken place in the use of magnetic field gradients in novel manipulation schemes such as mirrors, gratings, traps [Midgall A.L *et al.*, 1985] and

lenses [Kaenders W.G. *et al.*, 1996]. Specifically, mirrors for atoms have been proposed [Opat G.I. *et al.*, 1992] and demonstrated using macroscopic permanent rare-earth magnets [Sidorov A. I. *et al.*, 1996], microscopic magnetic tapes [Roach T.M. *et al.*, 1995], and magnetized floppy discs [Hughes I.G. *et al.*, 1997a and 1997b]. The use of microscopic planar geometries for small atomic traps has been proposed [Weinstein J.D. and Libbrecht K.G., 1995].

Neutral atoms are interesting to study gravitational effects, general relativity and quantum mechanics [Adams C.S. *et al.*, 1994]. Atoms come in a range of masses and other properties. They have a complex internal structure which can be probed and can be used for non-destructive probing of surfaces, atom interferometry, atom optics and atom lithography. Atom optics refers to techniques to exploit the wave properties of neutral atoms just as conventional optics manipulates light. Atom optics can offer several advantages over other kinds of optics (photon, electron, ion, and neutron). Still, efficient and reliable atomic mirrors and other optical elements like lenses, beamsplitters and waveguides are required for many applications [Adams C.S. *et al.*, 1994].

Recently, several manipulation schemes for atoms above planar microstructures have been suggested [Reviewed in: Hinds E.A., Hughes I.G., 1999]. Quantum wires and quantum dots for atoms have been proposed using planar structures [Schmiedmayer J., 1998]. Microstructures realized experimentally during the course of this research include planar micro-electromagnet atom mirrors [Drndic M. *et al.*, 1998; Johnson K.S. *et al.*, 1998; Lau D.C. *et al.*, 1999], micro-traps [Reichel J. *et al.*, 2000], atom guides [Dekker N.H. *et al.*, 2000; Muller D. *et al.*, 2000], and very recently, atom beamsplitters [Mueller D. *et al.*, 2000; Folman R. *et al.*, 2000]. It has been shown theoretically that the conductance of atom flow through microfabricated atom guides can be quantized [Thywissen J.H. *et al.*, 1999], analogous to electron flow in quantum point contacts [Van Wees B.J. *et al.*, 1988].

Charged particle mesoscopics in vacuum has also been advancing. Microtraps for ions modeled on Paul traps have been realized [Brewer R.G. *et al.*, 1992], and two-ion super- and subradiance has been observed [Devoe R.G. *et al.*, 1996]. Manipulation of electrons in vacuum for energies $E > 1$ eV has been realized for micro-vacuum tubes and flat panel displays [See for review: Brodie I. and Schwoebel P.R., 1994]. Many possibilities still remain to manipulate cold electrons. Electrons with lower energy confined in small volumes will permit study of low-dimensional gases in vacuum, minimizing interference from the substrate.

1.2 Overview of The Thesis

Chapter 2 describes the physical principles behind the neutral atom manipulation using magnetic fields, and introduces micro-electromagnets as new tools to control the particle motion. Chapters 3 and 4 describe the design, fabrication and properties of micro-electromagnets including atom mirrors, traps, and guides. The following two Chapters (5 and 6) concentrate on two experiments to deflect and reflect He and Rb atoms using micro-electromagnet mirrors. In Chapter 5 we show measurements to deflect atoms at grazing angles and describe how time-dependent mirror fields were used to narrow the angular distributions of the deflected He beams. The mirror properties as reflectors of cold Rb atoms are discussed in Chapter 6. The specularity of micro-electromagnet mirrors has been studied and nontrivial dependence of mirror corrugations on mirror current and on mirror geometry was confirmed. In Chapter 7, we describe the design and fabrication of three-dimensional micro-electromagnets that can produce deeper traps with larger field gradients and energy level spacing, spatially-symmetric potentials and could be integrated in quantum circuits for particles. In Chapter 8 we illustrate how micro-electromagnets could also be used for manipulation of charged

particles, including a way to realize electron traps and detect trapped electrons in vacuum.

Chapter 2

THE PHYSICS OF NEUTRAL ATOM MANIPULATION

Micro-electromagnets consist of current-carrying wires and produce magnetic field configurations which can be used to create optical elements for atoms. By tailoring the wire patterns, magnetic fields above the wires can be made intricate for a variety of manipulation schemes. In this Chapter we describe the control of neutral atoms using current-carrying wires, based on the magnetic-dipole interaction and the adiabatic following of the field by the atomic magnetic moment. The wire patterns to reflect, trap and guide atoms are introduced.

2.1 Magnetic-Dipole Interaction

The interaction of atoms with magnetic fields for neutral atom optics has been studied in detail [Migdall A.L. *et al.*, 1985]. The manipulation of atoms using current-carrying wires is based on the linear Zeeman interaction between an inhomogeneous magnetic field and the atomic magnetic dipole moment. This manipulation scheme can avoid spontaneous emission that occurs in atom optics based on light-atom interactions.

The interaction potential is

$$U(x,y,z) = -\vec{\mu} \cdot \vec{B}(x,y,z), \tag{2.1.1}$$

where $\vec{B}$ is the magnetic field, $\vec{\mu} = -g_F \mu_B \vec{J}$ is the atomic magnetic moment, $\vec{J}$ is the angular momentum, μ_B is the Bohr magneton, g_F is the Landé g-factor, and m_F is the magnetic quantum number of the atomic sublevel. If the magnetic moment can follow the changes in the local magnetic field, the motion is adiabatic and the external field

affects only the center of mass motion. In this regime, m_F is a constant of motion, and the gradient force due to the magnetic field is

$$\vec{F} = \nabla(\vec{\mu} \cdot \vec{B}) = -g_F m_F \mu_B \nabla B. \tag{2.1.2}$$

Weak-field seeking particles ($m_F g_F > 0$) are repelled by increasing B-field gradients and attracted to B-field minima, high-field seeking particles ($m_F g_F < 0$) are attracted to B-field maxima, and $m_F g_F = 0$ particles will be unaffected by the field.

For strong magnetic fields, one must consider both the linear Zeeman potential (Eqn. (2.1.1)) and the quadratic Zeeman potential expressed by the Breit-Rabi formula

$$U(x,y,z) = g_F m_F \mu_B B + (F^2 - m_F^2)(g_F \mu_B B)^2 / (\hbar \Omega_{hf}), \tag{2.1.3}$$

where $\Omega_{hf} / 2\pi$ is the frequency between the hyperfine ground states. In this case, the $m_F = 0$ states can be manipulated. Dynamic manipulaton of high-field seeking particles ($m_F g_F < 0$) is also possible using time-dependent magnetic fields [Weinstein J.D. and Libbrecht K.G., 1995]. Most of the discussion in this thesis is limited to the linear Zeeman interaction and static magnetic fields.

The interaction potential $U(x,y,z) = g_F m_F \mu_B B$ depends on the magnitude B of the magnetic field. The magnitude B can be tailored to achieve a particular manipulation scheme such as reflection, trapping or guiding, by designing the wire geometry and the current distribution correspondingly.

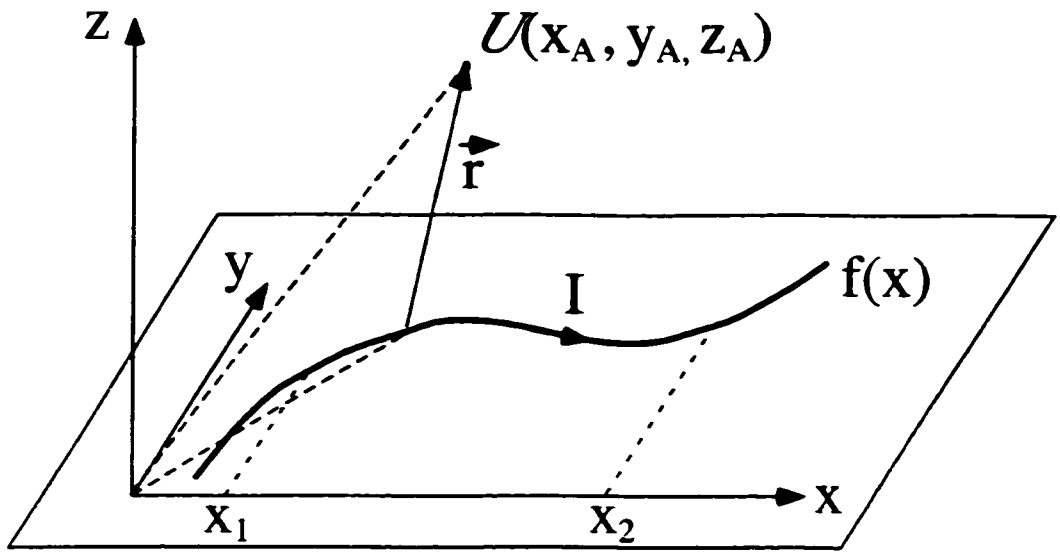

FIG. 2.1 Schematic of a planar wire pattern carrying current I. The wire pattern can be defined as a function $y = f(x)$ in some interval (x_1, x_2). The interaction potential U at some point A in space with coordinates (x_A, y_A, z_A) is given in Eqn. (2.1.4).

The magnetic field magnitude B and the interaction potential U can be calculated above an arbitrary wire pattern as described below. Figure 2.1 illustrates a planar wire pattern, carrying current I with the current direction as indicated. This wire pattern can be defined as a function $y = f(x)$ in some interval (x_1, x_2). The interaction potential at some point A in space with coordinates (x_A, y_A, z_A) will be given by

$$U(x_A, y_A, z_A) = (\mu_o / 4\pi) g_F m_F \mu_B I[(\int_{x_2}^{x_1} dx z_A f' / r^3)^2 + (\int_{x_2}^{x_1} dx z_A / r^3)^2 +$$

$$+ (\int_{x_2}^{x_1} dx [y_A - f - f'(x_A - a)] / r^3)^2]^{1/2}, \qquad (2.1.4)$$

where $f' = df(x)/dx$, and $r = [(y_A - f(x))^2 + (x_A - x)^2 + z_A^2]^{1/2}$. For a particular potential configuration $U(x,y,z)$, this equation defines the constraints on the wire geometry.

2.2 Adiabatic Condition

Adiabatic following of the magnetic field is necessary for the control of neutral particle motion using micro-electromagnets [Opat G.I. *et al.*, 1992]. As discussed in the previous section, the field magnitude (not direction) controls the trajectory of atoms in the adiabatic regime. If the particle is moving slowly enough compared to the rate of change of the direction of the magnetic field, the transition probability between the different magnetic sublevels is suppressed and the magnetic quantum number m_F remains constant.

This adiabatic following is illustrated in Fig. 2.2 with a magnetic moment, which processes around the local magnetic field lines. The projection of $\vec{\mu}$ onto $\vec{B}(x,y,z)$, i.e., the angle $\alpha = \angle(\vec{\mu}, \vec{B})$ between the magnetic moment and the magnetic field, is a constant of motion.

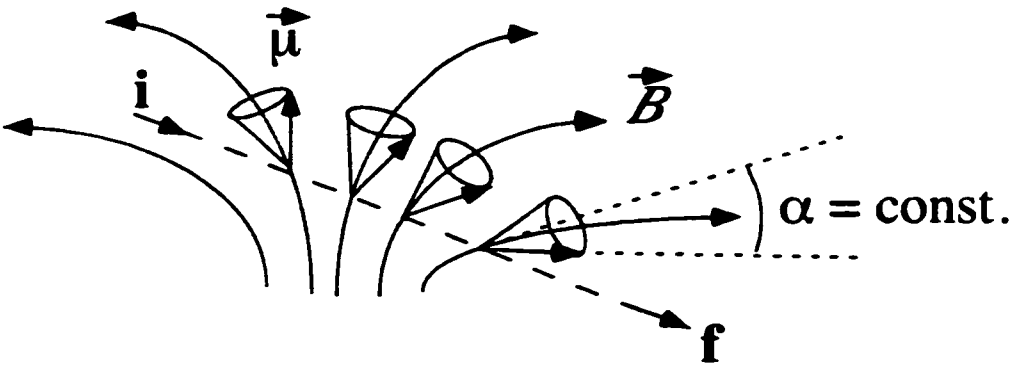

FIG. 2.2 Schematic diagram of atomic trajectory through the magnetic field $\vec{B}$ from the initial (i) to the final (f) position and the procession of the magnetic moment around the local field lines.

The adiabatic condition can be expressed as

$$\omega_{ij} << \partial \hat{e}_B / \partial t , \tag{2.2.1}$$

where ω_{ij} is the transition frequency between magnetic sublevels, $\hat{e}_B = \vec{B}/|\vec{B}|$ is the unit vector of the magnetic field $\vec{B}$, and $\partial \hat{e}_B / \partial t$ is the rate of change of the direction of the magnetic field.

In the experiments, a small background field should be added when operating micro-electromagnets to avoid $B = 0$ points when $\vec{\mu}$ can lose its orientation, and to ensure that the inequality (2.2.1) holds for all points in space. The inequality (2.2.1) imposes constraints which relate the atomic velocity v to a characteristic dimension a of the wire geometry and the magnitude of the background field B_{bg}. This is discussed in more detail for micro-electromagnet mirrors in the section 2.3 (Eqn. (2.3.4)).

The adiabatic condition can be understood in more detail by following the evolution of the atomic wave function described by Schrodinger's equation. The Hamiltonian is $H = T + U_{int}(x,y,z)$, where T is the kinetic energy operator, and

$U_{int}(x,y,z)$ is the interaction potential between the magnetic moment and the static position-dependent magnetic field. The atomic wave-function $|\psi\rangle$ describes both the internal state and external motion of the atomic ensemble and can be written as a vector product $|\psi\rangle = \sum_n |C_n\rangle \otimes |n\rangle$, where $|C_n\rangle$ is the center of mass and $|n\rangle$ the internal wavefunction of state n. While the kinetic energy operator is diagonal, the potential energy operator may have non-diagonal elements, which can lead to interstate transitions. Ideally, the magnetic field should change only the external motion of atoms. The problem would be significantly simplified if the internal motion and the external motion can be separated. If one chooses the vector basis where $U_{int}(x,y,z)$ is diagonal (unitary transformation), then the kinetic energy operator contains non-diagonal elements (in this new basis) giving rise to transitions between eigenstates. However, if the time dependence of the magnetic field (from the reference frame of moving atoms) is slow compared to the characteristic time scale for the internal evolution, the off-diagonal elements may be neglected and the magnetic dipole will adiabatically follow the changing direction of the field.

2.3 Micro-electromagnet Configurations (Mirrors, Traps, and Guides)

In this section, we introduce the planar wire geometries and magnetic field configurations that can be used to reflect (Fig.2.3), guide (Fig.2.4) and trap (Fig.2.5) atoms and other neutral particles with spin above a chip.

Figure 2.3 (a) shows a schematic diagram of the magnetic mirror for atoms. This mirror was first proposed for neutrons by [Vladimirskii V. V., 1961]. It is a serpentine pattern or an array of parallel wires alternatively carrying currents in opposite directions. Figure 2.3 (b) shows the cross-sectional view of the mirror wires on a flat substrate, together with the current in the wires, and the magnetic field lines above the wires, as indicated. The x-direction is defined in the plane of the mirror and perpendicular to the wires; the z-direction is defined perpendicular to the plane of the mirror with the origin $z = 0$ defined at the top of the wires. The characteristic size of the mirror is the mirror period a, which is the distance between two wires carrying currents in the same direction (Fig.2.3 (b)). The mirror surface is defined as the surface of the wires and the substrate. A background field $\vec{B}_{bg}$, perpendicular to the mirror field, is added along the y-direction (Fig. 2.3 (b)) to ensure adiabaticity, as previously discussed in section 2.2.

The contours of constant magnetic field magnitude B above an infinitely large mirror are shown in Fig. 2.3 (c). For such an ideal mirror with an infinite number of infinitely long wires, the magnitude B of the magnetic field decays exponentially in the direction perpendicular to the mirror plane, with characteristic length $1/k = a/2\pi$, where a is the period (see Fig. 2.3 (b)).

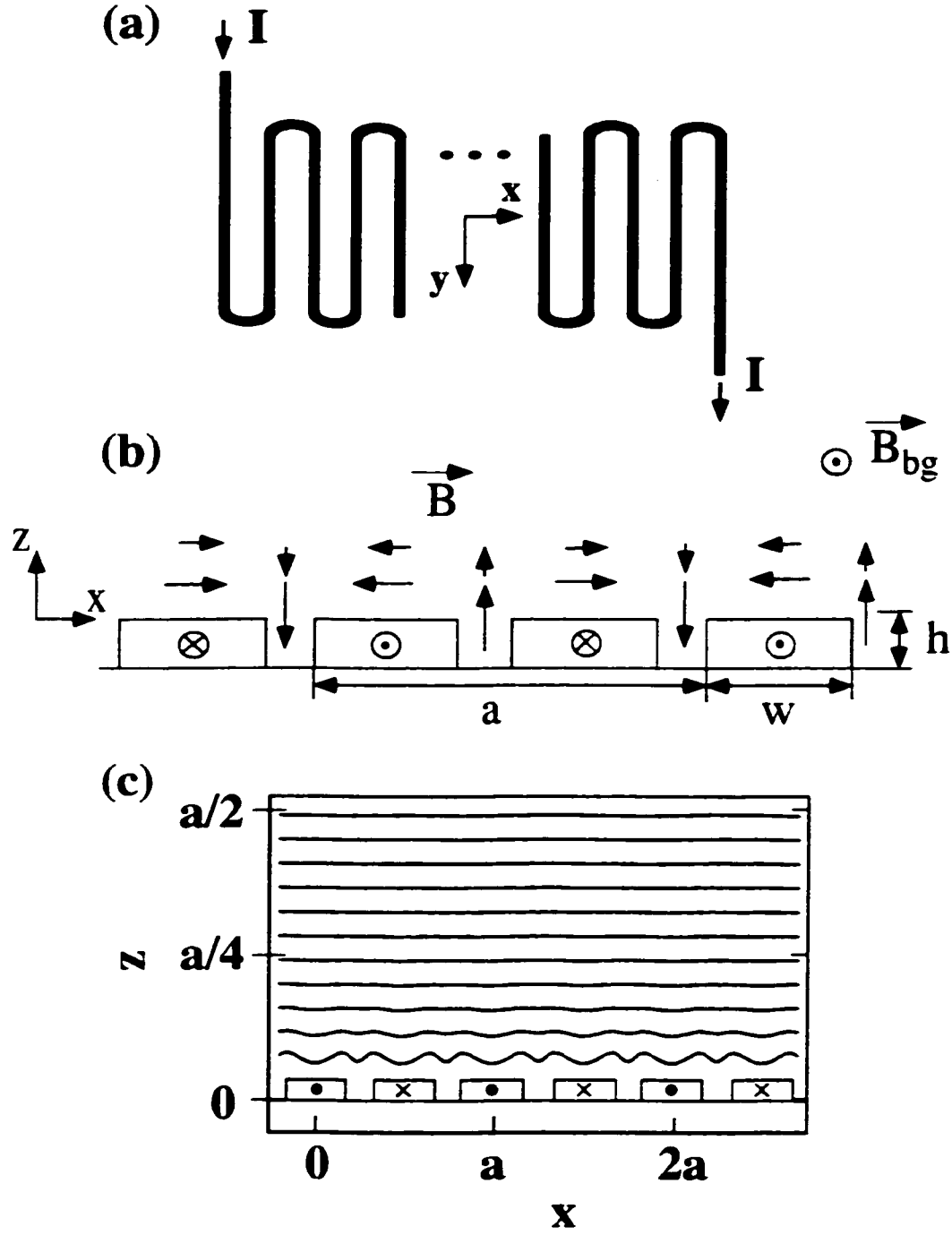

FIG.2.3 Micro-electromagnet mirror for atoms: (a) schematic diagram of a serpentine wire geometry. (b) Cross-sectional view of the wires with the current direction and magnetic field lines indicated; a background magnetic field $\vec{B}_{bg}$ is added perpendicular to the mirror field to ensure adiabaticity. (c) Contours of constant magnetic field magnitude B above a center of an infinitely large mirror. I is the mirror current and a is the mirror period. Subsequent contours, equally spaced in the z-direction, are in the ratio B_{n+1}/B_n = 0.8, where n = 1 to 11. Atoms in weak field seeking states are reflected elastically from high fields near the mirror.

At distances $z >> a/2\pi$ from the mirror surface, the magnitude of the B-field can be expanded in Fourier components [Sidorov A.I. *et al.*, 1996; Drndic M. *et al.*,1998]

$$B(x,z) = \varepsilon_o I e^{-kz}[1 + \varepsilon_1 e^{-2kz}\cos 2kx + \varepsilon_2 e^{-4kz}\cos 4kx + ...], \quad (2.3.1)$$

where ε_o, ε_1 , and ε_2 are coefficients determined by wire shape and spacing. The x and z components of B that contribute to the first, leading term $B(x,z) = \varepsilon_o I e^{-kz}$ in Eqn. (2.3.1) are

$$B_x(x,z) = \varepsilon_o I e^{-kz}\cos 2kx, \text{ and} \quad (2.3.2a)$$

$$B_z(x,z) = \varepsilon_o I e^{-kz}\sin 2kx. \quad (2.3.2b)$$

Thus, at a given height $z = h$, the field $\vec{B}$ rotates in the xz plane (Fig. 2.3 (b)) with a constant magnitude. Because the contours of constant B are planes parallel to the mirror surface, the gradient force will be perpendicular to the mirror plane. Therefore, the weak field seeking atoms will be specularly and elastically reflected from high fields near the mirror.

The magnetic field at the surface of the wires is not uniform. However, for practical purposes we can talk about the surface field and define it as the field at the middle of the top of the wire (Fig.2.3 (b)):

$$B_o = B(x = 0, z = 0) = \alpha I, \quad (2.3.3)$$

where $\alpha = \varepsilon_o (1+\varepsilon_1 + \varepsilon_2 + ...)$ is a proportionality factor between the surface field and the mirror current.

The specularity of micro-electromagnet mirrors is determined by the flatness of the magnetic field contours shown in Fig.2.3 (c). Corrugations in the magnetic field contours (Fig.2.3 (c)) cause the atomic reflection to deviate from specular. For an infinitely large mirror, the mirror corrugations decrease monotonically with distance from the mirror surface. At distances $z >> 1/k$, the mirror is almost perfectly smooth. For atoms of a given energy, the reflection will also be more specular as the mirror current is increased, because they are reflected further above the mirror, where the corrugations are smaller. Close to the mirror surface, the size of corrugations depends on the coefficients $\varepsilon_1, \varepsilon_2$ and the higher harmonics in Eqn. (2.3.1).

As shown in Fig.2.3 (b), a background magnetic field $\vec{B}_{bg}$ is added perpendicular to the mirror field to avoid points in space with $B = 0$ and to ensure adiabaticity. In the case of the mirror, the adiabaticity condition (2.2.1) can be expressed as a relation between the atomic velocity $\vec{v}$, the mirror period a, and the magnitude of the background field B_{bg}. A detailed discussion can be found in [Roach T.M.,1996]. and for an ideal infinite mirror, the condition (2.2.1) can be expressed as

$$\hbar k v / (\gamma g_F \mu_B B_{bg}) << 1, \tag{2.3.4}$$

where $\gamma \propto 1$ is a constant of order unity [Roach T.M.,1996]. If the atom approaches the mirror along x direction, at a constant distance z from the mirror, it sees a rotating field with a constant magnitude (see Fig. 2.3 (b)), and it can be shown that $\gamma = \sqrt{2}$. Similarly, if the atom approaches the surface along z at a constant x, then $\gamma = 2\sqrt{2}$.

A detailed discussion of micro-electromagnet mirror design follows in Chapter 3. Here, we outline two design consideration regarding the required magnitude of the surface field B_o and the mirror period a. The first consideration is the range of atomic wavelengths that can be reflected from the mirror given by $\lambda > \hbar / \sqrt{2mU_o}$, where m is the atomic mass, and $U_o = g_F m_F \mu_B B_o$ is the potential energy at $z = 0$. For example, for a

surface field B_o = 100 G, Rb atoms can be reflected at normal incidence if $\lambda > 0.6nm$ (v < 1 m/s). The fabricated mirrors described in Chapter 4 produce surface fields up to $B_o \approx$ 1000 G.

Another consideration in designing mirrors is the change of the phase of the atomic wavefunction during reflection from the mirror. The phase shift $\Delta\phi$ is proportional to the momentum p of incident atoms. From a semi-classical calculation the phase accumulated by an atom reflected due to the linear Zeeman effect is $\Delta\phi = -\pi/2 - (2ap/h)\cos\alpha_o$, where α_o is the angle of incidence from the normal [Sidorov A.I. *et al.*, 1996]. Consequently, mirrors with smaller periods (a) will cause smaller phase shifts.

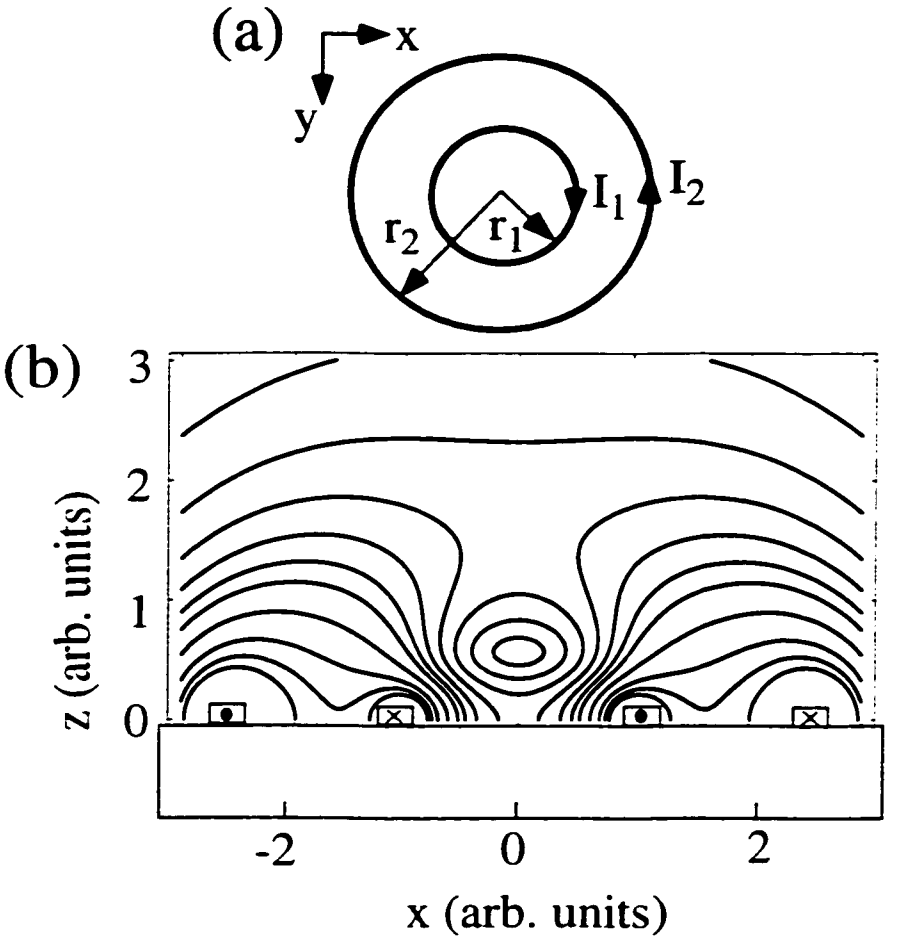

FIG.2.4 Micro-electromagnet quadrupole trap for atoms: (a) schematic diagram of two concentric current loops: (b) contours of constant magnetic field magnitude B above the wires. I_1 and I_2 are the currents and r_1 and r_2 are the radii of the inner and outer loops, respectively. Subsequent contours are spaced by an equal increment ΔB. The B-field minimum ($B = 0$) is formed along the z-axis and B increases linearly away from the trap center. Atoms in weak field seeking states are attracted to the region of minimum B-field in the trap center.

In the rest of this section, we describe the wire geometries to trap and guide neutral atoms. Figure 2.4 (a) shows a schematic diagram of a simple quadrupole magnetic trap for atoms consisting of two coaxial rings or radii r_1 and r_2, with opposing currents I_1 and I_2, suggested theoretically by [Weinstein J.D. and Libbrecht K.G., 1995]. This trap is a planar analogue of the anti-Helmoltz trap commonly used for particle trapping [see for review Phillips W.D.,1998]. The contours of constant magnetic field magnitude B above the quadrupole trap are shown in Fig. 2.4 (b). Fabrication and properties of these micro-electromagnet traps are presented in Chapter 4. We have made traps with depths $B_{max} \sim 100$ G, which corresponds to atomic temperatures $T \sim 10$ mK, and energy level separation $\Delta E \sim 10$ μK.

Other types of traps such as Ioffe and the hexapole traps can be formed by circular wire geometries [Weinstein J.D. and Libbrecht K.G., 1995]. These traps could be used to confine small numbers of cold atoms to regions with dimensions comparable to the de Broglie wavelength. Large arrays of traps, as well as nested series of traps can be fabricated. Such structures could be used to capture atoms in a large volume and then compress them to a much smaller volume.

Micro-electromagnet atom guides have been theoretically suggested by [Thywissen J.H. *et al.*, 1999]. Figure 2.5 (a) shows a schematic diagram of a simple quadrupole magnetic guide consisting of two pairs of straight wires with dimensions r_1 and r_2, and currents I_1 and I_2 as indicated. The contours of constant magnetic field magnitude B above the wires are shown in Fig. 2.5 (b). Similarly to the quadrupole traps (Fig. 2.4 (a)), the B-field minimum ($B = 0$) is formed at a height $z = \sqrt{r_1 r_2 (I_1 r_2 - I_2 r_1)/(I_2 r_2 - I_1 r_1)}$ above x = 0, along the y-direction (Fig.2.5 (b)), and B increases linearly away from the trap center. These guides have been fabricated and used to guide cold Cs atoms along channels 1cm long and ~100 μm wide [Dekker N.H., 2000].

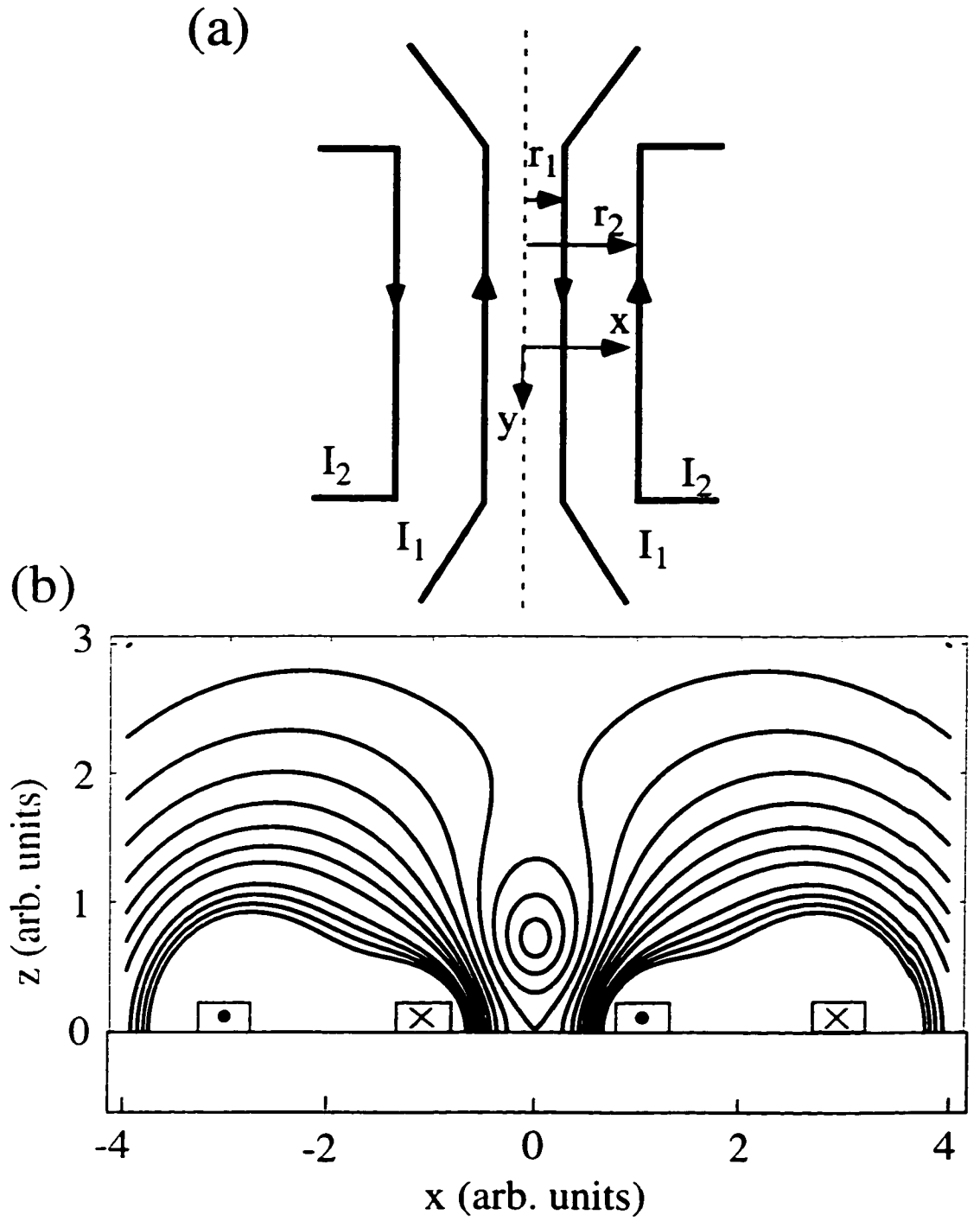

FIG.2.5 Micro-electromagnet quadrupole guide for atoms: (a) schematic diagram of two pairs of straight conductors; (b) contours of constant magnetic field magnitude B above the wires; I_1 and I_2 are the currents and r_1 and r_2 are wire separations from x=0, as indicated. Subsequent contours are spaced by an equal increment ΔB. Atoms in weak field seeking states are attracted to the region of minimum B-field.

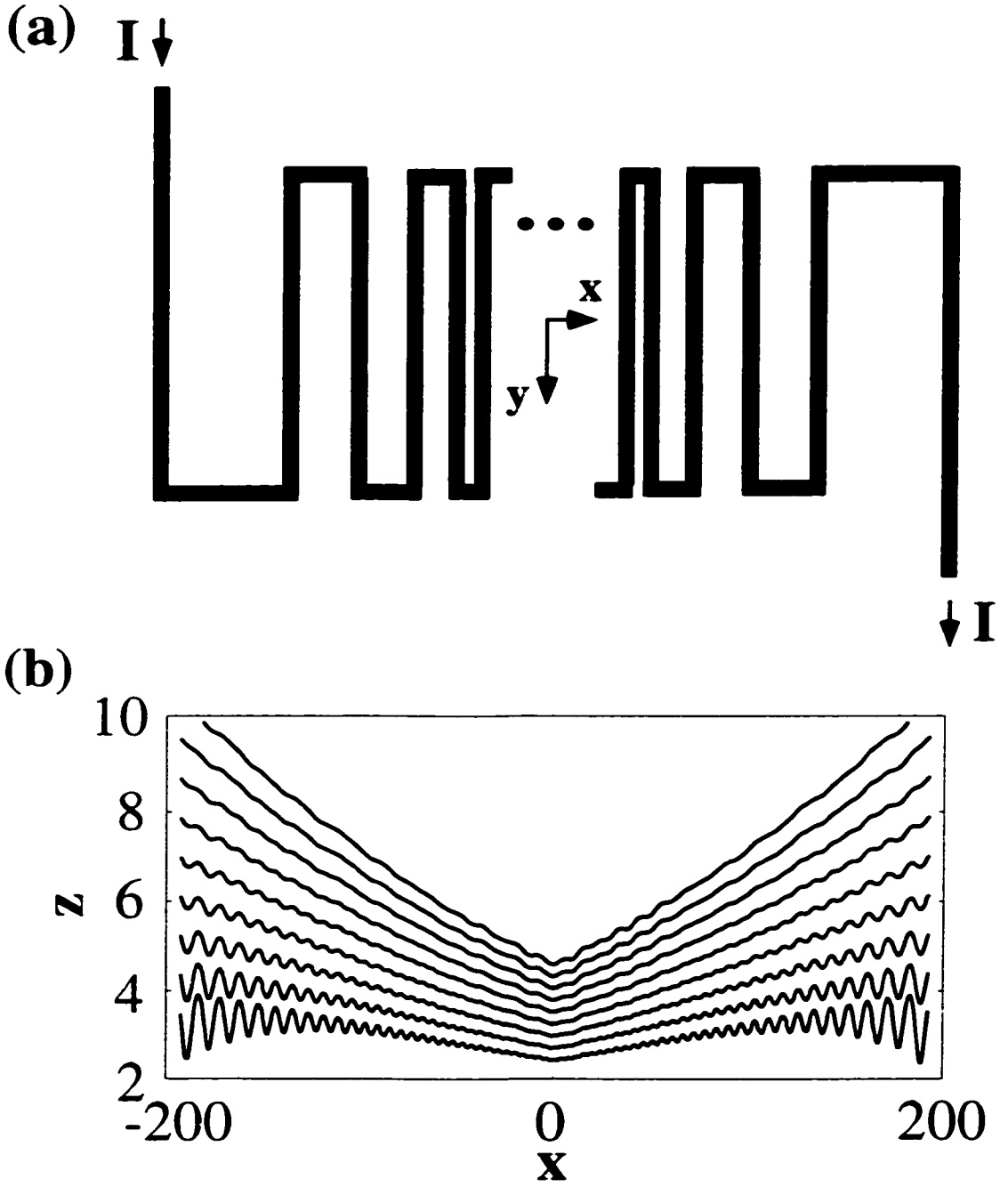

FIG. 2.6 Micro-electromagnet focussing mirror for atoms: (a) schematic diagram of a serpentine wire pattern with periodicity increasing from the center to the mirror edges; (b) contours of constant magnetic field magnitude B above the curved mirror with total number of wires $N = 87$ in the range $x = \pm 624$. Subsequent contours are spaced are in the ratio $B_{n+1}/B_n = 0.8$. In this example, the wire positions are $x_k = \pm [165 \log(|k|) - 624]$, $k = 1$ to 43, $x_o = 0$; the wire separations $a/2$ span from 3.4 in the center to 114.4 at the edge of the mirror. The magnetic field profile above the central 61 wires is included in the plot. I is the mirror current.

More elaborate planar wire geometries can be constructed from the basic designs discussed above, including atom beamsplitters, interferometers, and focusing mirrors. Varying the wire spacing across the width of the mirror adds a focusing capability to the micro-electromagnet mirrors, as illustrated in Figure 2.6 (a). In this case, the contours of constant magnetic field magnitude are curved surfaces, as shown in Fig. 2.6 (b). A beamsplitter can be realized by modifying a guide in Fig. 2.5 (a), as recently demonstrated by [Mueller *et al.*, 2000; Folman R. *et al.*, 2000].

Micro-electromagnets can be parts of an atomic circuit on a chip. Micro-electromagnet mirrors, traps and guides can be integrated both horizontally along the chip and vertically above a chip to achieve more complex structures. In Chapter 7 we describe three-dimensional (3D) micro-electromagnets including single and coupled 3D traps, 3D guides and integrated devices. The basic principles of operation are these described above.

In summary, in this Chapter we have described how to realize micro-electromagnets for atom manipulation using microfabricated current-carrying wires. The control of atom motion is achieved by exploiting the Zeeman interaction potential between the atomic magnetic moment and the magnetic field produced by the wires. For this control to work, the adiabatic condition has to be satisfied. Namely, the magnetic field should change the center of mass motion, but should not affect the internal state of the atom. We have described the wire geometries and corresponding magnetic field configurations to reflect, trap and guide atoms. Micro-electromagnet mirrors consist of serpentine wire geometries and produce magnetic fields whose magnitude falls off exponentially away from the mirror surface presenting a means to reflect particles with magnetic moments. Micro-electromagnet traps and guides produce magnetic fields to confine atoms in small volumes around the magnetic field minima. In the following Chapters 3 to 6 we will discuss in more detail the design of micro-electromagnet mirrors and the experimental results to deflect and reflect atoms using them.

Chapter 3

DESIGN OF MICRO-ELECTROMAGNET MIRRORS

In this Chapter we describe the modeling of realistic, finite-size atom mirrors. Unlike the magnetic field configuration above the ideal, infinitely large mirrors, described in Chapter 2, the magnetic field configuration above the finite-size mirrors depends nontrivially on the wire geometry. Two factors can significantly affect the magnetic field configuration: (*i*) the finite size of the mirrors, including the finite number of wires and the finite length of the wires (described in sections 3.1 through 3.4), and (*ii*) the cross-sectional profile of the wires (described in section 3.5). In section 3.1 we show that the specularity of finite mirrors is optimal at a finite height above the wires. Micro-electromagnet mirrors with an odd number of wires are more specular than mirrors with an even number of wires (section 3.2). Section 3.3 describes the magnetic field configuration close to the edges of a finite mirror. The magnetic field produced by the finite-size mirrors can be compensated with additional wires to mimic the magnetic field above an ideal, infinitely large mirror (section 3.4). Finally, in section 3.5 we describe the importance of the cross-sectional wire profiles to make high quality mirrors.

3.1 Magnetic field configuration above finite-size mirrors

In this section, we describe the magnetic field configuration above micro-electromagnet mirrors with a finite number of wires in the serpentine wire array. In particular, we show that specularity of finite mirrors is optimal at a finite height above the wires, and describe how to estimate the angular deviation from specular reflection for atoms reflecting off the mirror at normal incidence.

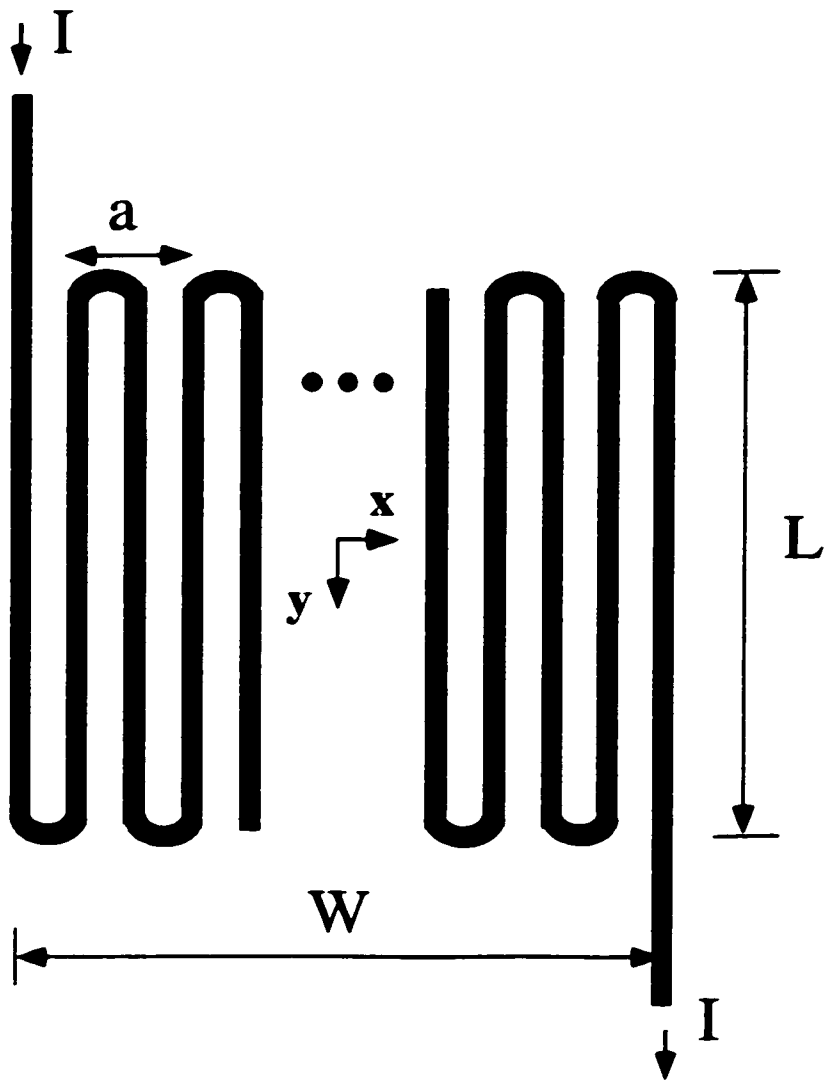

Fig.3.1 Schematic diagram of a finite micro-electromagnet mirror with period a, and current I. The x-direction is in the plane of the mirror and perpendicular to the wires, the y-direction is parallel to the wires. The mirror center is at $x = 0$, $y = 0$. The mirror width is W, and the length of the wires in the mirror array is L.

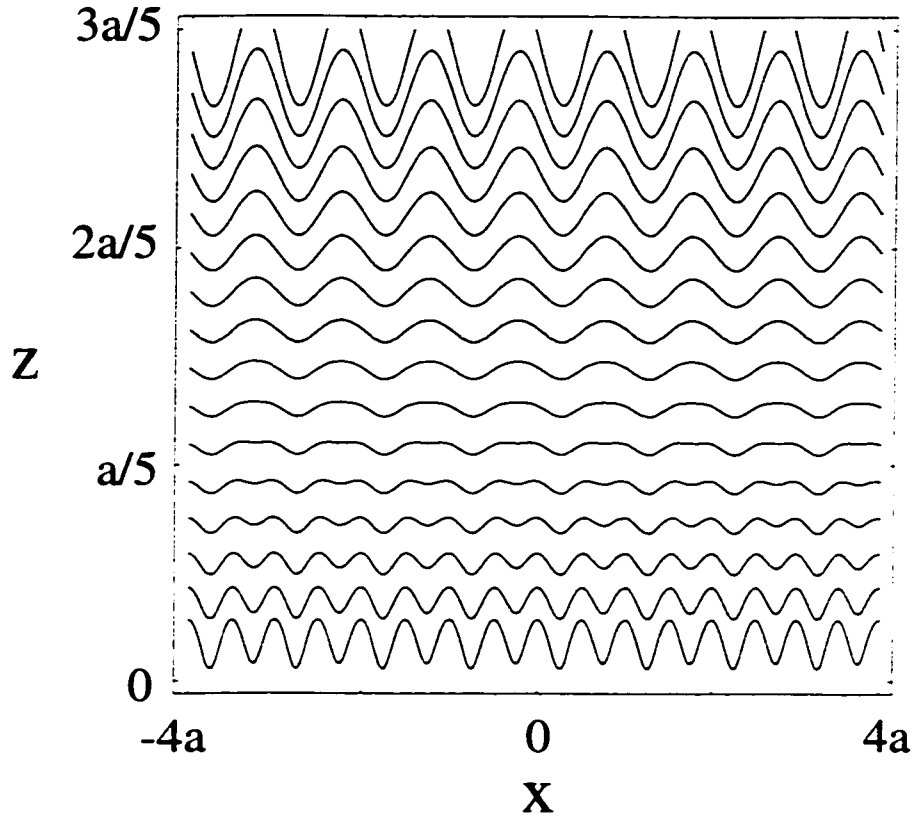

Fig.3.2 Contours of constant magnetic field B above the center of a mirror with 84 wires; the mirror current is I and wire separation is $a/2$; the wires are assumed to be cylindrical. Subsequent contours are in the ratio $B_{n+1}/B_n = 0.8$, where $n = 1$ to 16. For a mirror with $a = 50$ μm and area 2 x 2 mm^2 (see Chapter 4), the achieved field at the mirror surface (defined in Eqn. 2.3.3, Chapter 2) is $B_o \sim 0.1$ T. Corrugations in the magnetic field contours cause non-specular reflection. For a finite number of wires, the effect of end wires on the mirror corrugations is felt at heights near $z_o = \ln(N)/k$, $k = 2\pi/a$. In contrast, for an infinitely large mirror the corrugations decrease with increasing distance above the mirror (see Fig.2.3, Chapter 2).

Figure 3.1 shows a schematic diagram of a realistic, finite-size micro-electromagnet mirror with period a, mirror width W, and the length L of the wires in the serpentine array. The x-direction is defined perpendicular to the wires, and the y-direction is parallel to the wires. The mirror center is at $x = 0$, $y = 0$, and the mirror edge runs along $x = \pm W/2$ and $y = \pm L/2$; $z = 0$ is defined as the height above the top of the wires. The mirror surface is defined as the surface of the wires and the substrate.

Figure 3.2 shows the computed contours of constant magnetic field magnitude B (or equivalently, the equipotentials of the interaction potential U) above the center of a micro-electromagnet mirror with $N = 84$ wires.

For finite-size mirrors, the magnetic field contours exhibit interesting and nontrivial features at heights $z \sim a$ above the mirror. Because the B-field from an infinite array of wires decays exponentially[1], $B = 2\mu_o I / a e^{-kz}$, the effect of the end wires in a finite serpentine array is felt at a finite height above the mirror center $z_o \approx a/2\pi \ ln\ (N)$, where $B = 2\mu_o I/(\pi W)$ is the field produced by the end wires above the mirror center, and $W = (N\text{-}1)a/2$ is the mirror width. For example, for $N = 10^4$, $z_o \approx 1.5\ a$.

The specularity of micro-electromagnet mirrors is strongly affected by the finite-size of the mirrors. Deviations from specular reflection are caused by corrugations in the magnetic field contours. These contours deviate from perfectly flat lines parallel to the mirror surface. For an infinitely large micro-electromagnet mirror, the corrugations decrease monotonically in magnitude with the distance from the mirror (see Fig.2.3 (c) in Chapter 2). The mirror corrugations also decrease monotonically with increasing mirror current. This is because the height above a mirror at which atoms of a certain initial velocity are reflected is directly proportional to the mirror current I.

---

[1] Above the mirror center $B = \mu_o I / 2\pi \sum_{k=-\infty}^{\infty} (-1)^k z/[(ka/2)^2 + z^2] = 2\mu_o I / a e^{-2\pi z/a}$, which follows from the general equality $\sum_{k=1}^{\infty} (-1)^k /(k^2 + q^2) = 1/2q\ [2\pi/(e^{\pi q} - e^{-\pi q}) - 1/q]$ [Gradshteyn I. S. and Ryzhik I.M., 1994].

In contrast to mirrors with an infinite number of wires, the magnetic field contours for finite N in Fig. 3.2 best approximate straight lines at finite heights above the mirror near $z_o = \ln(N)/k$. This means that mirror corrugations are smallest for approximately the mirror current which gives a turning point in the region where the contours are most straight. The experimental observation of this optimal current is described in Chapter 6.

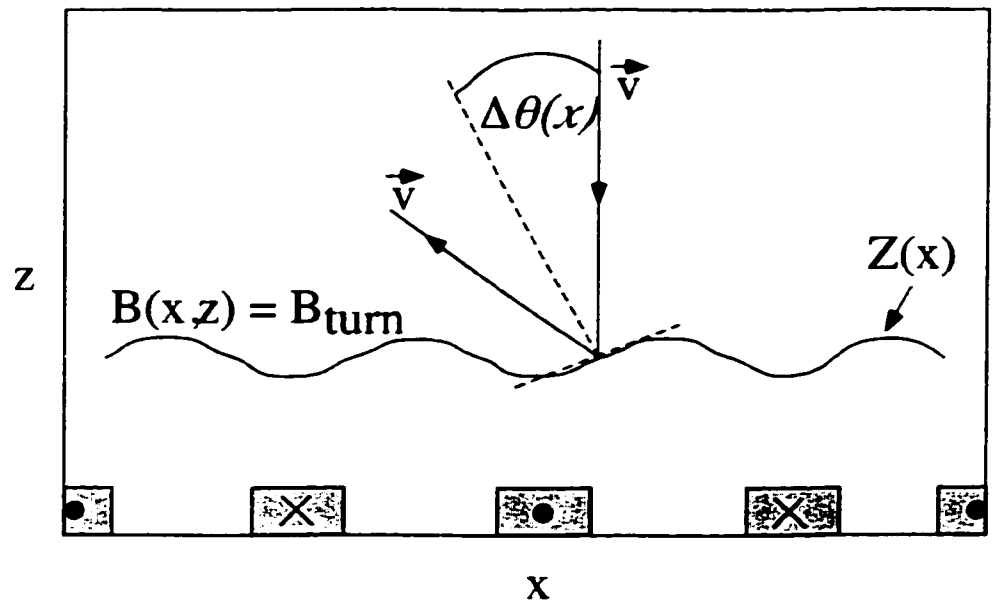

Fig.3.3 Schematic diagram of one magnetic field contour $B(x,z)=B_{turn}$ (see Eqn. (3.1.2)) at a turning point (Eqn. (3.1.1)) above a micro-electromagnet mirror, in a simple picture of atoms bouncing from a hard-wall potential. The magnetic field contour in the xz plane is defined explicitly as a function $Z(x)$. The incident atomic velocity $\vec{v}$ is normal to the surface. The angular deviation $\Delta\theta(x)$ from specular reflection is position-dependent and is given by $\Delta\theta(x) = Z(x)/dx$. The root-mean-square angular deviation can be estimated from Eqn. (3.1.4).

The angular deviation $\Delta\theta$ from specular reflection can be calculated for micro-electromagnet mirrors from the corrugations in the magnetic field contours. This calculation can be performed semi-classically by calculating the root-mean-square (rms) size of corrugations integrated along the atomic trajectory [Zabow G. *et al.*,1999].

A way to estimate the angular deviation $\Delta\theta$ classically is illustrated in Fig. 3.3 in a simple picture of atoms bouncing from a hard-wall potential. In this simplified picture, the atoms with incident velocity $\vec{v}$ bounce off the magnetic field contours close to the turning point. The angular deviation $\Delta\theta$ can be estimated from the corrugations in these contours near the turning point (Fig. 3.3) from the equations following below.

The height of the turning point z_{turn} is given approximately by

$$z_{turn} \approx k^{-1} \ln(B_{turn} / B_o), \tag{3.1.1}$$

where the magnetic field B_{turn} at a turning point is

$$B_{turn} = E / g_F m_F \mu_B , \tag{3.1.2}$$

$B_o \propto I$ is the field at the mirror surface (Eqn. 2.3.3, Chapter 2), and E is the atomic energy of the center of mass motion. The magnetic field contours close to the turning point are given implicitly by

$$B(x,z)=B_{turn}, \tag{3.1.3}$$

or explicitly, by a curve $Z(x)$, illustrated in Fig.3.3.

The rms angular deviation $\Delta\theta_{rms}$ can be estimated from

$$(\Delta\theta_{rms})^2 = (1/W)\int_{-W/2}^{W/2}(\Delta\theta(x))^2 dx = (1/W)\int_{-W/2}^{W/2}(dZ(x)/dx)^2 dx, \qquad (3.1.4)$$

where $\Delta\theta(x) = Z(x)/dx$ (Fig.3.3), and $dZ(x)/dx = -(\partial B(x,z)/\partial x)/(\partial B(x,z)/\partial z)$, which follows from Eqn. (3.1.3) by taking a partial derivative of B with respect to x.

3.2 Mirrors with even and odd numbers of wires

In designing mirrors it is important to take into account whether the mirror has an even or an odd number of wires. In this section, we describe the following properties of finite mirrors: (*i*) mirrors with an odd number of wires in the serpentine mirror array are more specular than mirrors with an even number of wires, and (*ii*) an array of guides is formed above finite mirrors, with the guide location being different for odd and even mirrors.

(*i*) Figures 3.4(a) and 3.4(b) compare the magnetic field configurations above the centers of the two micro-electromagnet mirrors used in the actual experiment described in Chapter 6, with an even (N = 102) in Fig. 3.4 (a) and odd (N = 101) number of wires in Fig. 3.4 (b). The wires in the array are taken for simplicity to have rectangular cross-sections.

As shown in Figs. 3.4 (a) and 3.4 (b), there is a clear difference between the magnetic field configurations for mirrors with an odd and even number of wires, the mirror with odd N having smoother contours than the mirror with even N. This difference can be understood by noting that the magnetic field of finite-size mirrors $\vec{B}_{fin}$ can be expressed as

$$\vec{B}_{fin} = \vec{B}_{inf} - \vec{B}_{miss}, \tag{3.2.1}$$

where $\vec{B}_{inf}$ is the magnetic field of an infinite mirror, and $\vec{B}_{miss}$ is the magnetic field due to wires that are missing in the finite mirror compared to the infinite mirror.

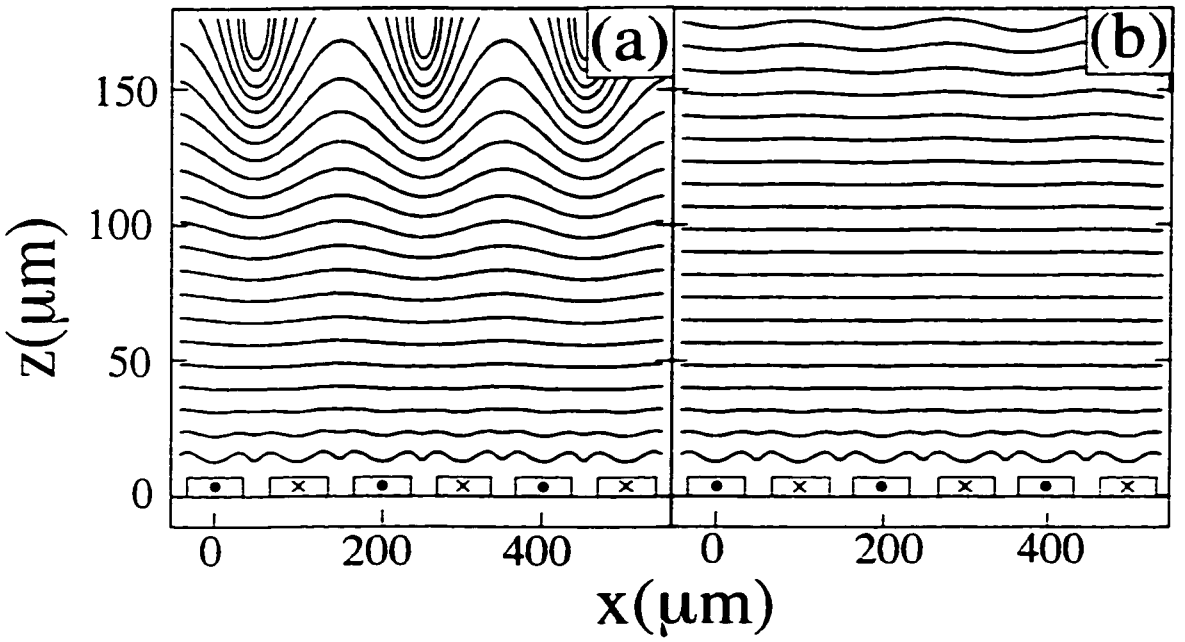

FIG. 3.4 Computed magnetic field magnitude contours above two micro-electromagnet mirrors with (a) even $N = 102$ and (b) odd $N = 101$ wires. The serpentine mirror area is 1 cm^2, the period $a = 200$ μm, wire width $w = 70$ μm, and wire height $h = 7$ μm. The wire width w and height h are defined in Fig. 2.3 (b), Chapter 2. The mirror center is at $x = 0$ and z is the height above the substrate. Subsequent contours are in the ratio $B_{n+1}/B_n = 0.8$, where n = 1 to 20, and $B_1/I = 7.2$ mT/A.

Surfaces of constant B-field magnitude for an ideal infinite mirror, at distances $z >> a/2\pi$, are planes at constant z: $\left|\vec{B}_{inf}\right| \approx \varepsilon_o I e^{-kz}\left|\cos(kx)\vec{e}_x + \sin(kx)\vec{e}_z\right| = \varepsilon_o I e^{-kz}$ (see Eqn. (2.3.1), Chapter 2). In contrast, from Eqn. (3.2.1) we have that the surfaces of constant B-field magnitude for a finite mirror are given by

$$\left|\vec{B}_{fin}\right| = \sqrt{B_{inf}^2 + B_{miss}^2 - 2\vec{B}_{inf} \cdot \vec{B}_{miss}} \ , \tag{3.2.2}$$

and include cross-terms between $\vec{B}_{inf}$ and $\vec{B}_{miss}$. The current distributions producing $\vec{B}_{miss}$ consist of two infinite wire arrays spanning in the intervals $(-\infty, -W/2 - a/2)$ and $(W/2 + a/2, \infty)$ along the x-direction, on both sides of the mirror, where $x = \pm W/2$ is the position of the end wires along the x-direction in the finite mirror array (Fig.3.1). In section 3.4 (Eqns. (3.4.1.) and (3.4.2)) we show that these two current distributions can be replaced by two wires located at $x = \pm (W/2 + a/2)$ to produce a magnetic field approximately equal to $\vec{B}_{miss}$ above the mirror center. In the case of a finite mirror with an odd (even) number of wires, these two wires carry currents in equal (opposite) directions. This results in a $\vec{B}_{miss}$ that is small (large) near the center of the odd (even) mirror, making the odd mirror flatter than the even. For a more detailed analytical treatment of Eqn. (3.2.2) see [Zabow G. *et al.*, 1999].

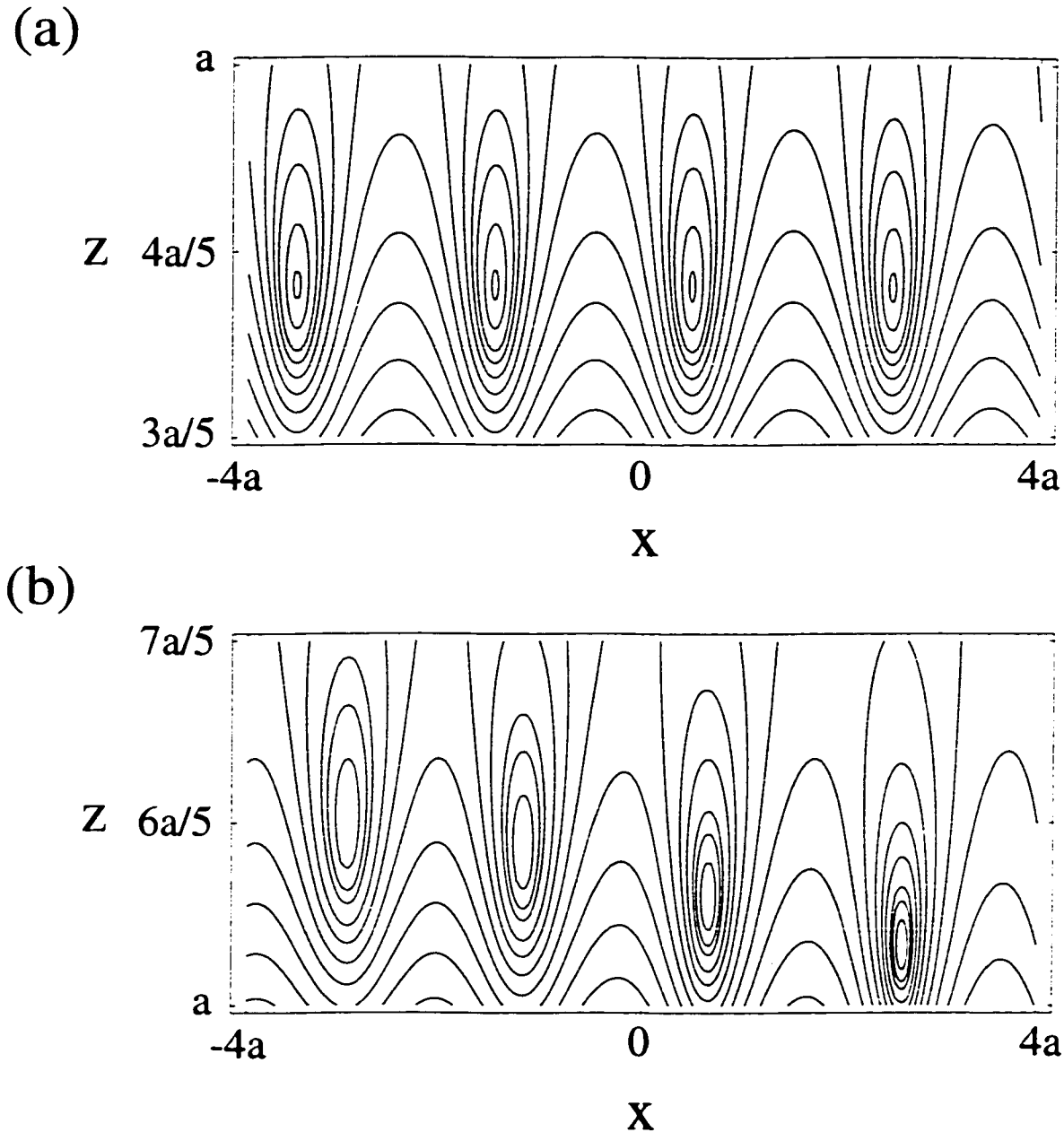

FIG.3.5 Contours of constant magnetic field B above the center of a mirror with (a) $N = 84$ wires and (b) $N = 83$ wires, with period a. An array of shallow quadrupole guides with $B = 0$ at their centers is formed at heights $z_o = \ln(N)/k$, $k = 2\pi/a$, above the mirror center.

(*ii*) Another nontrivial property of finite-size mirrors is the formation of one-dimensional guides above the mirror centers, at heights near $z_o = \ln(N)/k$. The guides are formed for both mirrors with an even N and with an odd N number of wires. In Fig. 3.5 we show the contours of constant magnetic field magnitude B, for mirrors with even $N = 84$ in Fig. 3.5 (a), and odd $N = 83$ in Fig.3.5 (b). The mirror periods and areas are the same as in Fig.3.2. The formation of guides is clear from Fig.3.5. The regions of the magnetic field minima in the guides are parallel to the wires along the y-direction, and are separated in the x-direction by a mirror period a. The magnetic field inside the guides is quadrupole. The guide centers are lines of zero B-field along the y-direction (Fig.3.5). The depth of the guides B_{max} is ~ 2 orders of magnitude smaller than the field B_o at the mirror surface. For fabricated mirrors (Chapter 4), the trap depth is $B_{max} < 1G$ for $a = 50$ μm, and $I = 1$ A. This small field means that the guides will not significantly affect the trajectories of atoms dropped from a few cm that reach velocities $v \sim 1$ m/s.

The guides are formed at higher heights for mirrors with N odd, as expected from the comparison of mirrors with odd and even N in Fig.3.4. This difference is further illustrated in Fig. 3.5 where we compare the formation of guides above two mirrors with even (Fig.3.5 (a)) and odd numbers of wires (Fig.3.5 (b). The position of guide centers in the xz-plane can be calculated analytically from Eqn. (3.2.2) for guides formed above the mirror center by setting $\left|\vec{B}_{fin}\right| = 0$. The guide centers lie on a surface $Z(x)$ defined by $Z(x) \approx z_o$ for N even, and $Z(x) \approx z_o + 1/k \ln(W\sqrt{x^2 + Z^2(x)}/2)$ for N odd, where W is the mirror width in the x-direction [Zabow G. *et al.*, 1999].

The guides formed above the typical mirrors (Chapter 4), with a large number of wires $N \sim 100$, are shallow. However, for small N, $N < 10$, the guide depths are comparable to the surface field B_o, and in that case micro-electromagnet guides are formed. We have already introduced such guides in Chapter 2 with an example of $N = 4$ equally spaced wires alternatively carrying currents in opposite directions (Fig. 2.5). In Fig.3.6 we show another example of micro-electromagnet guides formed from $N = 3$

equally spaced wires alternatively carrying currents in opposite directions. For wire spacing $a/2 = 10\ \mu m$ and current $I = 1$ A, the guide depth $B_{max} = 60$ G.

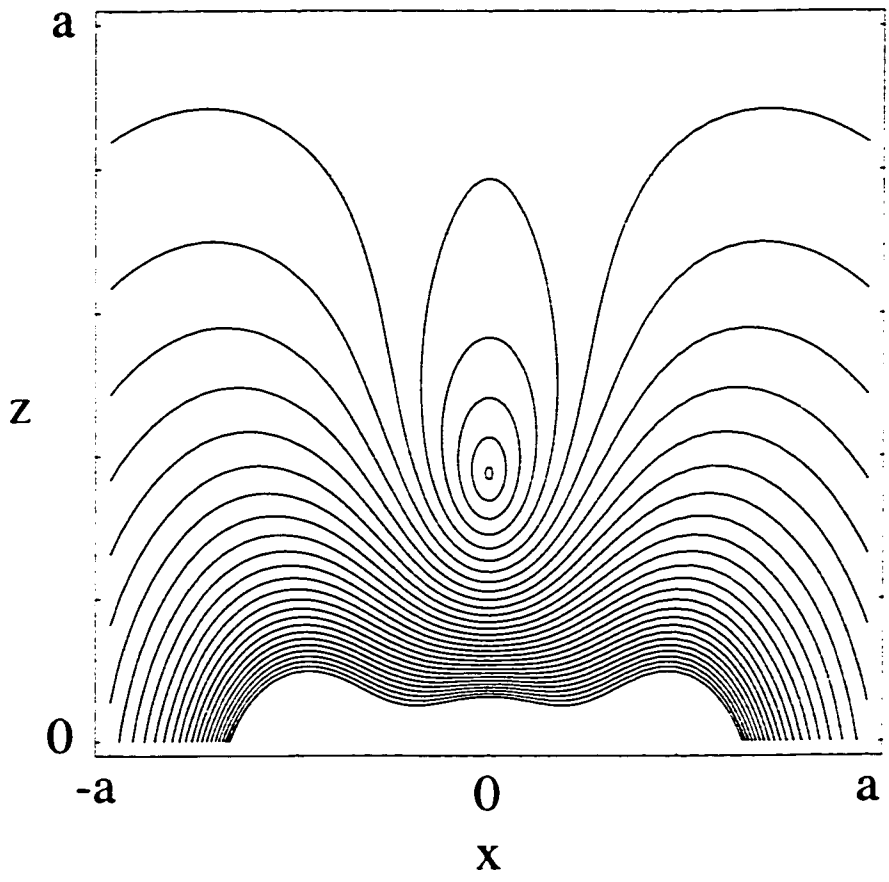

FIG.3.6 Contours of constant magnetic field B above $N = 3$ wires located at $x = 0$ and $x = \pm a/2$ with alternating current directions and magnitude I. A single guide is formed above $x = 0$ along y-direction with $B = 0$ at the center. Subsequent contours are spaced by an equal increment ΔB.

3.3 Magnetic field configuration close to the mirror edge

In this section we describe the magnetic field configuration close to the edges of a finite mirror along the x- and y-directions, which are defined in Fig.3.1. The width W of the mirror in the x-direction strongly influences the mirror corrugations. On the other hand, the effect of the finite wire length $L \sim W$ on the mirror corrugations is negligible compared to the effects from the finite width W.

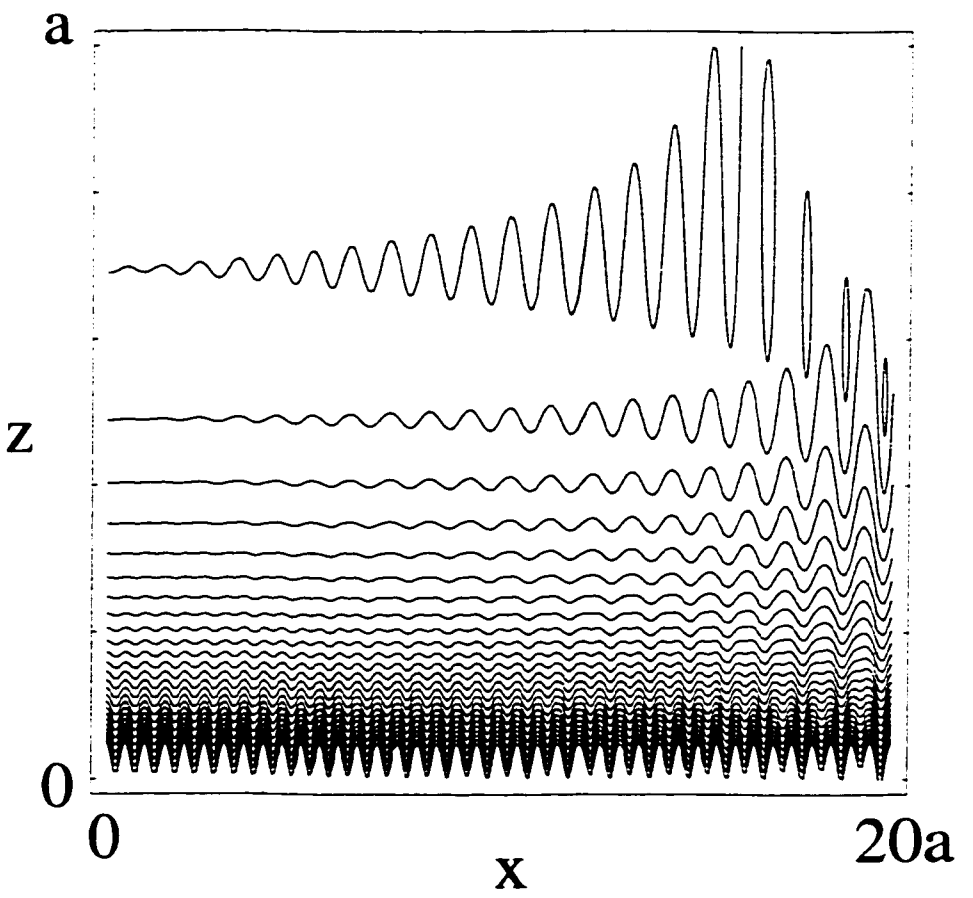

FIG.3.7 Computed contours of constant B above a mirror from the mirror center at $x = 0$ to the mirror edge at $x \approx 20\,a$, with the mirror period a; number of wires $N = 83$; $y = 0$. Subsequent contours are spaced by an equal increment ΔB. The contours are relatively flat lines above the mirror center, and become more strongly corrugated near the mirror edge.

In the previous sections, the magnetic field contours were presented above the center of the mirror at x=0, y=0. Near the mirror edges along the y-direction at $x = \pm W/2$, the contours become more strongly corrugated. This is clear from the magnetic field contours in Fig.3.7 for a mirror with $N = 83$ wires, and $W = 41\ a$.

The effect of finite length L of mirror wires on mirror corrugations is negligible compared to the effect of finite width W, described above. For infinitely long wires, the magnetic field magnitude does not depend on the distance y from the mirror center at $y = 0$. In contrast, the magnetic field magnitude for wires of finite length L depends on y. The finite wire length results in a nonzero curvature $\partial^2 B / \partial^2 y$ of the magnetic field contours along y-direction, but the corrugations caused by it are negligible compared to the corrugations illustrated in Fig.3.7.

3.4 Magnetic field configuration above a compensated mirror

Several authors have pointed out that the specularity of finite mirrors can be improved by adding compensating wires [Sidorov A.I. *et al.*, 1996; Lau D.C. *et al.*, 1999; Zabow G. *et al.*, 1999]. The purpose of these added wires is to mimic the field of an ideal infinitely large mirror by using a mirror with a finite number of wires.

Figure 3.8 shows a schematic diagram of a compensated mirror [Zabow G. *et al.*, 1999] with the current directions and magnitudes indicated. The current in the mirror is I, while the current in the compensating segments is $I/2$. The two wire segments placed at $x = \pm(W/2 + a/2)$ along the y-direction compensate for the finite number of wires. The other two wire segments placed at $y = \pm(L/2 + a/2)$, compensate for the effect of the short wire segments parallel the x-direction, connecting the individual wires.

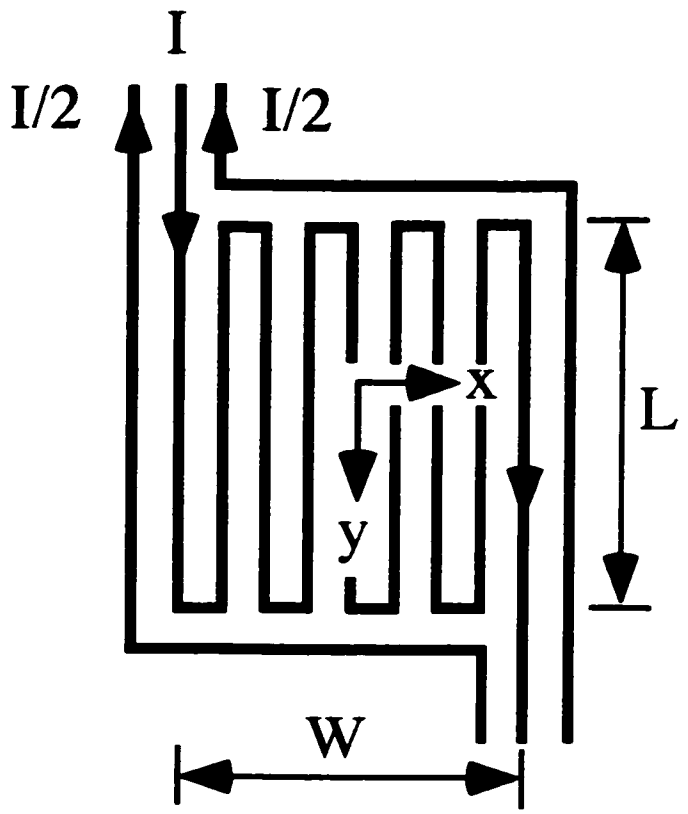

FIG. 3.8 Mirror pattern with indicated current directions and magnitudes for a mirror with an odd number of wires, compensated for the detrimental effect of the finite number and finite lenght of wires in the serpentine array.

The magnetic field produced by the two additional wires placed at $x = \pm(W/2+a/2)$ along the y-direction with currents $I/2$ is approximately equal to the magnetic field $\vec{B}_{miss}$ of the missing wires (See also Eqn.3.2.2). This is shown for the magnetic field above the

mirror center ($x = 0$, z=0) from the following equations. The magnetic field magnitude above the mirror center that is produced by the two wires at $x = \pm(W/2+a/2)$ is given by

$$B \approx 2\mu_o(I/2)/(2\pi(W/2+a/2)), \tag{3.4.1}$$

while the field from the missing wires is

$$B = 2(\mu_o I/2\pi a)(\sum_{i=0}^{\infty}[1/(i+(W+a)/2a) - 1/(i+(W+a)/a)] \approx 2(\mu_o I/2\pi a)\ln(1+a/(W+a)). \tag{3.4.2}$$

For $a << W+a$, $\ln(1+a/(W+a)) \approx a/(W+a)$, and the expressions in Eqns. (3.4.2) and (3.4.1) are equal.

A compensated mirror illustrated in Fig. 3.8 is significantly more specular than the uncompensated mirror illustrated in Fig.3.1. In Fig. 3.9 we show the magnetic field contours above a compensated mirror with $N = 83$ wires. The contours above a compensated mirror in Fig.3.9 are smoother than the contours above an uncompensated mirror in Fig.3.7 with all other parameters being equal. In Chapter 6 we will describe the experimental results showing the improvement of specularity for mirrors with the compensating wires.

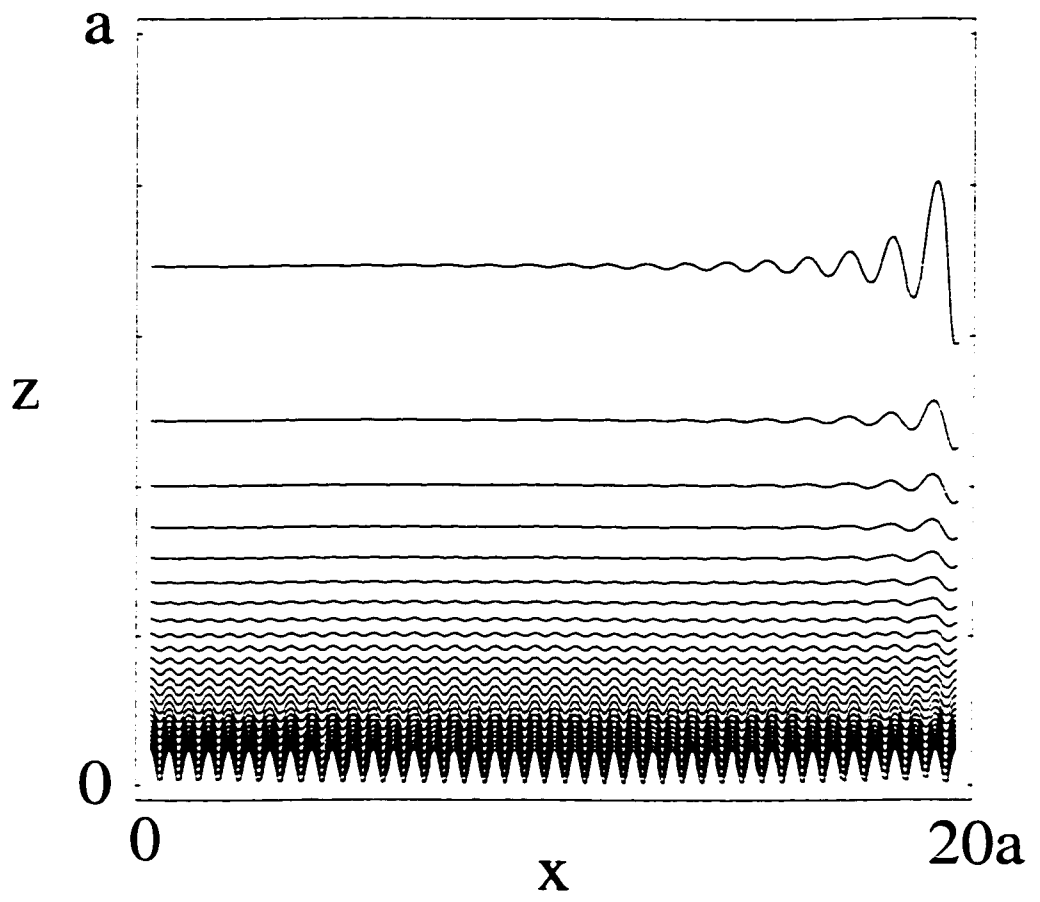

FIG.3.9 Computed contours of constant B above a compensated mirror (see Fig. 3.8) from the mirror center at $x = 0$ to the mirror edge $x = 20a$, a is the mirror period; $N = 83$. Subsequent contours are spaced by an equal increment ΔB. The magnetic field contours are relatively flat lines above $x = 0$, and become corrugated closer to the mirror edge.

3.5 Magnetic field configuration close to the wires

In this section we show that: (*i*) specularity of micro-electromagnet mirrors is strongly affected by the cross-sectional shape and separation of the wires in the serpentine mirror arrays, and (*ii*) mirror specularity above fabricated oval-shaped wires can be better than the mirror specularity above rectangular wires with the same wire separation.

Close to the surface of the mirror, the magnetic field contours critically depend on the surface boundary conditions. Recent simulations showed that wire cross-sectional profiles and separation can be optimized to make high quality mirrors [Zabow G. *et al*,1999]. This is demonstrated in Fig. 3.10 [Zabow G. *et al*,1999], which shows the magnetic field contours above three mirrors with different wire shapes: (a) rectangular wires, (b) wires with optimized cross-sectional profiles, and (c) microfabricated wires with measured cross-sectional profiles[2].

Figures 3.10 (a) and 3.10(b) show the magnetic field contours above two mirrors with period a = 50 μm that differ only in the shape of the wires. The magnetic field contours above the mirror with an optimized wire profile in Fig. 3.10 (b) are two orders of magnitude flatter than the contours above the mirror with rectangular wires in Fig.3.10 (a).

[2] The wire profiles were measured using an atomic force microscope. Details of fabrication and formation of oval-shaped wires as in (c) are described in Chapter 4. The numerical calculations shown in Figs. 3.9 (a)-(c) were performed by G. Zabow.

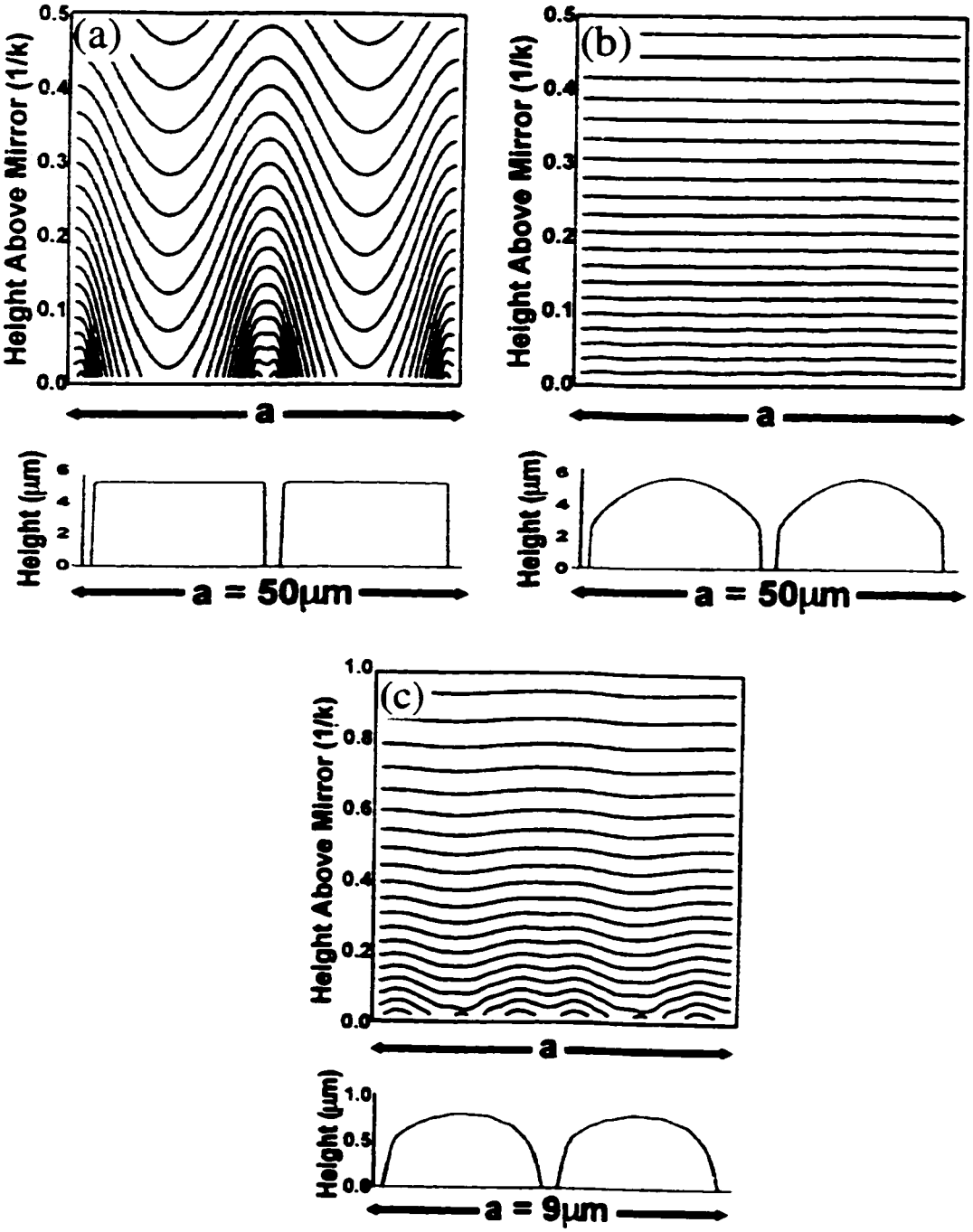

FIG.3.10 Computed contours of constant B, equally spaced in the z-direction, above a mirror with (a) rectangular wires, (b) wires with an engineered cross-sectional profile to achieve flattest contours, and (c) fabricated wire with cross-sectional profiles measured with an atomic force microscope. A uniform current density and electrical resistivity is a good approximation for small wires; $z = 0$ is defined at the top of the wires. Magnetic field contours from G. Zabow; wire profiles in (c) from M. Drndic.

Finally, the magnetic field contours above fabricated wires are up to one order of magnitude flatter than the contours above rectangular wires with the same wire separation. This is illustrated in Fig.3.10 (c), for the magnetic field contours above fabricated wires with wire separation $a/2 = 9$ μm. These oval-shaped wires were formed during electroplating, as will be described in Chapter 4, and their cross-sectional profiles were recorded using an atomic-force microscope. We adjusted the fabrication parameters to make the real wire shape (Fig.3.10 (c)) look like the optimal wire shape shown in Fig.3.10 (b).

Chapter 4

FABRICATION AND PROPERTIES OF MICRO-ELECTROMAGNETS

In this Chapter we describe the fabrication, electrical and thermal properties of micro-electromagnets for atom manipulation. Micro-electromagnets consist of planar micron-scale Au wires on sapphire substrates fabricated using photo-lithography and electroplating. Photo-lithography allows for the fabrication of complex patterns across large surface areas with excellent control to create novel field configurations for atom manipulation. Electroplating permits high currents (current density of $\sim 10^8 A/cm^2$) and magnetic fields to $B \sim 0.3$ T with gradients $|\nabla B| \sim 10^5$ T/m. Fabricated mirrors (serpentine pattern), traps (circular patterns) and other configurations (curved mirrors and guides) for atoms are presented. We have experimentally investigated Au, Cu and Ag wires on sapphire substrates and Nb on silicon substrates. The best results are obtained with Au, for which we achieved the highest current densities.

Magnetic field magnitudes B, gradients $|\nabla B| = \sqrt{(\partial B/\partial x)^2 + (\partial B/\partial y)^2 + (\partial B/\partial z)^2}$ and curvatures $\nabla^2 B = \partial^2 B/\partial^2 x + \partial^2 B/\partial^2 y + \partial^2 B/\partial^2 z$ generated from current carrying wires typically scale as $B \propto I/d$, $|\nabla B| \propto I/d^2$ and $\nabla^2 B \propto I/d^3$, where I is the wire current and d is the characteristic size of the system. If we consider a simplified case of a normal wire of width w on a planar substrate carrying a current I, the condition to remove the Ohmic heating via heat conduction through the substrate gives $I/w \leq (\kappa \Delta T_{max}/\rho)^{1/2}$, where κ is the thermal conductivity of the wire, ρ is the electrical resistivity, and ΔT_{max} is the maximum allowable temperature difference to the substrate. For Au at room temperature with ΔT_{max} = 100 K and standard values for κ and ρ [*American Institute of Physics Handbook* (ed. Gray D.E.), 1982], we have $I/w \leq 1$ A/μm. This corresponds to a current

density of 10^8A/cm^2 through wires 1 μm thick and 1 μm wide. Cooling can be used to achieve even higher values of I/w by reducing ρ and increasing κ.

The maximum current in superconductors is limited either by the critical field H_c (Type I) or by flux pinning (Type II). Among existing materials, Nb, NbTi, and Nb_3Sn could be used to obtain current densities up to 10^7A/cm^2 [*Materials at Low Temperatures* (eds. Reed R.P. and Clark A.F.), 1983], lower than the values we report for Au micro-electromagnets. However, for devices with surface areas larger than ≈ 1 cm^2, superconductors can be advantageous for lack of heating.

4.1 Fabrication: Optical Lithography and Electroplating

The fabrication is done in following steps, illustrated in Fig.4.1: lithography, electroplating and annealing. First, photo-lithography is used to define the wire geometry on a 0.5 mm thick sapphire substrate 2.5 cm in diameter. Sapphire washers and windows of different shapes, thickness and optical flatness are available from *General Ruby and Sapphire, Inc.*[1], as well as suppliers[2] of optical elements such as *Melles Griot* and *Meller Optics*. Photo-lithography is used to control precisely the mirror geometry across large surface are as (~ 1 cm^2).

---

[1] *General Ruby and Sapphire, Inc.* P.O. Box 610, Newport Richley, FL 34656, 1-800-535-5374.

[2] *Meller Griot* 1-800-835-2626; *Meller Optics* , Providence RI 02940, 1-800-821-0180.

[3] Microposit Primer and Microposit 1813 resist, Shipley, Malborough, MA 01752.

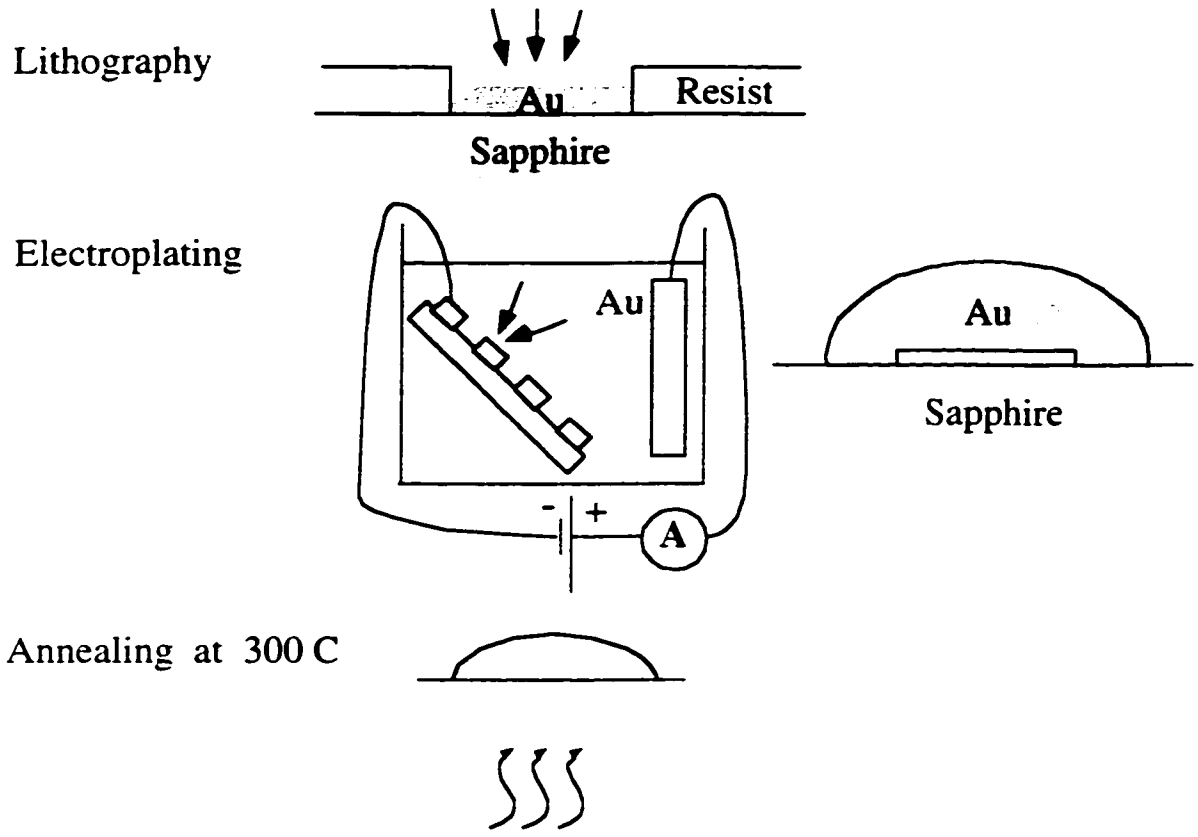

FIG.4.1 Schematic diagram of fabrication steps: lithography, electroplating, annealing.

Details of fabrication are as follows: First, the substrate is cleaned in trichloroethylene (TCE), and then ultrasounded in acetone and methanol for 10 minutes each. After baking the substrate at 180 °C for ~ 10 minutes to remove any leftover solvents on the sapphire surface, an organic primer and resist[3] are spun on consecutively for 30 s each at 5000 rpm; the primer is used to ensure better adhesion of the resist on the sapphire surface. The spun-on resist is then baked on a hot plate at 100 °C for 3 minutes, and exposed to UV light for 5s through a 3 inch in diameter chrome and glass mask

(manufactured by *Advance reproductions*[4]) using the Karl Suss Stepper in the cleanroom. The resist is developed for 60 s, cleaned in distilled water and dried off. After checking with an optical microscope that the wire pattern has been successfully developed in the resist, we proceed with metal evaporation. A gold layer up to 4000Å thick is evaporated on top of a 50 Å Cr adhesion layer, and the resist is then lifted-off in acetone[5].

To achieve the high current carrying capabilities of devices, the wires are made thicker by electroplating (see Fig. 4.1) to further reduce the resistance. Electroplating is widely used for its advantages over dry methods (sputtering and metal evaporation) for fabrication of thick films (tens of microns thick), metallization of holes, and formation of soldering bumps. It is also a less expensive process.

Because most devices were made out of Au, we outline the electroplating procedure for Au. The fabrication processes for Cu, Ag, and Nb micro-electromagnets are similar. We have also made Cu and Ag wires. Gold surfaces have the practical advantage of being chemically inert, which is necessary for good heat transfer and electrical conductivity at interfaces.

Electroplating of gold proceeds as follows: the wires, connected as cathode, are electroplated with Au using In contacts and Cu leads. Mirrors have four contacts for four-terminal measurements. The Au electroplating bath is a pH ≈ 7, sulfite bath (TG 25E) commercially prepared and filtered from *Technic Inc*[6]. The bath contains ~3% $Na_3Au(SO_3)_2$, ~8% Na_2SO_3, and is heated to 60°C. The percentage of chemicals in the

---

[4] Advance Reproductions Corp., Willows Industrial Park, 100 Flagship Drive, North Andover, MA 01845, Tel. (978) 685-2911.

[5] The lift-off is sometimes slow and gentle ultrasounding of the sample helps, but can form 'dog ears' on the wire edges. These tall edges can grow disproportionately large during electroplating and can cause the shape of the wire to look bimodal.

[6] Technic Gold 25E (ready to use) with 1/4 ounce of Au per quart of solution; Technic Inc., Providence, RI 02940, Tel. (401) 781-6100; Other gold solutions are available such as the neutral immersion 24Kt Au bath (Oromerse Br) for electroless plating of Ag, Cu, Ni, Fe, Pb, solder, brass, etc.

solution is defined by volume. To obtain smooth surfaces, plating is done at low currents (< 1mA) with magnetic stirring of the solution. The anode is a thin Pt foil (high purity, available from *AlfaAesar*[7]) with area 1 x 1 cm^2 separated ~ 3 cm from the device.

There is a significant reason for using low current densities during electroplating. In order to have a uniform metal deposition throughout the wire pattern, the voltage drop across any two points on the wire pattern (cathode) has to be much smaller than the applied voltage ΔV between the electrodes. In the case of a wire of length L, cross-sectional area S, and electrical resistivity ρ, this condition can be expressed as $\rho L I / S << \Delta V$. If this condition is not satisfied, a resulting deposition rate will decrease across the wire length.

From equation

$$M = KQ, \tag{4.1.1}$$

where M is the deposited mass, K is the material constant ($K = 2 \times 10^{-3}$ g/C for gold[8]), and Q is the required charge, we estimate Q to grow the wires to desired sizes. The total charge of the deposited material is determined from the monitored current and the plating time t. The required plating time is easily estimated and can vary from minutes to hours depending on the wire length. The overall current density i ~ 1 mA/cm^2 is applied[9] (i is defined as the applied current divided by the sum of all the cathode area on the substrate).

---

[7] AlfaAesar, Ward Hill, MA 01835, http://www.alfa.com, Tel. 1-800-343-0660.

[8] $K = (1/F)(A/Z)$, where A is the atomic number [in g/mol], F is the Faraday constant [96.5 kC/mol], and Z is the atomic valence ($Z = 1$ for Au, $Z = 2$ for Cu).

FABRICATED MIRRORS

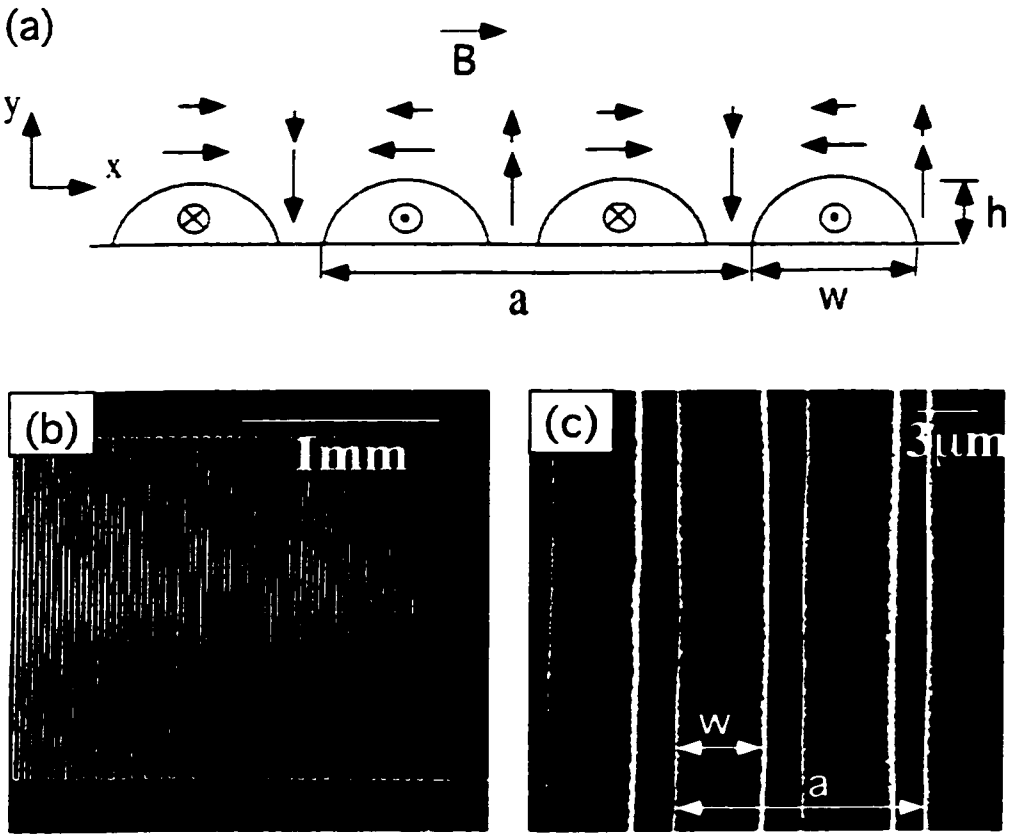

FIG. 4.2 (a) Schematic diagram of a serpentine micro-electromagnet mirror and the magnetic field above it. a is the period, w the wire width, and h the wire height; (b) and (c) scanning electron microscope (SEM) images of Au mirrors on sapphire substrates: (b) $a = 48$ μm, $w = 12$ μm, $h = 0.3$ μm; (c) $a = 12$ μm, $w = 4.3$ μm, $h = 1.7$ μm.

Figure 4.2 shows the schematic diagram of a serpentine mirror pattern (Fig.4.2 (a)), and the scanning electron microscope (SEM) images of fabricated micro-electromagnet mirrors (Figs 4. 2(b) and 4. 2(c)). We have made mirrors with periods a (see Fig. 4.2 (a)) ranging from $a = 12$ μm to $a = 200$ μm, with up to $N = 1667$ parallel wires, covering areas up to 1 cm^2.

A fabricated mirror in Fig.4.2 (b) has an area 2x2 mm^2 and period $a = 48$ μm. After evaporation the mirror resistance[10] was $R \sim 2$ kΩ, and the wires had a wire width $w = 12$ μm and the wire height $h = 0.1$ μm. After electroplating for ~ 4 hr, $R \sim 60$ Ω at 300K ($R \sim 6$ Ω at $T = 4.2$ K) and the wire width and height increase to $w = 20$ μm, and $h = 3$ μm. The mirror shown in Fig.4.2 (c) has an area 2x2 mm^2, period $a = 12$ μm, and $R \sim 2$kΩ at 300 K. The wire width is $w = 4.3$ μm, and the wire height is $h = 1.7$ μm. For ~ 1x1 cm^2 mirrors with large periods a ~ 100 μm, plating can last as long as 24 hr to grow the wires tens of microns wide and high at low current densities.

Using the same procedure described above, we have fabricated other types of micro-electromagnets for atom manipulation. Figures 4.3 (a), 4.3 (b) and 4.3 (c) show scanning electron microscope images of micro-electromagnet traps as suggested theoretically by [Weinstein J.D. and Libbrecht K.G., 1995]. The radii of the circular traps vary from 30 μm to 50 μm. We have also fabricated arrays of traps as shown in Fig. 4.3 (d).

[10] The calculated room temperature resistances $R = \rho L/(wh)$, where L is the wire length, and ρ is the resistivity of the metal agree well with the measured values. At low temperatures, the calculated resistances are up to 4 orders of magnitude lower than the measured ones, due to the low purity (high resistivity) of fabricated wires.

FABRICATED TRAPS

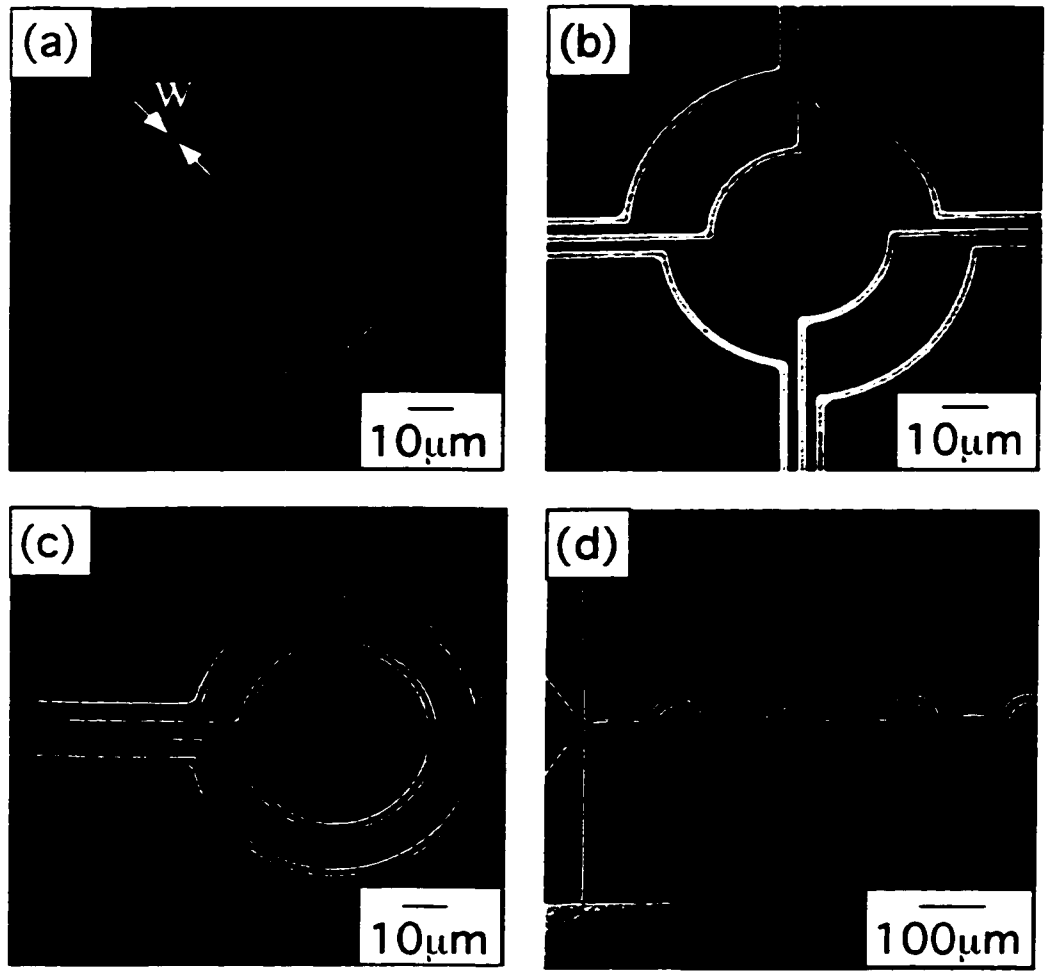

FIG. 4.3 SEM images of micro-electromagnets with geometries suggested for trapping atoms. Traps are Au on sapphire substrates with w = 3μm and h = 1μm. (a) Two half loops. (b) three concentric half loops. (c) two full loops. (d) array of traps.

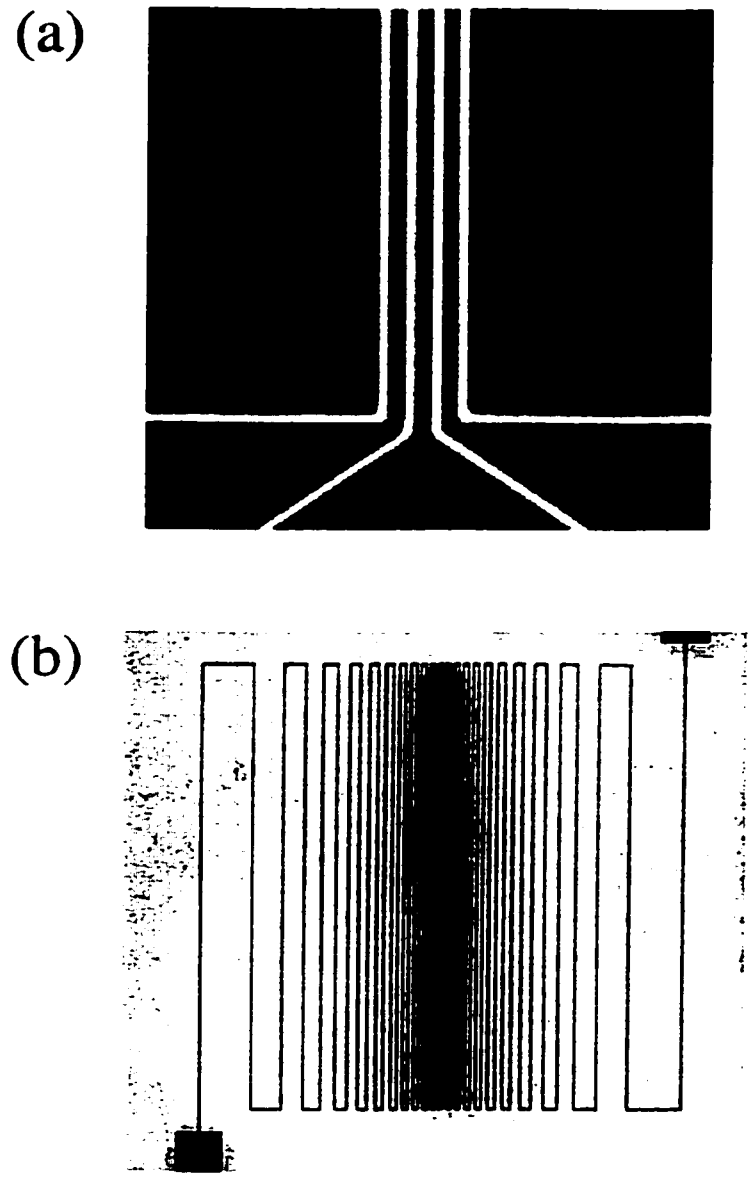

FIG. 4.4 Micrographs of micro-electromagnet (a) guides (see also Fig.2.5) with wire width $w = 3$ μm, and (b) curved mirrors with wire width $w = 40$ μm covering an area ~2 cm^2 (see also Fig. 2.6).

Traps in Fig.4.3 are Au on sapphire substrate with wire width $w = 3\mu m$ and height $h = 1\mu m$. Traps in Fig.4.3 (a) and Fig. 4.3 (b) are Ioffe-type traps with a non-zero value of magnetic field B at the trap center, and with B increasing quadratically away from the center [Weinstein J.D., Libbrecht K.G., 1995]. Quadrupole traps shown in Fig.4.3 (c) and 4.3 (d) have been discussed in Chapter 2. The maximum trap depth is achieved for the ratio of currents $I_1/I_2 = 0.533$, and the ratio of radii $r_2/r_1 = 2.66$, where I_1 and r_1 are the current and radius of the inner loop, and I_2 and r_2 are the current and radius of the outer wire loop.

In Fig.4.4 we show a fabricated micro-electromagnet guide (Fig.4.4 (a)) with wire width $w = 3\mu m$, and the same wire separation, and a focusing micro-electromagnet mirror (Fig. 4.4 (b)) with wire width $w = 40\ \mu m$, covering an area ~2 cm^2. The magnetic field configurations produced by these wire geometries were discussed in Chapter 2 (Fig. 2.5 and Fig. 2.6).

The fabrication of superconducting Nb micro-electromagnets was done by sputtering a Nb film on silicon wafers, with the sputtered layer thickness up to ~1 μm. For higher sputtered thickness, the stress in Nb layers degraded the superconducting properties. The Nb micro-electromagnets were not electroplated. Figure 4.5 shows the SEM image of a Nb mirror on silicon with $a = 12\ \mu m$ and area 2 x 2 mm^2 ($N = 333$).

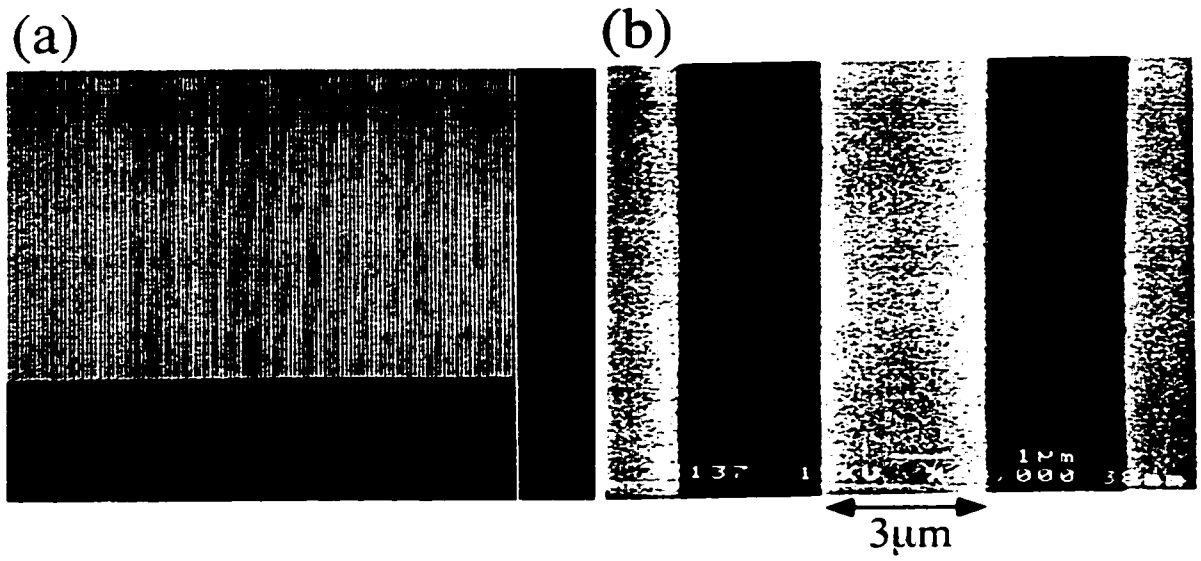

FIG. 4.5 SEM images of the sputtered Nb micro-electromagnet mirror on a silicon substrate with area 2 x 2 mm^2, $w = 3$ μm and $h = 0.3$ μm: (a) large view, (b) close-up view.

4.2 Shape of electroplated micron-size wires

The ability to precisely control the particle motion with micro-electromagnets requires a precise spatial configuration of the magnetic field produced. Because the wire shape determines the surface boundary conditions for calculating the magnetic field, it will also affect the spatial configuration of the electromagnetic field above the devices. In many schemes for atom manipulation with microstructures, the atoms will approach the surface of the device, making it even more important to control the landscape on a sub-micron scale.

Control of wire profiles is useful to make high quality mirrors as illustrated by recent theory [Zabow G. *et al.*, 1999]. Measurements with a mirror in Fig. 6.1 indicated the importance of wire shape on the reflective mirror properties [Cognet L. *et al.*, 1999]. These results will be discussed in more detail in Chapter 6. A variety of wire shapes might thus be needed to control the field configuration precisely.

The control of micro-wire shapes is important for applications. In microelectronic applications, using resist patterned[11] ("through-mask") electroplating, extremely flat wire profiles are sought. Flat and rectangular conducting micro-wires have the highest cross-sectional area and smallest resistance for a given maximum height and width. Flat wire profiles are also needed to fabricate multilayered structures.

Numerical investigations of shape formation [Dukovic J. O., 1993; Chem J. W. E. *et al.*, 1996a, 1996b, 1992; Kondo K. *et al.*, 1998, 1996, 1994; Hazlebeck D.A. *et al.*, 1991, 1989; Shenoy R.V. *et al.*, 1996] have been made for resist-patterned electroplating. Several experimental studies of electroplating have addressed shape evolution on a micron-scale. Micron-scale groove formation on gramophone plates was studied interferometrically [Nanev C. *et al.*, 1975] as a function of chemical additives in the

[11] In the resist-patterned electroplating, rectangular wire profiles are achieved by initially coating the substrate with a seed metal layer (~ 5 nm thick) and then plating vertically through the resist used in lithography. The resist is lifted off and the thin seed layer is etched off to isolate the wires.

plating solution. Recently, formation and roughness of electroplated surfaces was studied using an atomic force microscope (AFM) [Schmidt W. U. *et al.*, 1996] and SEM [Kondo K. *et al.*, 1998]. The match between theory and experiment is qualitative due to complexities of electrochemical transport phenomena.

Using an atomic force microscope (AFM) from Park Scientific Instruments we have investigated wire shape during a multidirectional electroplating. The wires are electroplated without the resist to grow in all directions, resulting in oval-shaped wire cross-sections, as illustrated in Fig.4.6. The wire shape formation was recorded using an AFM at successive time intervals during the wire growth. By appropriately adjusting the plating parameters, the wire dimensions can be continuously varied during fabrication and grown to desired sizes and aspect ratios. The results are qualitatively consistent with electroplating models and previous experimental studies [see for review *Fundamentals of Electrochemical Deposition* (eds. Paunovic M. and M. Schlesinger), 1998]. Atom mirrors realized in this way have a calculated corrugations of magnetic field contours up to ten times lower than mirrors with rectangular wires (see Fig. 3.10).

Figure 4.6 shows a schematic diagram of the resulting wire profiles $f(x, t)$ after a multidirectional plating of a micro-electromagnet mirror for time t. Before the plating was performed, the wire shape was initially rectangular with height h_o, width w_o, and aspect ratio h_o/w_o. The expression $(a/2 - w_o)$ is the initial separation between the wires.

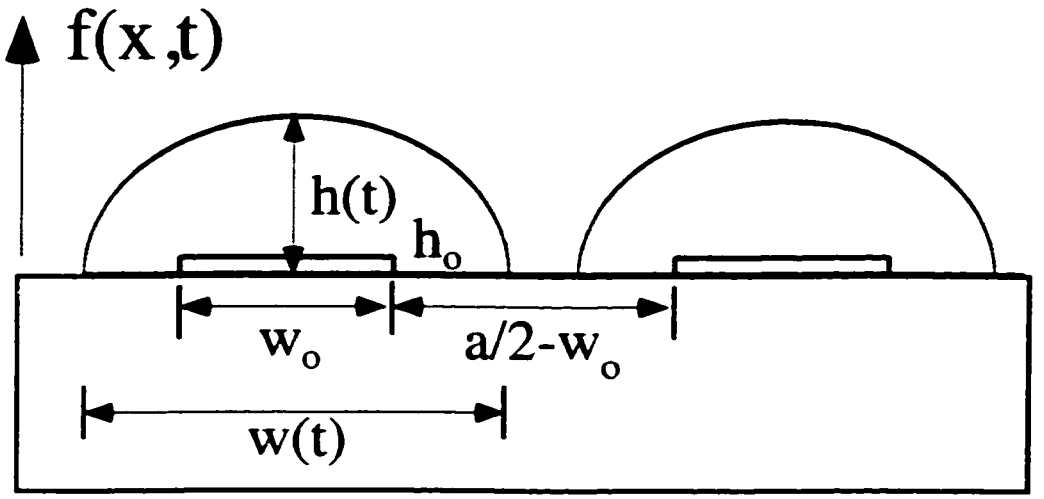

FIG. 4.6 Schematic diagram of the resulting wire profiles $f(x, t)$ after plating time t; w_o and $w(t)$ are the initial and final wire width, h_o and $h(t)$ are initial and final wire height, respectively.

Figure 4.7 shows the AFM scan of a plated mirror with area 2 x 2 mm^2 and $a/2 = 9$ μm, $h_o \approx 0.05$ μm, $w_o \approx 2$ μm: (a) is a three-dimensional AFM picture with $h \approx 0.8$ μm and $w \approx 4.4$ μm, (b) is a series of three AFM line scans to show the evolution of the wire shapes $f(x,t)$ after successive plating times up to $h \approx 1.6$ μm and $w \approx 5.5$ μm.

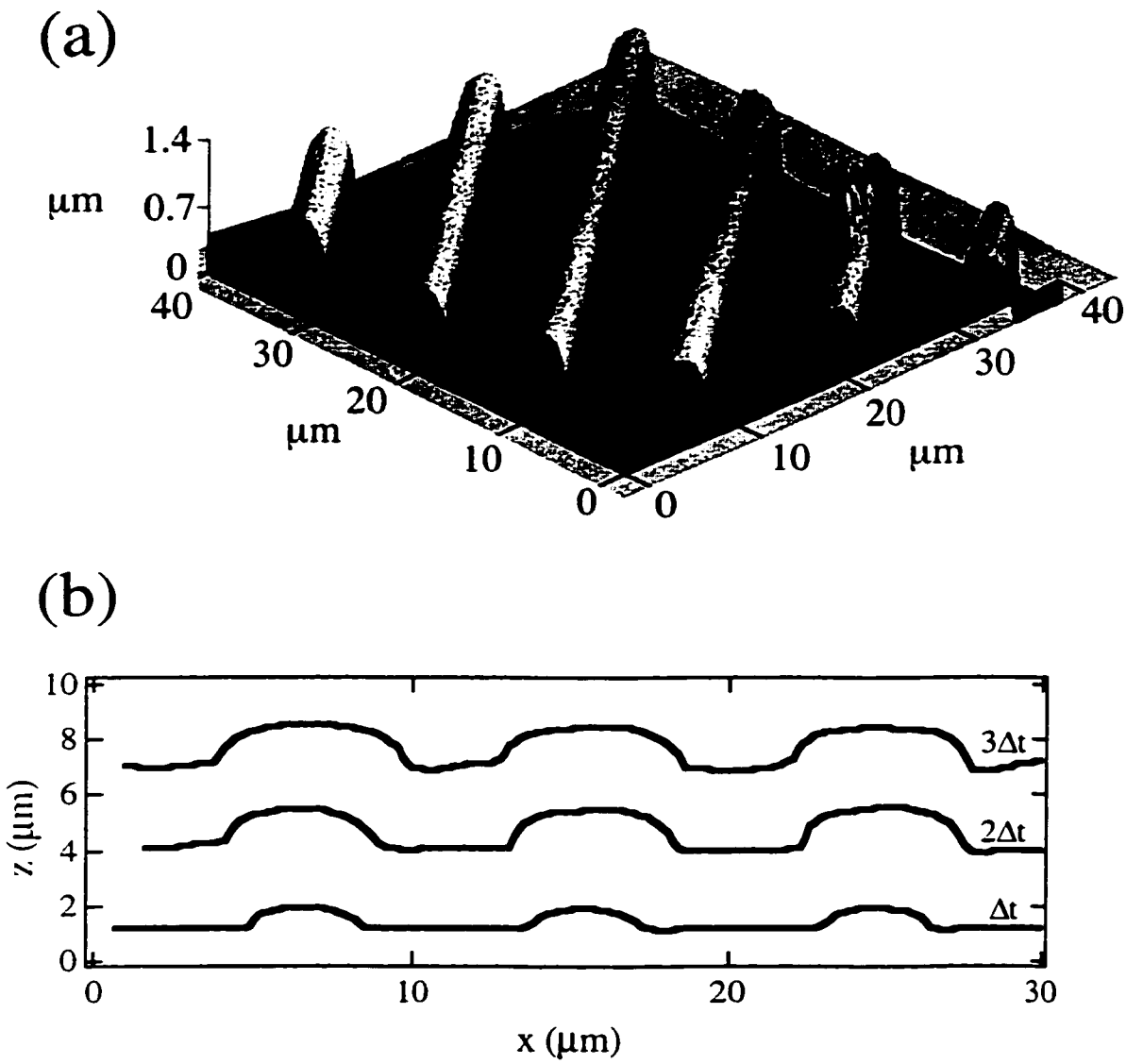

FIG.4.7 (a) Three-dimensional atomic force microscope picture of a micro-electromagnet mirror after electroplating. (b) AFM line scans, along the x-direction perpendicular to the wires, showing the evolution of wire shapes during electroplating after time intervals Δt (bottom line), $2\Delta t$ and $3\Delta t$ (top line) from the beginning of plating; $\Delta t \approx 15$ min.; the line scans are separated in the z-direction for clarity.

As shown in Fig.4.7, the wire surface grows during electroplating in all directions and advances into the space previously occupied by the electrolyte. In most of the cases we have measured, including gold and copper plating, the wires grow roughly two times more rapidly in the x-direction than in the z-direction, possibly due to additives (leveling agents) in the plating solution[12] [review in *Fundamentals of Electrochemical Deposition* (eds. Paunovic M. and M. Schlesinger), 1998]. This is a useful empirical guideline to estimate the plating time from Eqn. 4.1.1. The mass M of the wire after plating for time t, can be approximately calculated using the approximate cross-sectional area of the wires after time t, $A = h\,(w_o+2h)$ (see Fig.4.6), where $w = w_o+2h$ is the wire width, and h is the wire heigth ($h_o<<h$). However, more studies are needed to control and understand the shape formation during electroplating. Generally, the evolution of the wire shape is determined from the current density distribution at the plated surface which depends in a complex way on many factors: the overall current density, additives (brightners or leveling agents) and electrode geometries. The local rate of deposition varies with position and depends on the electrochemical transport phenomena. At ~ 10 μm length scales and below, the dominant transport of the depositing ions is diffusion [Dukovic J.O., 1993].

The current distribution at the electroplated surface is calculated from the Laplace's equation for the potential $\Phi(x,y)$ of the electrolyte, $\nabla^2\Phi = 0$. The boundary conditions are set at $\Phi = V$ at the anode, $\Phi = 0$ at the cathode, and $\nabla\Phi\,\boldsymbol{n} = 0$ at the insulating surfaces, where $\boldsymbol{n}$ is the unit vector of the normal to the surface element. The current density is related to the potential by Ohm's law, $i = -\kappa\nabla\Phi$, where κ is the

---

[12] From the AFM measurements we also looked at the surface roughness superimposed on the overall wire shape. The measured peak to peak roughness on the top of the plated wires was ~ 20 nm, while the measured peak to peak roughness of the sapphire substrates used was ~ 2 nm. The effects of wire roughness on the shape of the magnetic field equipotentials above the wire surface should be suppressed by the electrical current conservation via Kirchoff's current law.

electrical conductivity of the bath. The local deposition rate r (in cm/s) is obtained from the local current density using the Faraday's law: $r = K\,i/\rho$, where K is the material constant[8], and ρ is the density, and the current efficiency of metal dissolution is often assumed to be 100%. The mass deposited onto the wire during time t can be expressed as $M(t) = 2\rho L\int_o^{w/2} f(x,t)dx = KIt$, where $Q = It$ is the deposited charge, K is the material constant[8], L is the wire length, ρ is the density, and $f(x, t)$ is the wire profile at time t (see Fig. 4.6).

4.3 Electrical and Thermal Properties of Normal Metal Micro-Electromagnets

To achieve the highest currents, micro-electromagnets are cryogenically cooled, and the current is pulsed to reduce heating. Micro-electromagnets were initially tested inside liquid nitrogen or liquid helium storage dewars. Five additional low-temperature setups were designed and built in the course of this research to add micro-electromagnets in vacuum to atomic beam systems. The results presented here were obtained from a low-temperature setup used to test micro-electromagnet mirrors and traps inside the He beam chamber at pressures of $p \sim 10^{-3}$ torr.

This low-temperature setup to cool micro-electromagnets inside the He beam chamber is discussed in detail in Chapter 5. The schematic diagram is shown in Fig.5.4. Here, we outline the basic features of this setup, illustrated in Fig. 4.8, which are necessary to understand how we tested electrical and thermal properties of micro-electromagnets.

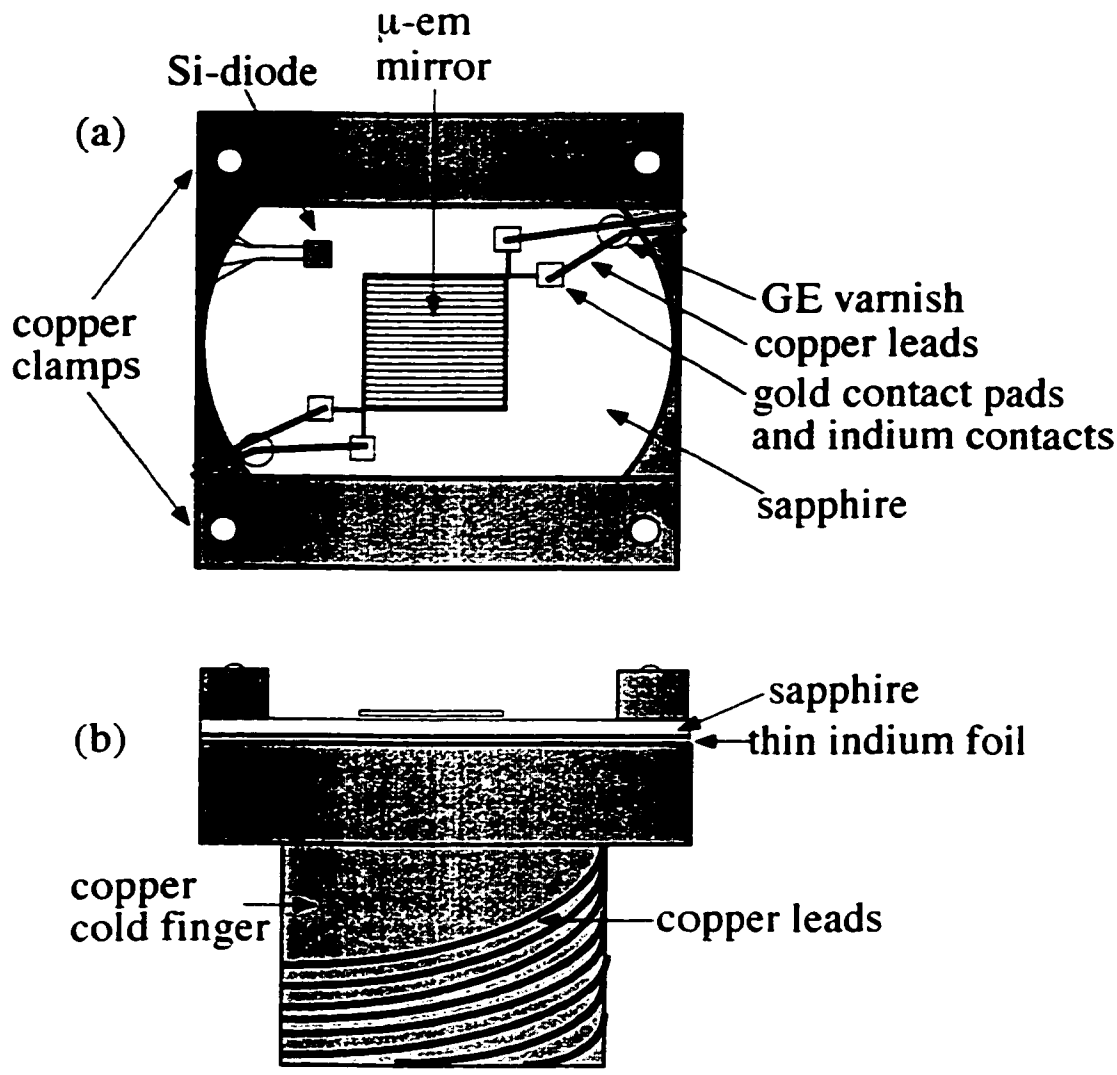

FIG.4.8 Schematic diagram of the micro-electromagnet mirror on sapphire substrate located at the end of a copper cold finger: (a) top view, (b) side view. The sapphire substrate is held with copper clamps to the cold finger. The copper leads of the micro-electromagnet mirror are wrapped around the cold finger and thermally anchored to it with GE varnish. A thin indium foil is placed between sapphire and copper to ensure good thermal contact. The temperature of the sapphire substrate is monitored with a Si-diode thermometer with Mn leads.

The cooling apparatus, illustrated in Fig.5.4 in Chapter 5, consists of a Precision Cryogenics Dewar, and a copper cold finger extending from the Dewar into the vacuum chamber of the He beam. The Dewar can be operated at liquid nitrogen and at liquid helium temperatures.

Figure 4.8 illustrates how the sapphire substrate of micro-electromagnets is mounted with copper clamps at the end of the cold finger. As shown in Fig.4.8 (a), the sapphire substrate temperature T_s was monitored with a Si diode thermometer[13] mounted near the micro-electromagnet. When the Dewar is filled with liquid cryogens, the measured temperature of the sapphire substrate at thermal equilibrium was $T_s \approx 16$ K for liquid helium and $T_s \approx 96$ K for liquid nitrogen. The time required to achieve this equilibrium temperature is ~ 4 hours for cooling from room temperature to $T_s \approx 96$ K, and ~ 30 minutes for cooling from $T_s \approx 96$ K to $T_s \approx 16$ K. As shown in Fig.4.8 (b), thin indium foil is placed between the sapphire substrate and the flat, polished copper surface at the end of the cold finger, to ensure good thermal contact between sapphire and copper. The copper leads of micro-electromagnets were wrapped tens of times around the cold finger and thermally anchored to it using GE varnish.

The copper leads of micro-electromagnets and the Mn leads of the Si diode thermometer were connected on the side of the vacuum space through a multi-connector cable, which gives us electrical access to these devices. A pulse generator and programmable Kepco power supply[14] with output up to 60V and 20A were used to energize micro-electromagnets. The total lead and contact resistance measured from the indium contacts of micro-electromagnets through the copper leads to the multi-connector cable was ~ 2 Ω; four-terminal measurements of current-voltage characteristic were performed.

---

[13] Available from Lake Shore Cryotronics, Inc., Westerville, Ohio, 43081, Tel. (614) 891-2243.

[14] Three Kepco power supplies with output up to 20V were connected in series, with one of them driving the other two.

Figure 4.9 (a) shows the measured dc current-voltage (I-V) curve for a micro-electromagnet mirror initially at temperature $T_s \approx 100$ K, in thermal equilibrium with the sapphire substrate. The mirror characteristics are area 2x2 mm^2, period $a = 48$ μm, $N = 83$ wires with wire width $w = 20$ μm, and thickness $h = 3$ μm. As shown in Fig.4.9 (a), the measured I-V characteristic is nonlinear because the micro-electromagnet mirror heats up and its resistance increases as the current is increased.

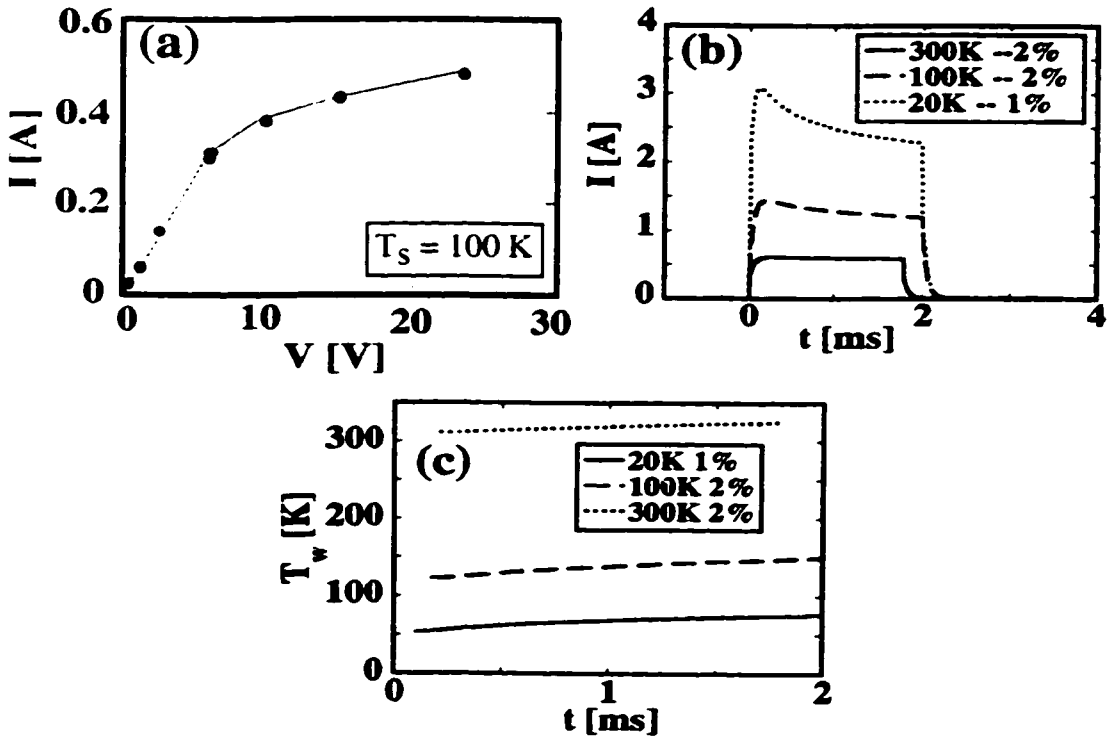

FIG.4.9 (a) Measured I-V characteristics for a mirror at initially at sapphire temperature T_s = 100 K for dc excitation. The surface B-field scales as B/I ~ 33 mT / A. (b) Mirror current $I(t)$ during a voltage pulse $V = 40$ V at temperatures and duty cycles indicated. (c) Mirror temperature $T_w(t)$ during a pulse $V = 40$ V, found using $R\ (\Omega) = 2.3 + 0.21T_w(\mathrm{K})$.

To study the heating of micro-electromagnet mirrors, the wire temperature $T_w(t)$ was found from the measured resistance $R(t)$ using the known temperature dependence $R(T)$. At $I = 0.5$ A in Fig. 4.9 (a), the calculated wire temperature is $T_w = 200$ K, still below room temperature. The thermal equilibration at this wire temperature and at dc current $I = 0.5$ A at a constant voltage $V = 21$ V takes ~ 10 minutes. This reflects the larger thermal time constant of the copper cold finger.

To reduce the average heat dissipation we pulsed the micro-electromagnet current. Voltage pulses were applied to micro-electromagnets initially at 300 K, 100 K and 20 K. Figures 4.9 (b) and 4.9 (c) show $I(t)$ and $T_w(t)$ for the same micro-electromagnet mirror as in Fig. 4.9 (a). As shown, mirror currents $I = 3$ A were achieved at 20 K using 1% duty cycle pulses. This current was limited by the voltage output (40V) of two Kepco power supplies connected in series[15], and not by the micro-electromagnet.

The surface magnetic field B_o produced by a micro-electromagnet mirror (Eqn. 2.3.3) was estimated assuming rectangular wires with wire width $w = 20$ μm and wire height $h = 3$ μm with uniform current density. For $I = 3$ A, this gives $B_o \sim 0.1$ T. In Chapter 5 and 6, we show that calculated magnetic fields of the mirror agree well with the measured values. As discussed in section 2.3, surface magnetic fields $B_o \sim 0.1$ T are sufficient to reflect 300 K thermal atoms at grazing angles and colder atoms at arbitrary angles.

[15] After this measurement, we have added a third Kepco power supply, used to obtain the I-V curve at the initial sapphire temperature of 100 K (Fig. 4.10 (a)).

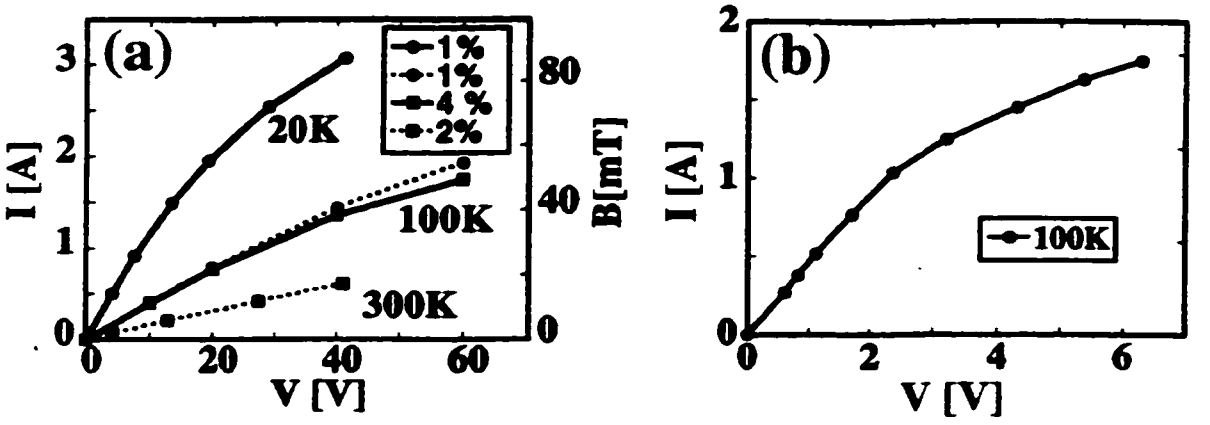

FIG. 4.10 (a) Measured I-V characteristics (left axis) and computed fields B (right axis) at the wire surface for a micro-electromagnet mirror at 300 K, 100 K, and 20 K pulsed at duty cycles indicated; mirror area 2x2 mm^2, a = 48 μm, w = 20 μm, h = 3 μm, and measured inductance L = 0.05μH, resulting in a $\tau = L/R$ time constant of ~ 10ns at low temperatures. (b) Measured trap I-V characteristics initially at sapphire temperature T_s = 100 K for dc excitation; the trap is shown in Fig. 4.3 (c).

As shown in Fig. 4.9 (c), for initial temperature T_s = 20 K of the sapphire substrate and 1% duty cycle, the wire quickly heats to 50 K at the beginning of the current pulse, then increases more slowly to 80 K during the pulse. The instantaneous power dissipated by the mirror reaches large values > 1 kW/cm^2. From the measured wire heating we estimate the effective thermal conductance G ~ 4 W/K from the wire to the heat sink, and the thermal time constant C/G ~ 3 μs, where $C = 1.3 \times 10^{-5}$ J/K is the wire heat capacity.

Figure 4.10 (a) shows the measured I-V curves (left axis) and computed fields B (right axis) at the surface of the micro-electromagnet mirror obtained at initial mirror temperatures 300 K, 100 K and 20 K for voltage pulses with duty cycles (< 5%) as indicated; mirror area is 2x2 mm^2, a = 48 μm, w = 20 μm, h = 3 μm and resistance R ~ 20 Ω at room temperature. The measured inductance L = 0.05 μH, results in a $\tau = L/R$ time constant of ~ 10ns at low temperatures. The inductance L of a mirror can be estimated from

$$LI^2/2 \approx A \int_o^\infty B_o^2 e^{-2kz}/2\mu_o dz, \qquad (4.2.1)$$

where A is the area of the mirror, B_o is the field at the mirror surface, and I is the current; for $A = 2\text{x}2\ \text{mm}^2$, $I = 1$ A, $B_o = 30$ mT, the estimated inductance $L \approx 0.1$ μH.

When the current in the micro-electromagnet mirror discussed in Fig. 4.10 (a) was pulsed at higher duty cycles (~ 20%), the time-averaged power at thermal equilibrium reached ~ 10 W for the entire mirror. For example, the measured peak current for a 1.5 ms pulse and duty cycle ~ 15 % was $I \approx 0.95$ A at the initial sapphire temperature $T_s = 100$ K.

Figure 4.10 (b) shows dc I-V characteristics obtained at initial temperature $T_s = 100$ K of the sapphire substrate for the micro-electromagnet trap shown in Fig. 4.3 (c). The trap wires have a wire width $w = 3$ μm and wire height $h = 1$ μm, with resistance $R \approx 1\Omega$. As shown, this device can carry a constant current of $I = 1.8$ A, which corresponds to a magnetic field at the top of the wire $B \approx 0.3$ T, and the field gradient at the surface of the wire $|\nabla B| \sim 10^3$ T/cm. This trap has burnt at a current $I \approx 2$ A.

Electrical currents in micro-electromagnets can be rapidly changed due to the small electrical and thermal time constants. In the limit of very short current pulses $\Delta t \sim 10$ ns applied to micro-electromagnets, very strong magnetic fields $B \sim 10$ T could be produced. With the fabricated micro-electromagnets, the maximum B-fields achievable could be estimated from a 'back of the envelope' calculation in the extreme limit of very short pulses $\Delta t \sim L/R$. Setting $I^2R\ \Delta t = C\ \Delta T$, where ΔT is the temperature rise in the wire during the pulse, and C is the wire heat capacity. For a mirror as discussed in Fig. 4.10 (a), taking $\Delta t \sim 10$ ns and $\Delta T = 1000$ K, gives $I \sim 100$ A, which corresponds to a surface field $B_o \sim 10$ T. Recently, [Mackay K. *et al.*, 2000] demonstrated that a wire loop made of copper on a silicon substrate with cross-sectional

area 100 μm x 10 μm and inner radius ~ 5 μm can carry pulsed currents I ~ 1000 A for τ ~ 10 ns, producing fields B ~ 10 T.

In conclusion, we have discussed the fabrication and testing of gold micro-electromagnets. This work begins the experimental development of adaptive atom-optical elements, which exploit microfabrication and cryogenics. A possible way to achieve higher magnetic fields and gradients is fabricating devices with resistance ratios R(300K)/R(4K) ~ 10^4 using high purity wires; in the present devices R(300K)/R(4K) ~ 10, limited by impurities. Higher purity could be achieved by etching metal foils or by improving electroplated and evaporated metals. Wires could be made from Au, or from Cu and Ag with a layer of Au on top to prevent chemical degradation. The current density achieved in this way would be higher, corresponding to higher magnetic fields B ~ 10 T and gradients B ~ 10^5 T/cm.

4.4 Electrical Properties of Superconducting (Nb) Micro-Electromagnets

To measure the maximum current attainable in superconducting micro-electromagnets, we have fabricated niobium (Nb) micro-electromagnet mirrors on silicon substrates. The expected maximum current densities in superconductors are 10^{-7} A/cm^2 [*Materials at Low Temperatures* (eds. Reed R.P. and Clark A.F.), 1983], which is lower than what is achievable in normal metals, like gold, copper and silver.

Testing of Nb mirrors was performed in the Shubnikov de Haas Dewar [Rimberg A.J., 1993] at temperatures from T =1.5 K to T = 4.2 K and perpendicular magnetic fields up to several Tesla. The mirror was GE varnished into the standard chip carrier used in the Westervelt group. Indium contacts and copper leads were used to connect the mirror contact pads to the pads of the chip carrier. All measurements were four-terminal.

The critical current I_{crit} of the Nb wires as a function of the external magnetic field B at $T = 4.2$ K is shown in Fig. 4.11 (a). The mirror characteristics are area 2 x 2 mm^2, $a = 18$ μm, $N = 223$, $h = 0.3$ μm and room temperature resistance $R \approx 20$ kΩ. At $B \approx 1.2$ T the transition to a normal phase occurs. The critical current I_{crit} as a function of temperature T at $B = 0$ is shown in Fig. 4.11(b). Current densities up to ~ 3 x 10^6 A/cm^2 were achieved at $T \approx 1.5$ K; the corresponding field at the mirror surface is $B_o \approx 3$ mT.

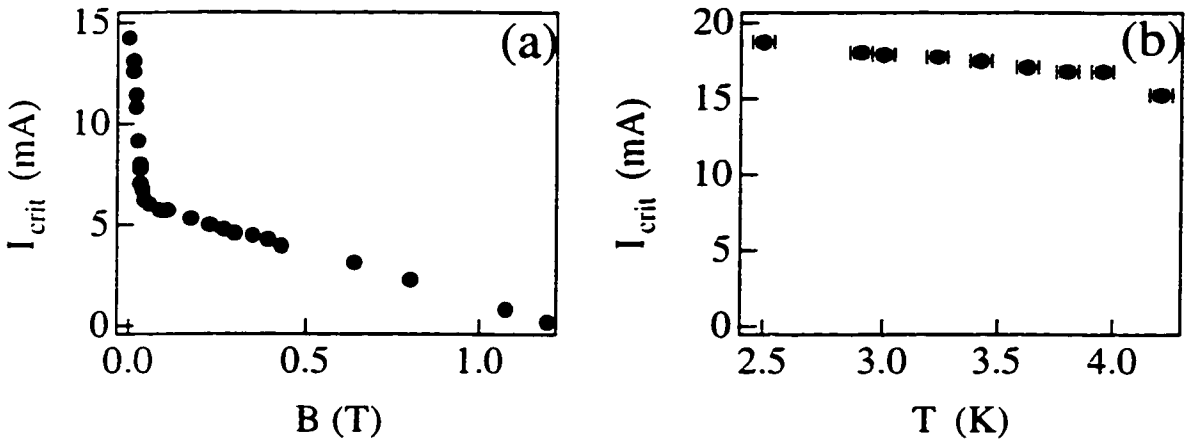

FIG.4.11 (a) Critical current I_{crit} vs. the external magnetic field B for a mirror with area 2 x 2 mm^2, $a = 18$ μm, $h = 0.3$ μm; (b) Critical current I_{crit} vs. temperature at $B = 0$.

Chapter 5

DEFLECTION OF A THERMAL He BEAM

In this Chapter we describe the use of micro-electromagnet mirrors to deflect a beam of metastable He* atoms[1]. The spatial distributions of deflected atoms were measured as functions of atom-mirror separation and mirror current. The magnitude of the magnetic field of the mirror was calibrated by deflecting atoms in the presence of an added external bias field. By exploiting time-dependent mirror fields, we have narrowed the deflected peak distributions. The measured results agree well with numerical simulations assuming a simple exponentially decaying field.

5.1 Experimental Setup

In section 5.1 we describe the experimental setup to deflect a metastable helium beam from a cooled micro-electromagnet mirror. First, we outline the main parts of the experimental setup, and then we discuss the individual components in more detail. A photograph of the experimental setup is shown in Fig. 5.1, and the experiment is illustrated in Fig. 5.2. The experimental setup can be divided into two main parts :(*i*) the metastable He* beam setup (Fig.5.1 (a)), and (*ii*) the low-temperature setup to integrate the mirrors with the He beam setup (Fig. 5.2 (b)).

[1] Symbol * stands for metastable atoms.

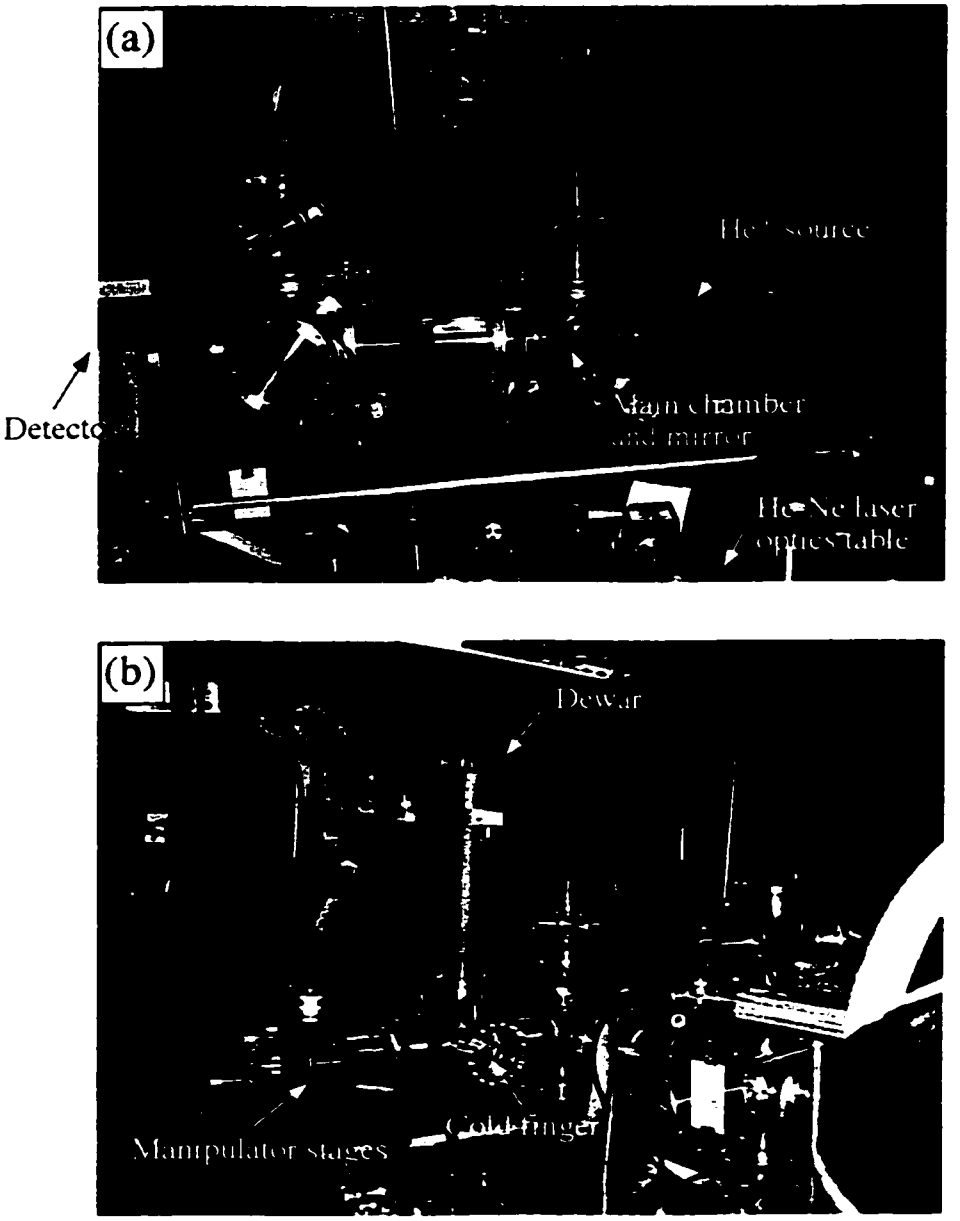

FIG.5.1. Photograph of the experimental setup. (a) He beam source, main chamber where the mirror is installed, and a 1.6 m long vacuum chamber for atom travel to the detector located on the far left. The detector consists of a multi-channel plate, a phosphorous screen and a CCD camera. (b) view of the cooling system including a dewar, and the manipulation stages. The copper cold finger, located inside the vacuum space can be partly seen through the glass window.

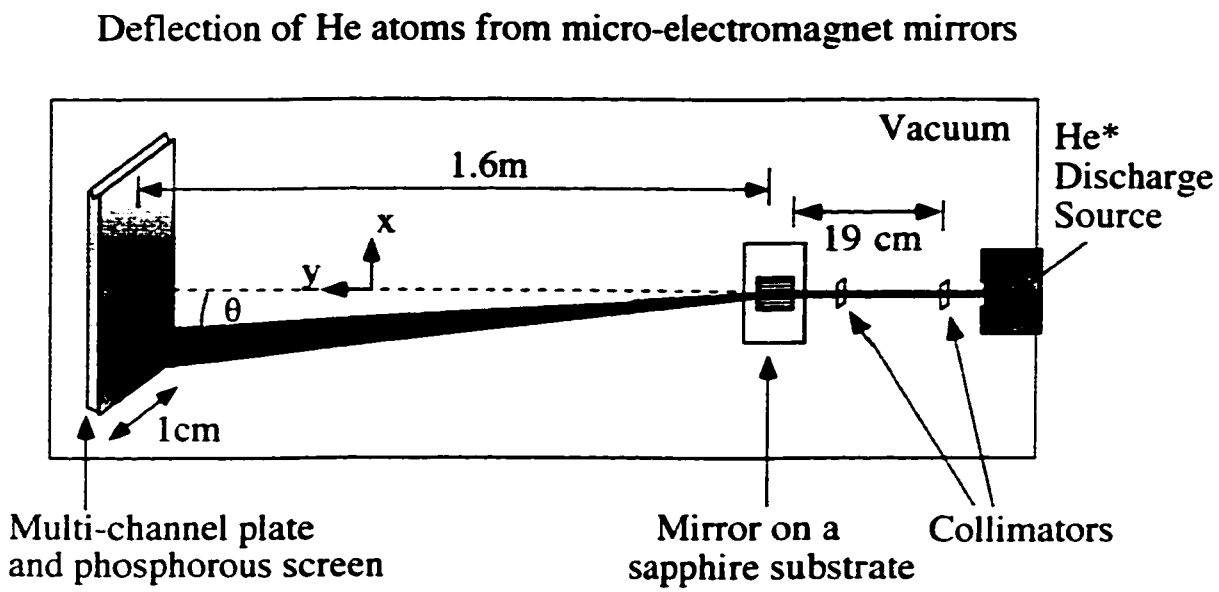

FIG. 5.2 Schematic diagram of the experimental setup to deflect metastable He atoms at mrad angles θ from a micro-electromagnet mirror. The He atoms are produced in a pulsed discharged source, and detected by a multi-channel plated detector and a fluorescent phosphorous screen located 1.6 m from the mirror. Two slits 5 μm x 0.5 mm are used to collimate the He atoms into a ribbon, parallel to the micro-electromagnet mirror. The micro-electromagnet mirror is located 19 cm from the source, along the direction of atom travel. The mirror is fabricated on a rectangular sapphire substrate.

The first part of the experimental setup is the He beam setup (Fig.5.1 (a)). It includes the He* source, the position-sensitive detector, the main vacuum chamber for He* atom travel from the source to the detector, and the optics table with lasers and the supporting laser optics. The micro-electromagnet mirror, located in the main chamber, can be seen through the glass window of the main chamber in Fig. 5.1 (a). The position-sensitive detector consists of a multi-channel plate, a phosphorous screen and a CCD camera. Previously built by John Lawall [Lawall J.,1993; J. Lawall and M. Prentiss, 1994], the He beam setup was originally used to realize an atomic beamsplitter based on laser light.

The second part of the experimental setup is the low-temperature setup to cool the mirrors (Fig.5.1 (b)). This setup was built to fit in the existing He beam setup. It consist of a liquid helium Dewar and a cold finger to cool the mirrors, and a set of manipulation stages to orient the mirror with respect to the He beam.

A schematic diagram of the deflection of metastable He* atoms from a micro-electromagnet mirror is illustrated in Fig. 5.2. Metastable He* atoms are produced from He atoms in the ground-state inside a pulsed discharge source [Lawall J., 1993]. Two slits 5 μm x 0.5 mm are used to collimate the He atom beam into a ribbon, parallel to the micro-electromagnet mirror. The beam travels ≈19 cm from the source to the mirror which was fabricated on a rectangular sapphire substrate. The spatial spread of the beam when it reaches the mirror was ≈15 μm in the z direction, and ≈1 mm in the x direction (see Fig.5.2). The mean velocity of the He* beam was v = 1800 m/s corresponding to temperature T = 270 K. The relative spread in the longitudinal velocities was $\delta v_L / v \approx 1/3$ and the spread in the transverse velocities was $\delta v_T \approx 0.2$ m/s . As will be described below, this large spread in the longitudinal velocities of the beam will be the reason for the spatial broadening of the deflected beams. The He* atoms are detected by a micro-channel plate, a phosphorous screen and a CCD camera located a distance1.6 m from the mirror (Fig.5.2). When a metastable He* atom hits the multi-channel plate, an

avalanche of electrons is produced in the multi-channel plate. This electron current is then converted into an image on a fluorescent phosphorous screen. The fluorescence is imaged by a CCD camera and the image is displayed on the computer screen. In this way, we were able to monitor the arrival of individual He* atoms after they had interacted with the micro-electromagnet mirror. The long length of atomic travel in our experiment permitted high-resolution detection of small deflections (resolution ~ 0.05 mrad).

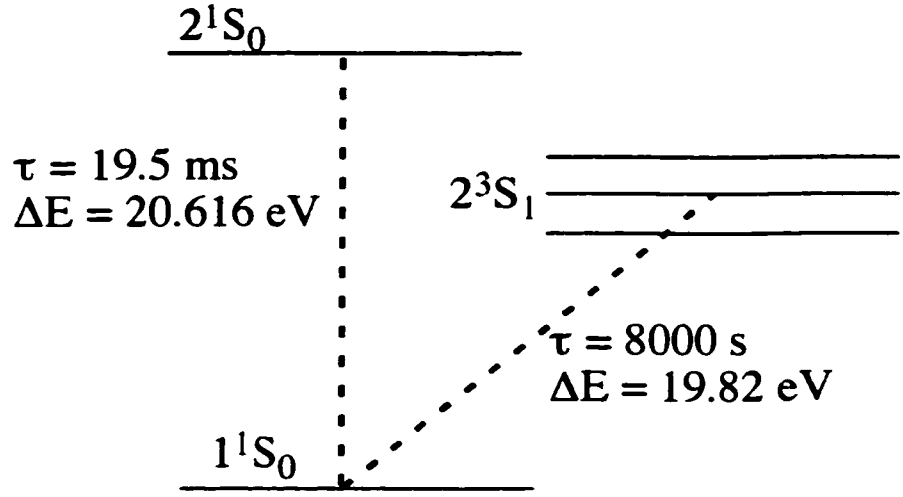

FIG. 5.3 Schematic diagram of the He atom level structure, with only those levels included that are relevant in this experiment. The different levels are given in the spectroscopic notation $n^{2S+1}L_J$, where J is the quantum number for the total angular momentum, L is the quantum number for the orbital angular momentum, and S is quantum number for the spin. The He atoms in the ground-state is 1^1S_0 are excited into two metastable states are 2^1S_0 and 2^3S_1 with lifetimes τ = 19.5 ms and τ = 8000 s, respectively. The energy difference between the excited states and the ground state is ΔE.

The He* beam consists of excited He* atoms in the singlet 2^1S_0 and the triplet 2^3S_1 states. The structure of the relevant He levels is illustrated in Fig 5.3. The states are presented in the spectroscopic notation $n^{2S+1}L_J$, where n is the principal quantum number, J is the quantum number for the total angular momentum, L is the quantum number for the orbital angular momentum, and S is quantum number for the spin. The excited states

are produced by flowing the He gas through a ceramic vessel and exciting the 1^1S_0 ground-state atoms with rf discharge [Lawall J., 1993]. The excited states are metastable, with lifetimes $\tau = 19.5$ ms for 2^1S_0 and $\tau = 8000$ s for 2^3S_1.

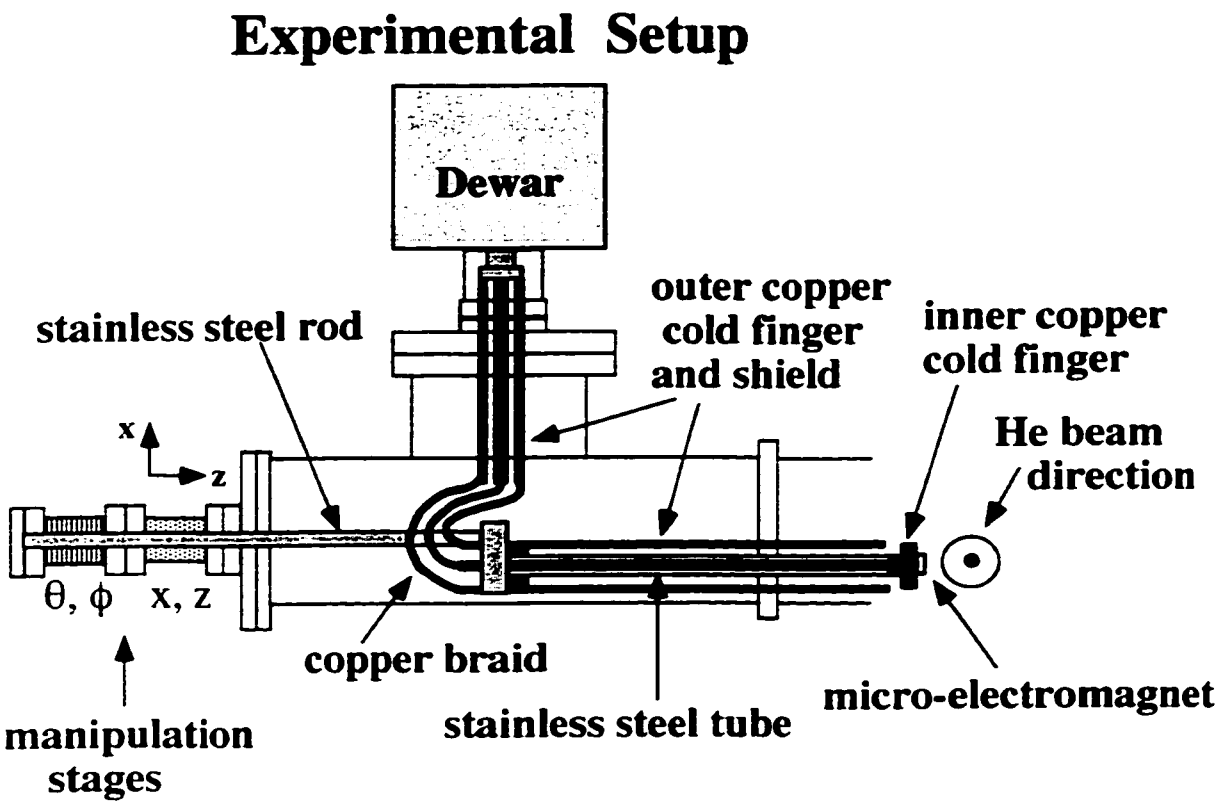

FIG. 5.4 Experimental setup used to integrate micro-electromagnet mirrors with the He* beam. A liquid helium Dewar is used for cryogenic cooling of mirrors. Rotation and translation stages allow for the movement of the mirror with respect to the beam.

5.2 Low-Temperature Micro-Electromagnet Mirror Setup

In section 5.2, we describe in more detail the low-temperature setup to cool micro-electromagnet mirrors and integrate them with a He* beam setup. Figure 5.4 shows a schematic diagram of the Dewar and the copper cold finger to cool the mirrors, and the manipulation stages to orient the mirrors with respect to the He* beam.

The sapphire substrate of the micro-electromagnet mirror was tightly held with copper clamps against the end of a flexible copper cold finger of length $L \approx 0.5$ m and diameter $d \approx 1.25$ cm. The other end of the cold finger was cooled by liquid helium inside a Precision Cryogenic[2] Dewar.

A schematic diagram of the Dewar, which was designed particularly for this experiment, is shown in Fig. 5.5. The Dewar is designed with both a helium and a nitrogen can. The nitrogen can is attached to a radiation shield which completely encloses the helium can. A copper cold finger extends from the liquid helium can of the dewar into vacuum space, and is surrounded by an aluminum radiation shield extending from the liquid nitrogen can. The Dewar can be opened to atmosphere by opening the evacuation valve on the side wall of the Dewar, or by opening a 2 3/4" flange on the bottom (Fig.5.5).

The cold finger was designed with a low thermal resistance $\propto \kappa L/d^2$, where κ is the thermal conductivity of copper, L is the length and d is the diameter. The minimum length $L \approx 0.5$ m and the maximum diameter $d \approx 1.25$ cm were in our case constrained by the He* beam setup. The flexible part of the cold finger was made from a copper braid that allowed us to orient the micro-electromagnet mirror with respect to the atom beam. The copper current leads of the micro-electromagnet mirror were heat sunk to the cold finger by wrapping them tens of times around the cold finger and thermally anchoring them with GE varnish. An outer copper shield extending from the liquid nitrogen bath of the Dewar, wrapped in a highly reflective mylar foil, was used to shield the inner cold finger from 300 K black body radiation.

---

[2] Precision Cryogenic Systems, Inc., 804 Rockville Road, Indianapolis, Indiana 46214, Tel: 317/273-2800. http://www.precisioncryo.com/.

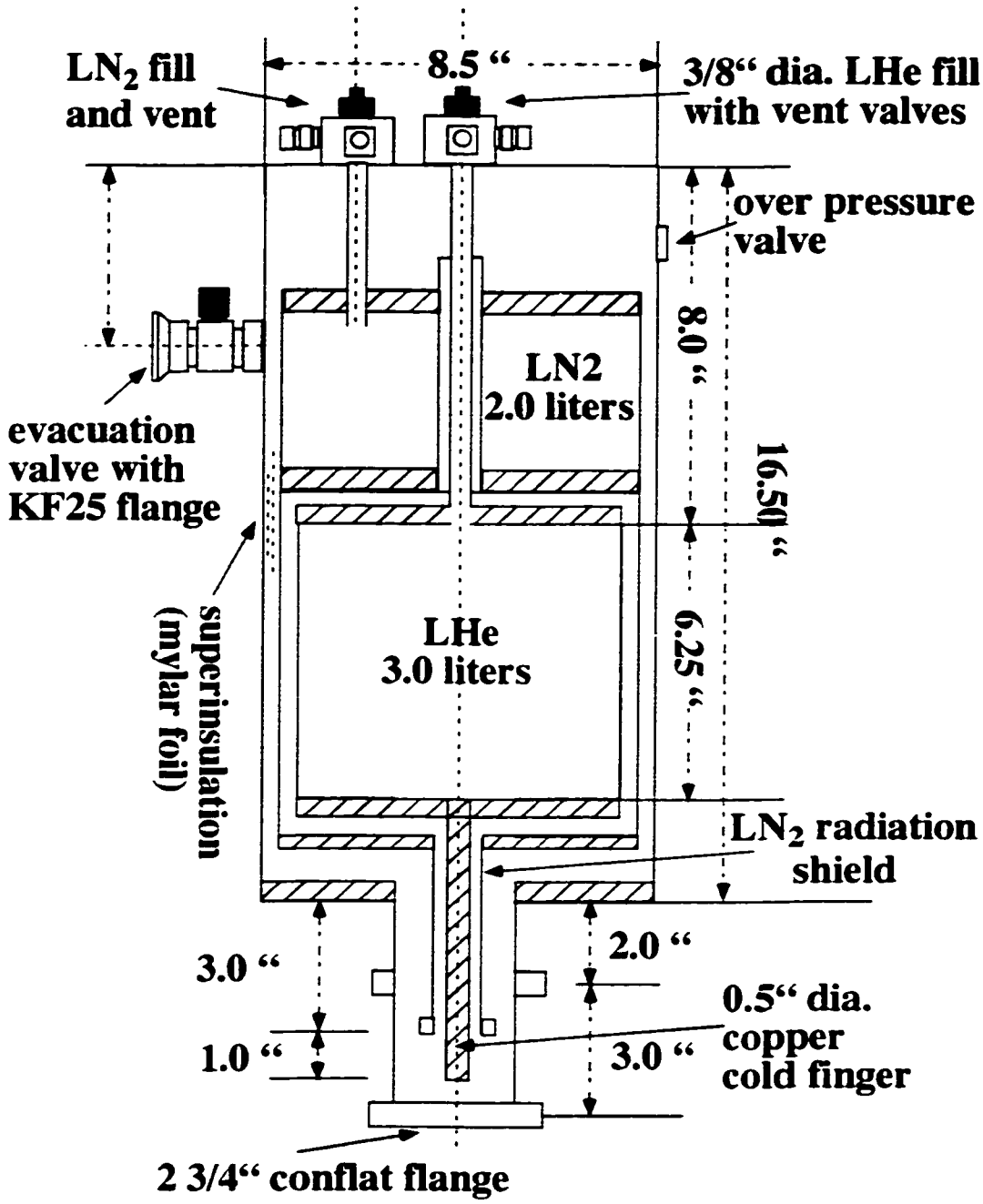

FIG. 5.5 Liquid helium dewar used for cryogenic cooling of micro-electromagnets. A copper cold finger extends from the LHe can of the dewar into vacuum; an aluminum radiation shield surrounding the cold finger extends from the LN_2 can of the dewar.

The position of micro-electromagnets with respect to the beam was controlled to μm-scale precision with a set of manipulators from MDC[3]. They allowed for x and z translation and for rotation around the x and y axes (see Fig.5.4). Special care was taken to minimize the 300 K thermal load from the manipulation stages to the cold finger at 4 K, while providing enough mechanical support. The manipulation stages were first connected using a bellows to a solid stainless steel rod ~ 0.25 m long which was further clamped to a ~ 0.25 m long stainless steel tube with ~ 0.5 mm thin walls. The tube was then clamped and heat sunk to the 77 K outer cold finger at one end, and connected to the inner cold finger at the other end using a teflon spacer.

The sapphire substrate temperature T_S was monitored with a Si diode thermometer from Lake Shore Cryotronics, mounted close to the to the micro-electromagnet mirror. Four Mn leads were used to connect the Si diode to the readout unit at 300 K. The mirror leads were wrapped around the cold finger many times to minimize the thermal load. For liquid He cooling $T_S = (16 \pm 1)$ K and for liquid N_2 $T_S =$ (96 ± 1) K. The liquid helium hold time of the Dewar is consistent with the estimates of the thermal load on the cold fingers and the Dewar cooling capacity. The measured liquid helium hold time of the Dewar with the copper cold finger and the manipulation stages attached (Fig. 5.4) was ≈ 4 hours, suggesting that the thermal load was $P \approx 0.75$ W (since the cooling capacity of one liter of liquid helium is ≈ 1 W/hour). This is consistent with the power load estimated from the black body radiation, described below.

[3] MDC, Vacuum Products Corporation, Hayward, CA 94545. Tel. (510) 265-3500.

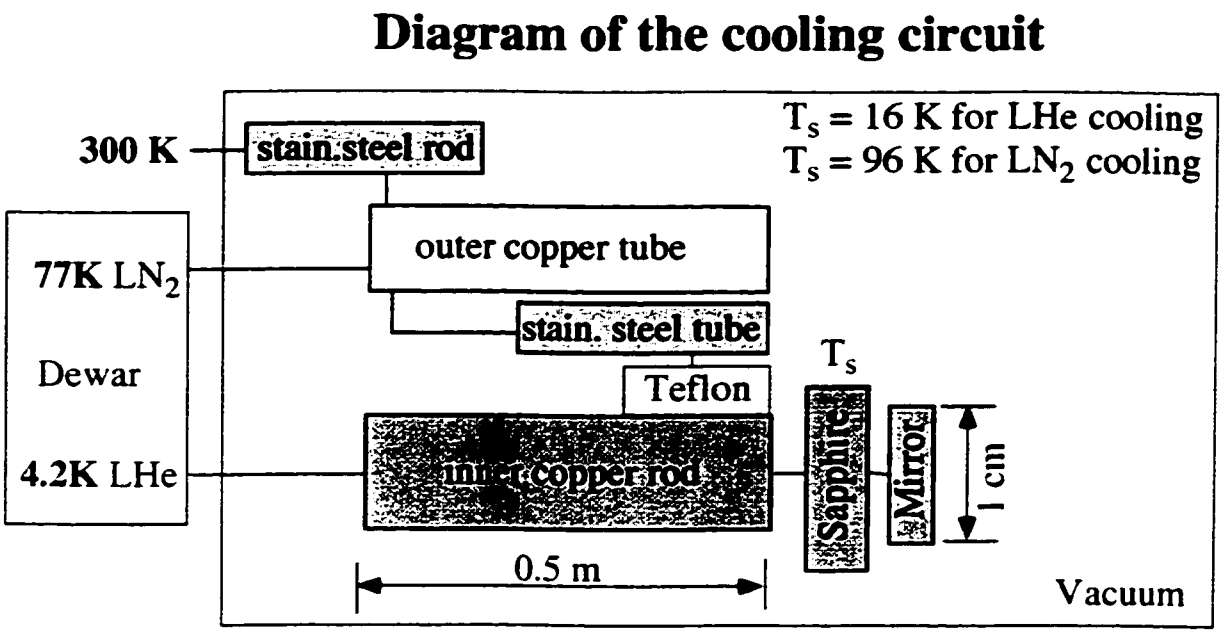

FIG.5.6 Diagram of a thermal circuit to cool micro-electromagnets. The thermal load on the inner copper cold finger comes from: (*i*) the black body radiation at liquid nitrogen temperature, (*ii*) the black body radiation at room temperature onto the sapphire substrate, and (*iii*) from the contact through teflon to the stainless steel tube. The thermal load on the outer copper cold finger comes from: (*i*) the black body radiation at room temperature, and (*ii*) from the stainless steel rod at room temperature.

A diagram of the cooling circuit is shown in Fig.5.6 to illustrate in more detail the thermal loads on the inner copper rod and outer copper shield (tube). The thermal load on the inner copper rod comes from two sources (*i*) the black body radiation at liquid nitrogen temperature, (*ii*) the black body radiation at room temperature onto the sapphire substrate. The equilibrium temperature at the end of the cold finger $T = 4.2\text{K} + \Delta T$, can be estimated from

$$P(\text{radiated power}) = \sigma_{SB}(77\text{K})^4 A_{77} + \sigma_{SB}(300\text{K})^4 A_{300} \approx \kappa A\, \Delta T/L, \qquad (5.2.1)$$

where P is the power of the total black body radiation reaching the inner cold finger, A_{77} and A_{300} are the surface areas of the cold finger exposed to 77K and 300K black body radiation, respectively; A is the cross-sectional area of the cold finger, κ is the thermal conductivity of Cu at low temperatures, L is the length of the cold finger, ΔT is the temperature difference from the liquid helium bath to the end of the cold finger; σ_{SB} is the Stefan-Boltzmann constant, $\sigma_{SB} = 5.67 \times 10^{-8}$ W/m^{2}K^4. Useful numbers to remember in cryogenic experiments are the black body radiation power per unit area for the black body radiation at 77K and at 300K: $\sigma_{SB}(77K)^4 = 0.4$mW/cm^2, $\sigma_{SB}(300K)^4 = 50$mW/cm^2. In our case, L=0.5m, A=$r^2\pi$ = 1 cm^2, $A_{77} = 2r\pi L$= 200 cm^2, A_{300}= 20 cm^2, and κ(4K) ≈ 10000 W/mK. The total power load on the inner cold finger is then P = 1 W, corresponding to an estimated $\Delta T \approx$ 1K.

The micro-electromagnet mirror used in this experiment had an area 0.5x1 cm^2, period a = 200 μm, wire width w = 91 μm and wire height h = 12 μm. The choice of the mirror period a = 200 μm was determined from the condition that the spatial spread of the He* beam in the z-direction (see Fig.5.2) be smaller than the exponential decay length $1/k = a/2\pi$ of the magnetic field of the mirror. In our case, the size of the He* beam as it reaches the mirror in the z- direction of ≈ 15 μm is smaller than $1/k$ = 32 μm.

The mirror was fabricated on a rectangular sapphire substrate with thickness d = 3 mm along z-direction and width l = 1.5 cm along y-direction (see Fig.5.2). Large thickness was chosen to ensure the sapphire surface remains flat after clamping and small width, just large enough to fit the mirror and the contact pads. was chosen to minimize the atom-mirror separation. The resistance of the mirror was R = 20 Ω at T_s = 300 K and R = 5 Ω at T_s =100 K, with a calculated inductance L ~ 0.125 μH and a time constant τ = L/R ~ 25 ns.

5.3 Measurement Techniques

In section 5.3 we describe (*i*) the alignment of the mirror with respect to the He* beam using a red He-Ne laser beam (see Fig.5.1 (a)) and an infrared laser beam [Lawall J., 1993], and (*ii*) the data acquisition system used for the deflection of He* atoms. In particular, the current in the micro-electromagnet mirror was pulsed and the pulsing of the mirror was synchronized with the pulsing of the He* source and the pulsing of the detector.

The atom beam was incident parallel to the mirror plane and parallel to the wires in the array to help adiabaticity. As described in Chapter 3, the direction of the magnetic field of the mirror changes least along the wires, which is favorable for adiabaticity. The alignment of the mirror parallel to the beam was done using a red He-Ne laser and the same alignment procedure was repeated using a LNA (Lanthanum-Neodymium-Hexaluminate) laser, both previously set to be perpendicular to the He atom beam by [J. Lawall, 1993].

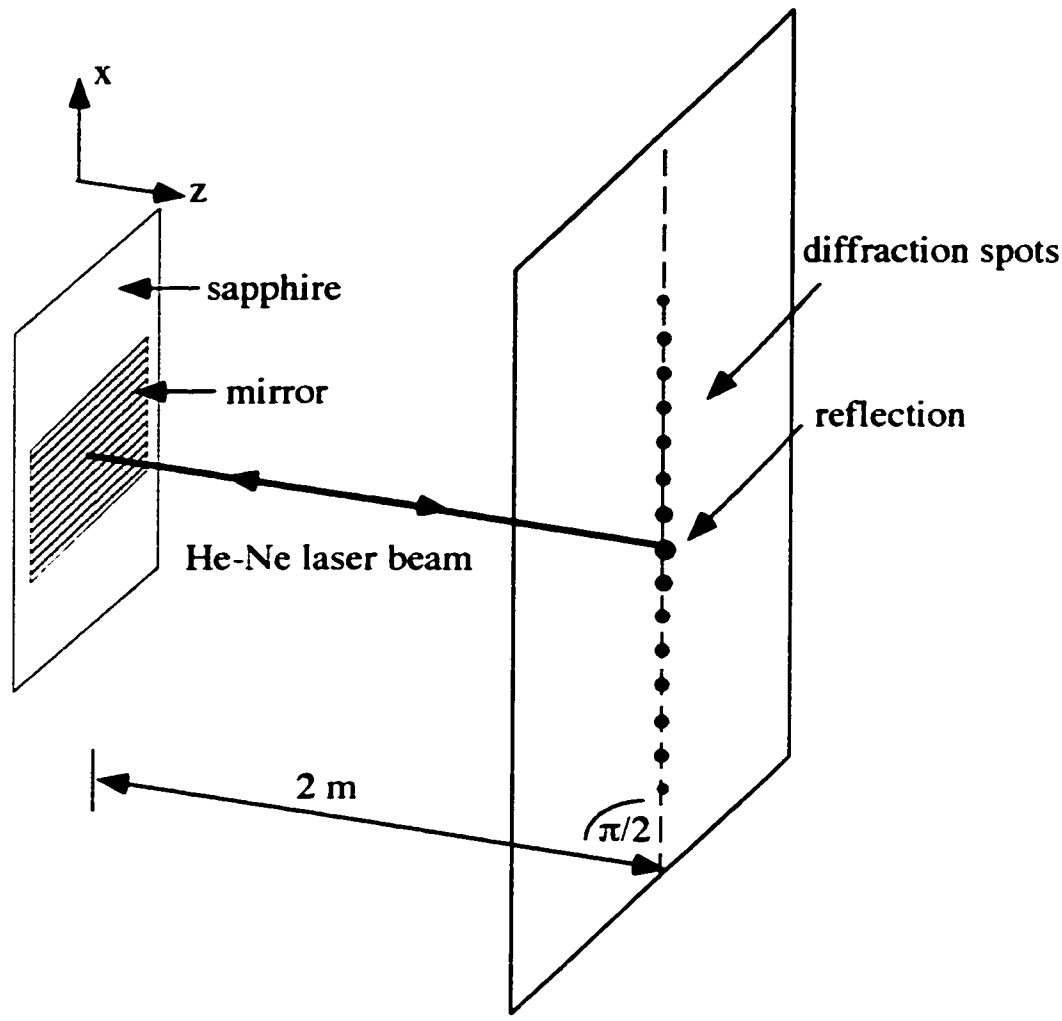

FIG.5.7 Schematic diagram of the reflection and diffraction of a laser beam, normally incident on the sapphire substrate and the wires in the micro-electromagnet mirror.

The alignment procedure is illustrated in Fig.5.7. Because the mirror is metallic it can reflect light specularly. Also, because the mirror geometry consists of an array of equally spaced parallel lines, the mirror can serve as a diffraction grating for laser light. By shining a laser beam onto the micro-electromagnet mirror, we were able to observe both the reflected laser beam, and a series of diffraction spots projected on a vertical surface at a distance $D \sim 2$ m (Fig.5.7). For the wire separation $a/2 = 100$ μm, the diffraction spots are separated by $\Delta x \approx (D \lambda) / (a/2) \sim 1$ cm in the x –direction, where λ is the wavelength of the laser light. For red laser light $\lambda = 0.6$ μm and $\Delta x \approx 1.2$ cm, and for infrared laser light $\lambda = 1$ μm and $\Delta x \approx$ 2cm. When the sapphire substrate and the wires in the micro-electromagnet mirror are perpendicular to the laser beam, the reflected laser beam coincides with the incident laser beam, and the diffraction spots are aligned in the x-direction (Fig.5.7). In this way, we were able to align the mirror parallel to the beam to an angular precision of ~ 0.2 mrad, which was limited by the diameter of the reflected laser beam.

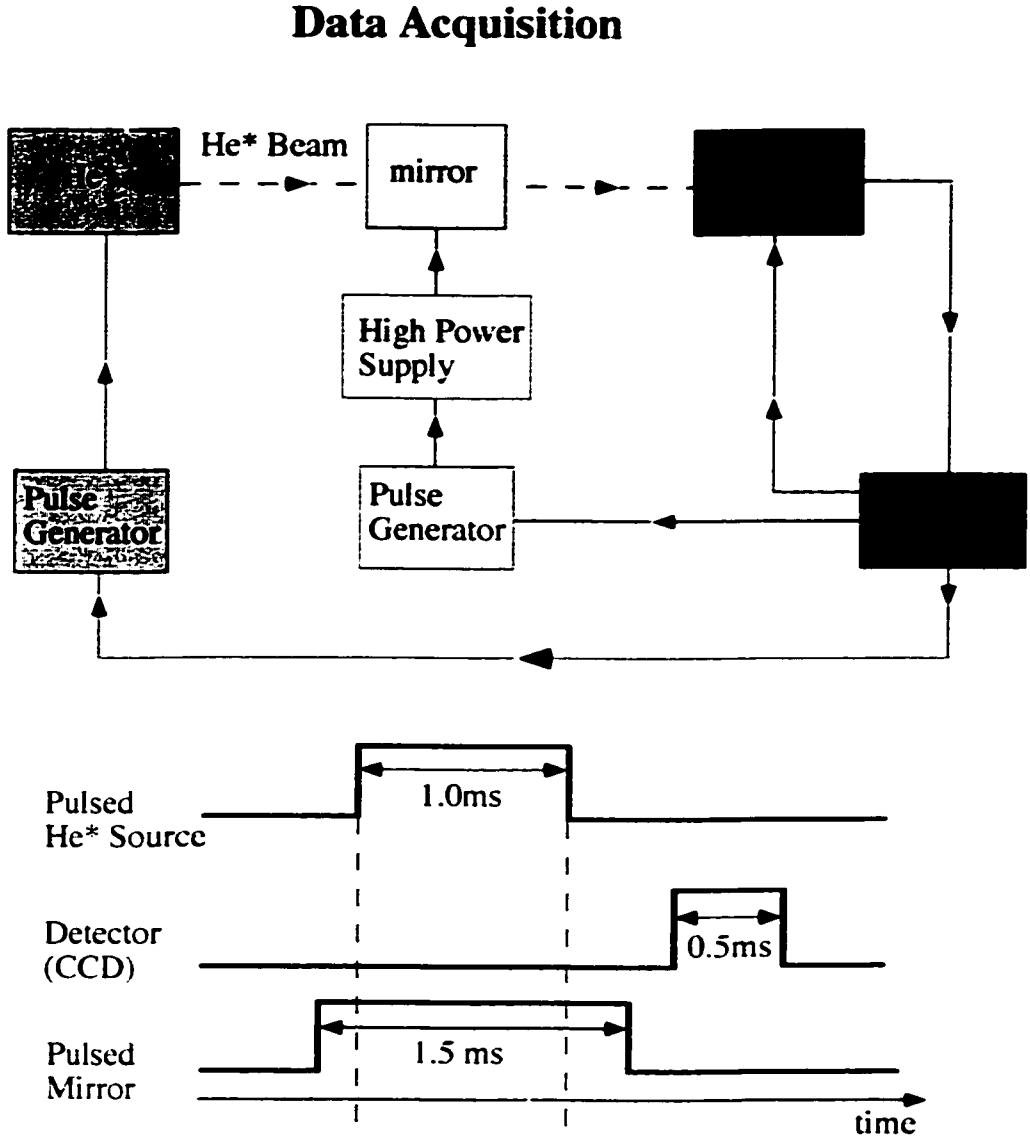

FIG.5.8 Schematic diagram of data acquisition. The pulsing of the source, the mirror and the detector was computer synchronized and controlled. The source pulse duration was up to 1.5 ms. The pulse sequence shown above was repeated every 30 ms.

The data acquisition setup is illustrated in Fig. 5.8. The triggering pulses to synchronize the He* atom source, the mirror and the detector were computer generated and controlled [Lawall J., 1993]. A pulse of current was applied to the mirror for 1.5 ms with either a flat or ramped profile. The He* atom source was pulsed on for up to 1.5 ms, and the atoms were detected during a 0.5 ms exposure using a CCD camera. This pulse sequence was repeated every 30 ms. The pulse generator used for the mirror allowed us to adjust the pulse width, separation and delay; this adjusted pulse was sent to the input of a programmable Kepco power supply with output 20V and 20A. Additional two Kepco power supplies with the same specifications, were connected in series with the first one, to provide higher voltage pulses to the mirror.

5.4 Deflection results as a Function of Mirror Current and the Beam-Mirror Separation

In section 5.4 we show the experimental results demonstrating that micro-electromagnet mirrors can be successfully used to deflect He* atoms. We have deflected He* atoms and measured the spatial distributions of deflected atoms as functions of atom-mirror separation and mirror current. The measured results agree well with a simple picture of an exponentially decaying magnetic field of the mirror. We have also calibrated the magnitude of the magnetic field of the mirror by deflecting atoms in the presence of an added external bias field. The measured magnetic field of the mirror agrees well with calculated values.

The He* atoms in the triplet 2^3S_1 state with nonzero magnetic quantum numbers m_J can be deflected by the magnetic field of the mirror. As described above, the 2^3S_1 state has quantum numbers J = 1, L = 0, S = 1, and $m_J = 0, \pm 1$, with the Landé g-factor g=2.

The $m_J = \pm 1$, 2^3S_1 states will be deflected, while the $m_J = 0$, 2^3S_1 state as well as the $m_J = 0$, 2^1S_0 state will be unaffected by the magnetic field.

The expected He* deflection angles θ of the triplet 2^3S_1 state can be estimated in the impulse approximation when atoms move in the z-direction significantly less than one exponential decay length of the magnetic field of the mirror, defined as $1/k = a/2\pi$, while interacting with the mirror. This condition can be expressed as $\theta d << 1/k$, where θ is the deflection angle and $d = 1$ cm is the mirror length along y –direction (see Fig.5.2). All the results described below were obtained in the impulse regime. The deflection angle θ can be estimated from

$$\theta = (2\mu_B d B_o k e^{-kz})/(mv^2), \tag{5.4.1}$$

where z is the atom-mirror separation, defined as the normal distance from the mirror surface to the center of the atom beam. The atoms interact with the magnetic field of the mirror field for a short time $\tau \sim d/v = 5.5$ μs. In our case, for $I = 1$ A, the surface field $B_o \approx 5$ mT, and $\theta \approx 0.3$ mrad for $z = 50$ μm and $m_J = \pm 1$. This model is in excellent agreement with experimental results shown below.

The experimental result to deflect the He* atoms are shown in Figure 5.9 with a schematic diagram of the He* atom deflection (Fig.5.9 (a)), the measured deflection angles θ of the He* atoms (Fig.5.9 (b)), and the angular splitting $\Delta\theta$ between the $m_J = 1$, and the $m_J = -1$ states, $\Delta\theta = |\theta(m_J = 1)| + |\theta(m_J = 1)|$ (Fig.5.9 (c)). The atom-mirror separation z in Fig. 5.9 (a), is defined as the distance between the mirror surface and the center of the atom beam. This distance was measured from the reading of the translator stage in the z-direction, in the following manner: we translated the cold finger and the mirror in the z-direction far enough to intersect the He* atoms and block the passage of the He* atoms to the detector. The distance z = 0 was then set as the reading on the translator when the mirror just started to block the He* beam and when no He* atoms

were detected. The error in the measurement of atom-mirror separation z, obtained in this way, was $\Delta z = 3\ \mu m$.

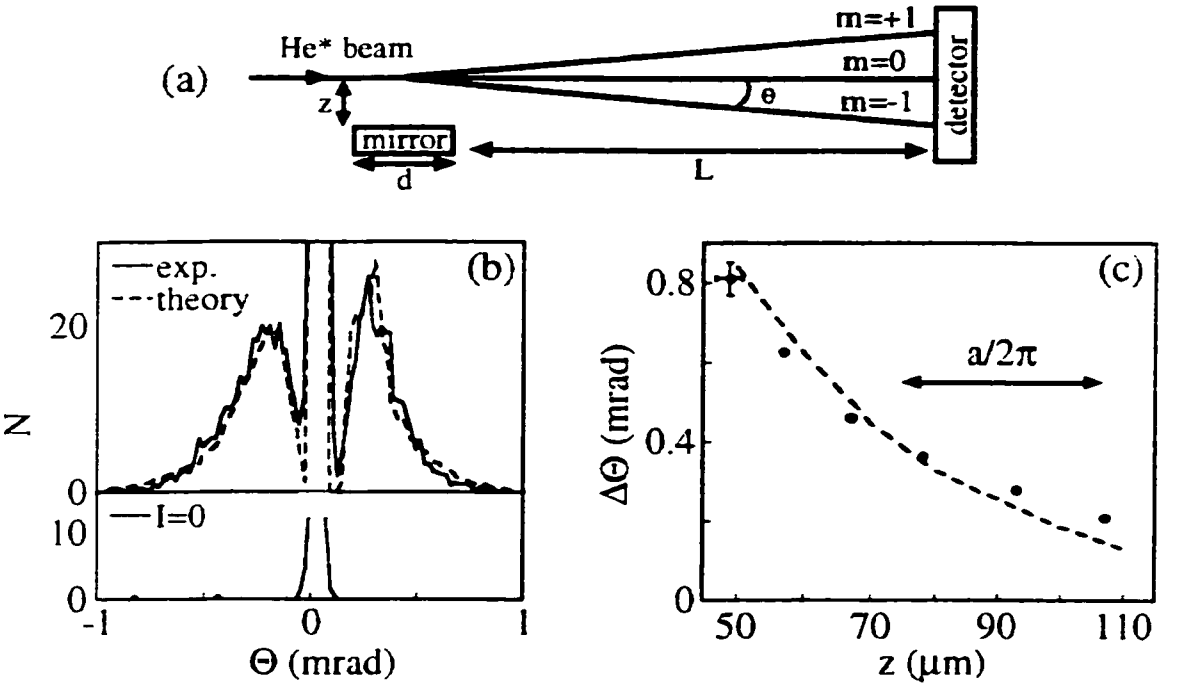

FIG. 5.9 (a) Schematic diagram of the experimental setup used to deflect He* atoms with a micro-electromagnet mirror; $L = 1.6$m, $d = 1$ cm. (b) The spatial distribution of deflected atoms after interacting with the mirror field at $I = 1.04$ A and $I = 0$. Solid line is the raw experimental data; dashed line is a numerical calculation which assumes an exponentially decaying field. (c) Angular splitting $\Delta\theta$, described in text, of He* atoms as a function of the atom-mirror separation z. Dots are experimental measurements; dashed line is a numerical calculation. Representative error bar is shown.

Figure 5.9 (b) shows the spatial distribution of He* atoms detected after interacting with the mirror carrying a current I = 1.04 A (top) and I = 0 (bottom). The separation between the center of the beam and the mirror was z = 58 ± 3 μm. Solid line is the raw experimental data, and dashed line is a numerical fit to the data. As expected theoretically, several interesting properties can be observed from this graph:

(*i*) With the mirror current on, the He* beam is expected to split into three peaks corresponding to three different magnetic quantum numbers $m_J = \pm 1$ and $m_J = 0$. As shown in Fig.5.9 (b), three peaks arise when the mirror is on: the central peak from the unaffected atoms (m_J = 0 state), the right peak from the repelled atoms (m_J = 1 state), and the left peak from the attracted atoms (m_J = -1 state).

(*ii*) The measured deflection angles θ of the $m_J = \pm 1$ He* atoms agree well with the estimated values from Eqn. (5.4.1). From the data in Fig.5.9 (b), the deflection angle of the peak in the atomic distribution for $m_J = \pm 1$ is θ = 0.28 mrad, for I = 1.04 A and z = 58±3 μm. The theoretical value θ_{th} from Eqn. (5.4.1), θ_{th} = 0.24 mrad for I = 1.04 A and z = 58 μm, is consistent with the measured value.

(*iii*) The deflection peaks in Fig. 5.9 (b) of the $m_J = \pm 1$ states are spatially broadened compared to the central peak, which corresponds to the unaffected m_J=0 states. This spatial broadening of the deflected peaks results primarily from the spread in the longitudinal atom velocities $\Delta v_L / v \approx 1/3$. The expected angular spread $\Delta\theta_{th}$ due to the velocity spread Δv_L, is $\Delta\theta_{th} \approx 0.5$ mrad from Eqn. (5.4.1), and agrees well with the data in Fig.5.9 (b).

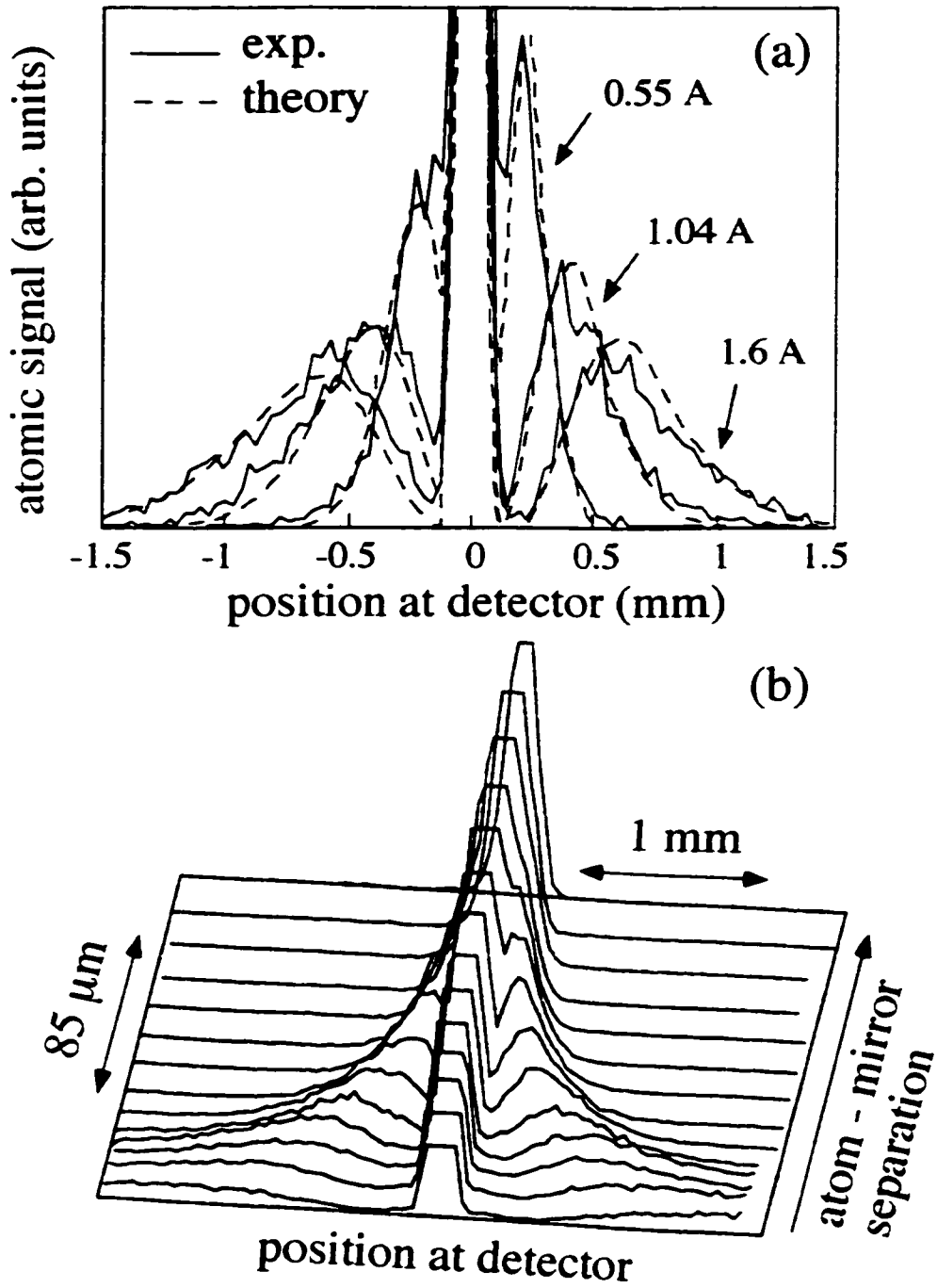

FIG.5.10 (a) Measured (solid lines) and calculated (dashed lines) atomic distributions for mirror currents $I = 0.55$ A, 1.04 A and 1.6 A at a fixed atom-mirror separation $z = 58 \pm 3$ μm. (b) Series of plots of atomic distributions as the atom-mirror separation is increased for fixed $I = 1.38$ A.

(*iv*) The dashed line in Fig. 5.9 (b) is a numerical fit to the data, which assumes an exponentially decaying field[4], and compares well with the measured data. The distribution of deflection angles $\theta(v)$ corresponding to the distribution of atomic velocities v in the He* beam follows from Eqn. (5.4.1). In this numerical calculation, the atom–mirror separation z, defined above, was used as the fit parameter. The fitted value was consistent with experimentally measured z.

Figure 5.9 (c) shows how the angular separation $\Delta\theta$ between the $m_J = 1$ and the $m_J = -1$ peaks as the atom-mirror separation z was increased for fixed current $I = 1.38$ A. Dots are experimental measurements and dashed line is a calculation based on Eqn. (5.4.1). Representative error bar is shown. From Eqn. (5.4.1) it follows that $\Delta\theta \propto e^{-kz}$. This exponential decay is observed in Fig. 5.9 (c).

Figure 5.10 shows another set of deflection data as functions of mirror currents I, and atom-mirror separations z. Figure 5.10 (a) shows the data and corresponding calculations for the angular deflection of the He* beam for three different mirror currents $I = 0.55$ A, $I = 1.04$ A, and $I = 1.6$ A with a fixed atom-mirror separation $z = 58 \pm 3$ μm. As expected, deflection angles θ increase as the mirror current, and correspondingly the magnetic field, was increased. A similar agreement between experiment and simulation has been observed for several other currents and atom-mirror separations.

In Fig. 5.10(b) we show a series of measured angular distributions as the atom-mirror separation is increased at a fixed current $I = 1.38$ A. The deflection angles decrease as the atom-mirror separation is increased, because the He* atoms feel a weaker magnetic field at larger distances away from the mirror. As shown, three peaks are observed only within a narrow range of atom-mirror separation $\Delta z \approx 85$ μm $\approx 3/k$, due to the exponential falloff of the magnetic field away from the mirror. The number of atoms

[4] Joseph Thywissen did the numerical calculation.

in the clipped central $m_J = 0$ peak is comparable to the number of deflected atoms in the $m_J = \pm 1$ peaks, as expected.

Figure 5.10 shows that the angular distributions of the $m_J = 1$ peaks and $m_J = -1$ peaks are not the same. As shown, the angular distributions of the repelled $m_J = 1$ peaks are spatially narrower and taller then the angular distributions of the attracted $m_J = -1$ peaks. This difference can be understood by noting that the interaction potential U is given by $U = 2\mu_B B_o e^{-kz}$ for the repelled $m_J = 1$ state and $U = -2\mu_B B_o e^{-kz}$ for the attracted $m_J = -1$ state. While deflection of the He* beam is caused by the potential gradient $\partial U / \partial z$, focusing of the He* beam is caused by the curvature of the potential $\partial^2 U / \partial^2 z = \pm 2\mu_B B_o k^2 e^{-kz}$. For repelled states, this curvature is positive and they are spatially focused, and for attracted states the curvature is negative and they are spatially defocused. In this way, the micro-electromagnet mirror acts as a weak lens to focus $m_J = 1$ states and defocus $m_J = -1$ states. The focal length of the mirror is $f = 1/(k\theta)$, where $k = 2\pi/a$, and θ is the deflection angle [Johnson K.S. *et al.*, 1998].

The magnetic field above the mirror was calibrated using an added bias field B_{bias}, perpendicular to the direction of the mirror field, $\vec{B}_{bias} = B_{bias}\hat{y}$, spatially uniform and constant in time. The deflection angle θ_{bias} in the presence of the bias field is

$$\theta_{bias} = \theta / \sqrt{1 + (B_{bias} / B_o e^{-kz})^2}, \tag{5.4.2}$$

where θ is the deflection angle for $B_{bias} = 0$. Fitting the measured θ_{bias} / θ as a function of B_{bias} from $B_{bias} = 0$ to $B_{bias} = 6$ mT at z = 114 ± 3 μm, gives the field at the surface of the mirror $B_O / I = 5.3 \pm 0.9$ mT/A, which agrees with simple Biot-Savart calculations of the magnetic field.

5.5 Focusing of the Deflected Atom Beam using Time-Dependent Mirror Currents

Magnetic fields produced by micro-electromagnet mirrors can be rapidly changed using time-dependent currents. In section 5.5, we describe the use of time-dependent mirror currents to narrow the angular distributions of He* atoms shown in Fig.5.10.

As described in section 5.4, the width of deflected peaks in Fig. 5.9 and Fig. 5.10 comes primarily from the spread in longitudinal atomic velocities of the He* beam. The deflection angle θ depends on the atomic velocity v and current I as

$$\theta \propto I/v^2 . \tag{5.5.1}$$

This means that slower atoms, which interact with the mirror for a longer time, receive a larger momentum kick and are deflected at larger angles θ. Narrowing of angular distributions of deflected He* atoms can be achieved by deflecting slow atoms at smaller mirror currents, and fast atoms at larger mirror currents.

Fig. 5.11 (a) shows the timing sequence for the source, mirror and detector pulses used to narrow the angular distributions of deflected He* peaks. The mirror current was either constant $I = 0.86$ A or ramped linearly from $I = 0$ to $I = 1.7$ A at the rate $I/t = 1.17$ A/ms. The atom-mirror separation was $z = 43 \pm 3$ μm.

When the mirror current is ramped we expect to see the narrowing of deflected peaks compared to the constant current case with similar peak separations. This effect is clearly shown in Fig.5.11 (b), where we show the measured angular distributions of deflected He* atoms for constant and ramped mirror current. Solid and dashed lines are data, while circles and squares are calculated values using the same model as described in section 5.4. The calculations agree well with data, as shown in Fig.5.11 (b).

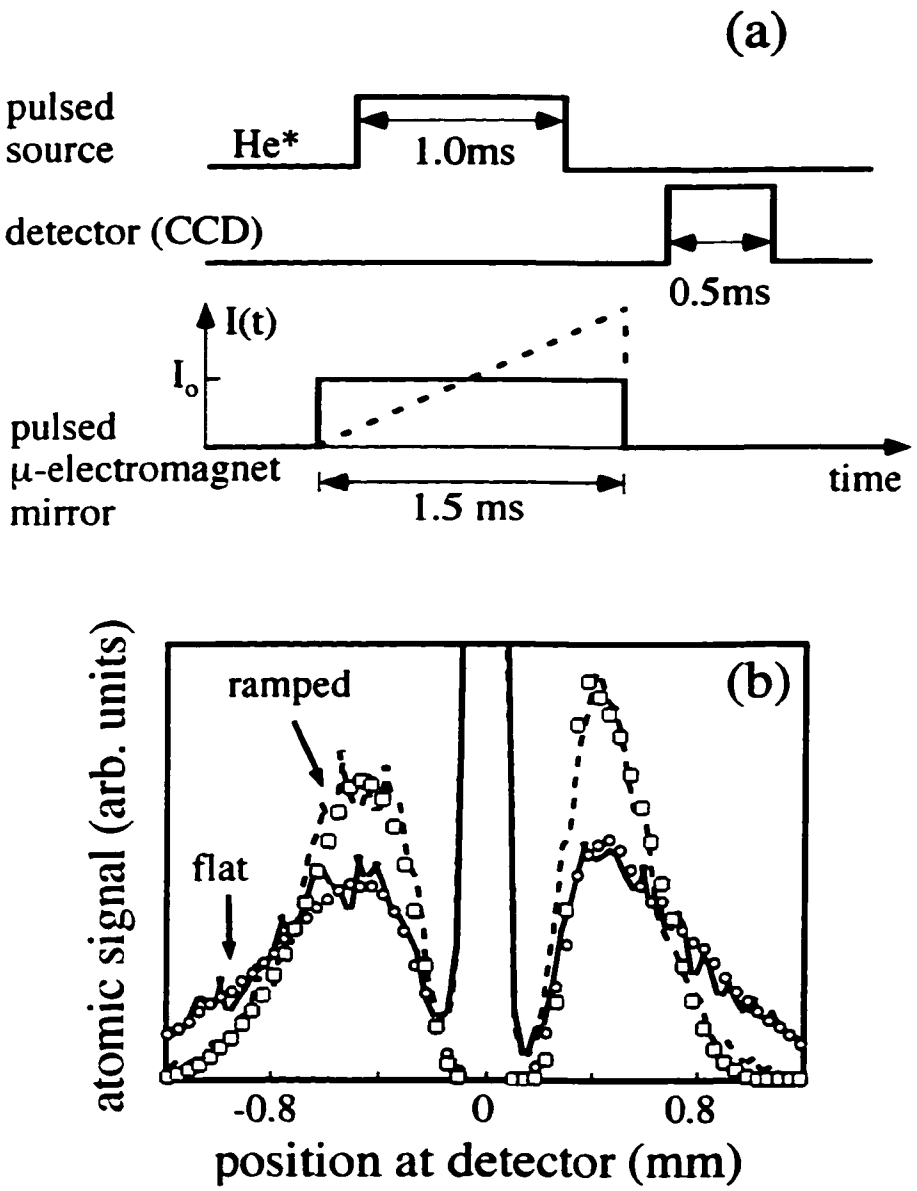

FIG.5.11 (a) The pulsing sequence for the source, the detector and the mirror. The mirror current was either constant I_o (solid line) or ramped linearly (dashed line) from $I = 0$ to $I = 2I_o$. (b) Measured (solid and dashed lines) and calculated (circles and squares) atomic distributions for the constant and ramped mirror current. The mirror current $I_o = 0.86$ A and the atom-mirror separation $z = 43 \pm 3$ μm.

The narrowing of the angular distribution of deflected He* atoms can be understood by noting that detected atoms included slow atoms which passed the mirror first and fast atoms which passed the mirror later. This is because the He* atoms were detected during a narrow time window when the CCD shutter is open. When the mirror current was increased during the current pulse, the slow (fast) atoms interacted with a strong (weak) mirror field and were deflected more (less). Consequently, the deflected peaks were narrowed.

From Eqn. (5.5.1) we see that deflection angles θ can be approximately velocity-independent if the mirror current $I(t)$ during the current pulse is $I(t) \propto \langle v^2(t) \rangle$, where $\langle v^2(t) \rangle$ is the mean of the square of atomic velocities v reaching the mirror at time t. We chose a linear ramp for the micro-electromagnet mirror current because this ramp almost perfectly matched $\langle v^2(t) \rangle$ for our timing sequence. The starting time and the slope of the ramped current pulse were experimentally adjusted to narrow the angular distributions for peak separations similar to those obtained with constant current.

In summary, we have demonstrated that micro-electromagnet mirrors can be used successfully to deflect fast He* atoms at mrad angles. In order to achieve this goal, we have integrated micro-electromagnet mirrors inside an existing He* beam apparatus built by [Lawall J., 1993]. We have designed and built an additional low-temperature setup to cool the mirrors and to orient them with respect to the He* atom beam. The micro-electromagnet mirrors were carefully aligned with respect to the He* beam, so that the mirror wires were parallel to the direction of the He* beam to ensure adiabaticity. After interacting with the magnetic field of the micro-electromagnet mirror, the He* atom beam was split into three peaks, corresponding to magnetic quantum numbers $m_J = \pm 1$ and $m_J = 0$ of the metastable He* atom states. We have measured the spatial distributions of deflected atoms as functions of atom-mirror separation and mirror current, to show that deflection angles decrease as the mirror current is decreased and as the atom-mirror

separation is increased. The data agrees well with a simple model of an exponentially decaying magnetic field of the mirror. The magnitude of the magnetic field of the mirror was calibrated by deflecting atoms in the presence of an added external bias field. Finally, we have exploited time-dependent capabilities of micro-electromagnet mirrors to narrow the deflected peak distributions. This experiment illustrates the advantage of micro-electromagnet mirrors over permanent-magnet structures to dynamically manipulate atoms.

Chapter 6

REFLECTION OF COLD Rb ATOMS

In this Chapter we describe the properties of liquid nitrogen cooled micro-electromagnet mirrors to reflect a cloud of free-falling laser-cooled ^{85}Rb atoms at normal incidence. The mirrors consisted of microfabricated current-carrying Au wires in a periodic serpentine pattern on a sapphire substrate. We imaged the fluorescence from the reflected cloud, dropped from a magneto-optical trap, and measured its size as a function of mirror current. The influence of the finite size of the mirror on its reflective properties was studied. The experiment confirms the nontrivial dependence of mirror corrugations on mirror current and on whether the mirror has an even or odd number of wires [see Chapter 3]: the measured corrugations reach a local minimum at an optimal current, rather than decreasing monotonically as current increases, and mirrors with an odd N number of wires are smoother than mirrors with even N. The measured mirror corrugation of ~ 10 mrad was achieved. Ultimately, micro-electromagnet mirrors promise an impressive 'flatness' for several reasons: 1) microfabrication can produce precisely controlled wire shapes and geometries on substrates with excellent surface smoothness, 2) the detrimental effect of possible wire irregularities on magnetic field equipotentials is suppressed by electrical current conservation, and 3) the strength of mirrors can be adjusted by applying time-dependent currents.

6.1 Experimental Setup

Figure 6.1 shows a photograph (Fig.6.1 (a)) of a micro-electromagnet atom mirror used in this experiment, consisting of a serpentine pattern of current-carrying Au wires on a sapphire substrate, together with a schematic diagram of the wire pattern (Fig. 6.1 (b)) and a profilometer trace of the wire profile (Fig. 6.1 (c)). The mirrors used in this experiment permitted high current densities up to ~ 10^8 A/cm^2 and magnetic fields to B ~ 0.1T with gradients $|\nabla B|$ ~ 100 T/cm.

Unless otherwise noted, the mirror specifications in the present experiment are: active area 1 x 1 cm^2 of the serpentine pattern of Au wires, period a = 200 μm, N = 101 lines, resistance R = 40 Ω at room temperature, and R = 10 Ω at 77 K. The mirrors were fabricated on circular sapphire substrates with thickness d = 0.5 mm and radius r = 1.25 cm, and surface roughness (peak to valley) measured with an atomic-force microscope of ≈ 20 nm. Two additional wire segments with the same profile and spacing, with resistance 0.4 Ω at room temperature, were added to the original mirror, as shown in Fig.6.1 (b). With these additional wires we were able to: (*i*) increase the number of wires from odd to even during the experiment, and (*ii*) use them as 'compensating wires' to mimic an ideal infinitely large mirror. Figure 6.1(c) shows a profilometer trace of a duplicate mirror with the same process parameters and resistance as the one used in the experiment, with the wire width w ≈ 70 μm and height h ≈ 7 μm indicated. To avoid damaging the mirror, we have applied currents only up to 3 A at liquid nitrogen temperatures, which corresponds to fields up to ≈ 30 mT at the surface of the wires.

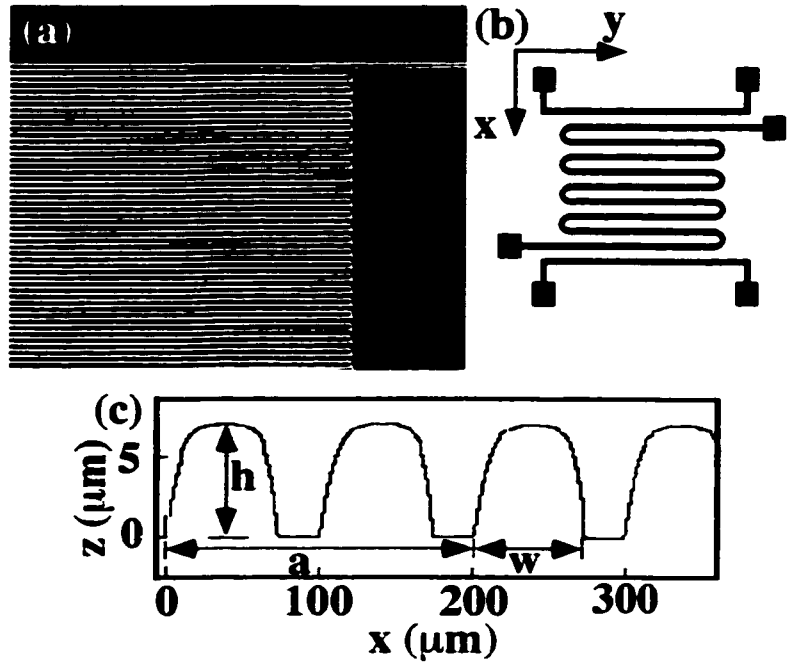

FIG. 6.1 Serpentine micro-electromagnet Au mirror on sapphire substrate (a) micrograph, (b) mirror pattern, (c) profilometer scan of a mirror with the same parameters as the one used in the experiment; wire width $w \approx 70$ μm and height $h \approx 7$ μm

The experimental setup used to reflect cold atoms from micro-electromagnet mirrors is schematically illustrated in Figs. 6.2(a) and 6.2(b). A cloud of cold ^{85}Rb atoms in the $5^2S_{1/2}$ $F = 3$ electronic ground state is accumulated and cooled in a magneto-optical trap (MOT). This atomic setup was the same as in [Landragin A. *et al.*, 1996], previously used to reflect atoms using light-based atom mirror and measure the mirror roughness. The number of trapped atoms is ~ 3 x 10^7 in a volume ~ 0.5 mm^3 with root-mean-square atom velocity $v_{rms} \approx 36$ mm/s, corresponding to temperature $T \approx 7$ μK. The atom cloud is released from the MOT with center at a constant height $H = 19.6$ mm above the mirror, and optically pumped during the fall into the $|F = 3, m_F = 3>$ state. A 1.06 mm wide slit mounted ≈ 3 mm above the mirror defines the width of the atom cloud which reaches the center of the mirror.

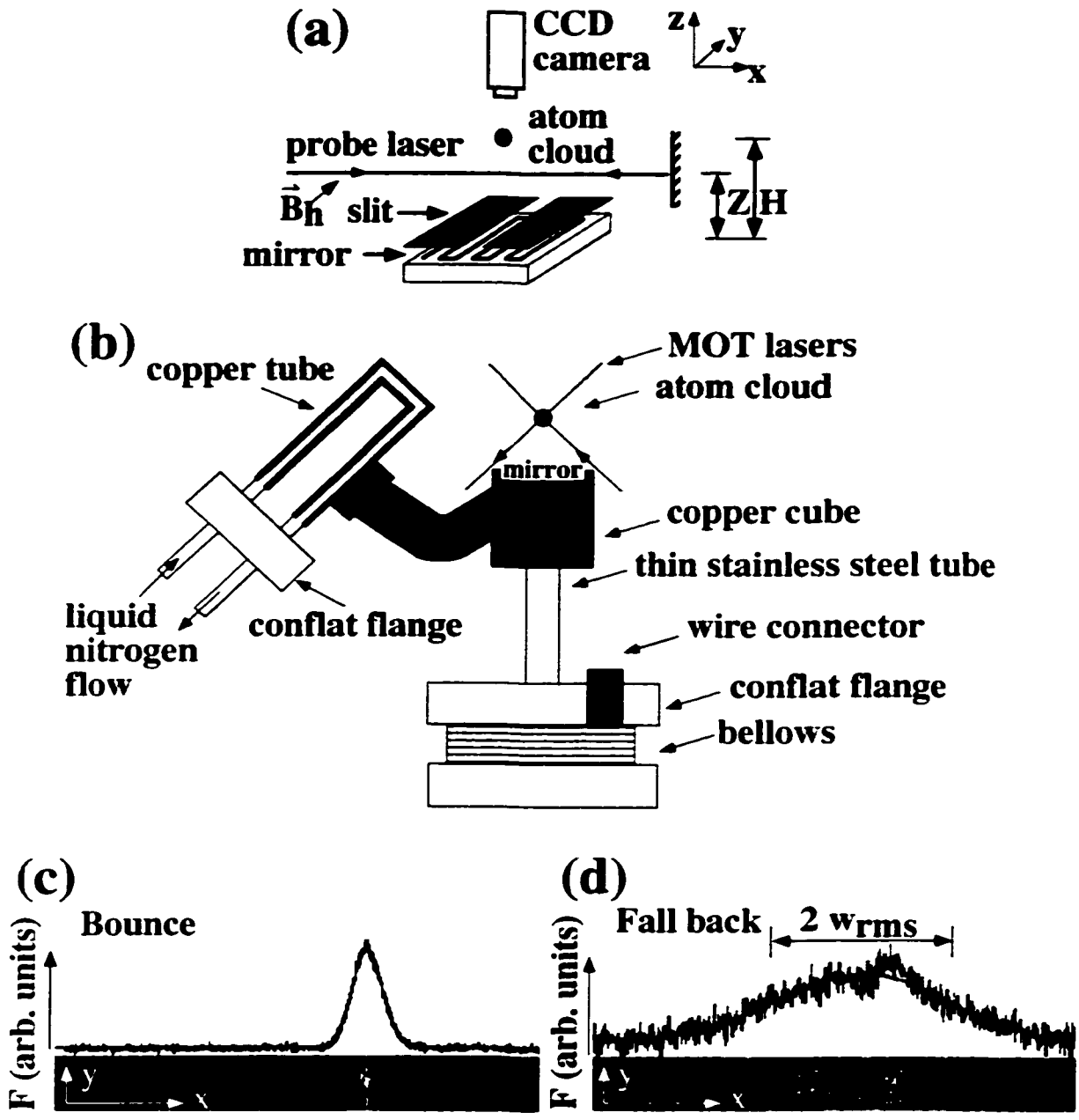

FIG. 6.2 (a) and (b) Experimental setup in the Institute of Optics, Orsay, France, used to reflect cold Rb atoms from a micro-electromagnet mirror; $H = 19.6$ mm and $Z = 9.4$ mm. Fluorescence profiles F along the x-direction and atom cloud images are shown at height Z (c) after the first bounce and (d) during the fall before the second bounce. The solid lines are Gaussian fits.

The mirror is mounted on a copper cold finger and cooled by continuously flowing liquid nitrogen to lower the mirror resistance and increase the thermal conductivity of the mirror and the sapphire substrate. The cold finger is supported with a ≈ 0.5 mm thin and ≈ 12 cm long stainless steel tube welded to a 2 3/4" conflat flange attached to a rotation stage using a bellows (see Fig. 6.2(b)). This allowed positioning of the mirror with respect to the atom cloud. The mirror mount consisted of an oxygen free high purity copper cube (OFHC) with sides ≈ 2.5 cm, silver soldered to a flexible ≈ 8 cm long and ≈1.3 cm thick copper braid. The braid was further attached to a copper tube and a conflat flange with feedthroughs where liquid nitrogen is circulated from a large storage dewar. The temperature of the mirror was estimated to be ~ 100 K from the known temperature dependence of the mirror resistance. Rectangular current pulses with amplitudes I and duration 5 ms coinciding with the arrival of the atom cloud were applied to the mirror every 1.5 s. We used a Kepco power supply with 100V and 4A with added circuit protection against large current spikes that could damage the mirror. The pulsed mode operation together with cryogenic cooling of the mirror reduced the average heat dissipation and allowed for higher currents and field strengths. To ensure that atoms adiabatically follow the magnetic field direction, i.e. remain in the $m_F = 3$ state, a constant holding field B_h = 10 μT was applied along the y-direction parallel to the mirror lines and perpendicular to the mirror field (see Fig. 6.2(a)).

The width of the atom cloud was measured by a horizontal probe laser beam during the free fall after the first bounce, and during the fall back before the second bounce. The probe laser beam was positioned at height Z = 9.4 mm above the mirror (see Fig. 6.2 (a)). The spatial extent of the probe beam was 1.4 mm in the z-direction by 1.0 cm in the y-direction, its power density was 1.1 mW/cm^2, and it was detuned 5 MHz from the Rb fluorescence line. The fluorescence was imaged by a charge-coupled device (CCD) camera looking down at the mirror along the z-direction [Landragin A. *et al.*,

1996]. The stray-light background recorded by the camera was subtracted from the fluorescence signal.

6.2 Atom Reflection

In this section we show the experimental results confirming the reflection of an atom cloud from micro-electromagnet mirrors. This reflection was observed by imaging the atoms bouncing off the mirror. Figures 6.2(c) and 6.2(d) show typical fluorescence images of the atom cloud together with fluorescence profiles along the x-direction after the bounce (Fig. 6.2(c)) and as the atom cloud falls back (Fig. 6.2(d)) before the second bounce on the mirror. The profiles empirically fit Gaussian distributions $F(x) \propto e^{-(x-x_o)^2/2w_{rms}^2}$. From fits to measured profiles such as those in Fig. 6.2 we obtain the root-mean-square width w_{rms} of the cloud at height $Z = 9.4$ mm above the mirror. Had the atoms been reflected specularly by an ideally smooth infinite mirror, the intrinsic width w_o would then be determined by the initial momentum and spatial distribution of the atoms in the cloud, the drop height, the slit width, and the effect of the probe laser; Monte-Carlo simulations of a specular reflection give $w_o = 2.54$ mm[1]. The actual measured widths of the atomic cloud w_{rms} are larger than w_o because the actual mirror, finite in size, is not ideally smooth. We have used the fitted width of the atomic cloud to study the reflective mirror properties as a function of current and to compare mirrors with odd and even numbers of wires.

---

[1] The rms width w_o for a perfectly specular bounce is $w_o = \left(w_{thermal}^2 + w_{probe}^2\right)^{1/2}$ where $w_{thermal} = 2.28mm$ is thermal expansion and $w_{probe} = 1.12mm$ is probe laser heating.

6.3 Measurements of the Mirror Specularity

Figure 6.3 shows the experimental width w_{rms} of the reflected atomic clouds falling back under gravity toward the mirror as a function of mirror current I for mirrors with $N = 101$ and $N = 102$ wires. The number of wires was changed during measurements by energizing one additional wire segment shown in Fig. 6.1(b).

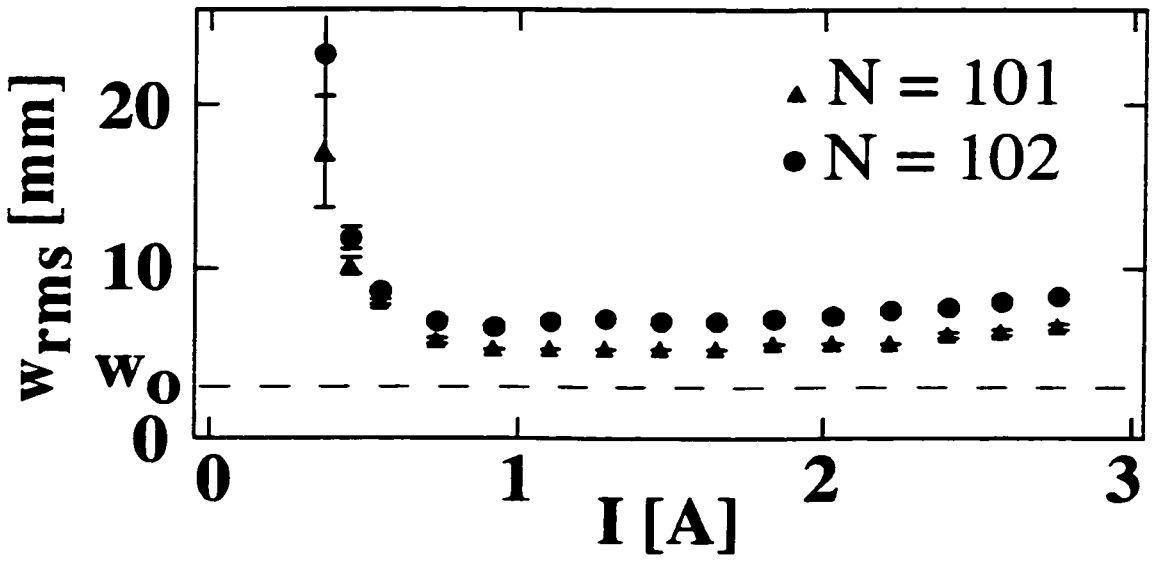

FIG. 6.3 Root-mean-square widths w_{rms} of the Rb cloud as it falls after the first bounce vs. mirror current I for mirrors with even (●, $N = 102$) and odd (▲, $N = 101$) numbers of wires. The computed width w_o for a perfectly specular bounce is the dashed line.

As predicted theoretically, the data of Fig. 6.3 clearly show three mirror properties: (i) a threshold current I_{th} for atom reflection, (ii) an optimal current I_{opt} at which the width of the reflected cloud is minimized, and (iii) a pronounced increase in width for the mirror with an even number of wires.

(i) Reflection is only observed at mirror currents above the threshold $I_{th} \cong 0.35$ A, as shown in Fig. 6.3. As the current increases, the magnetic field increases, and the height of the turning point for the atom bounce increases. The threshold occurs when atoms no longer hit the wires or substrate. The minimum magnetic field required to reflect ^{85}Rb atoms in the $m_F = 3$ ground state dropped from H = 19.6 mm is calculated from the incident atomic energy to be $B_{th} \cong 3$ mT at the turning point. This value agrees well with a threshold estimated from the computed magnetic field 2.9 mT for I_{th} at the top of 70 x 7 μm^2 rectangular wires using simple Biot-Savart calculations. Close to threshold the measured width w_{rms} of the reflected cloud is comparable for odd and even mirrors, consistent with the fact that the magnetic field contours for even and odd mirrors shown in Figs. 3.4(a) and 3.4(b), in Chapter 3, are comparable near the wires.

(ii) In contrast to the simpler infinite mirror case, the transverse width w_{rms} of the atom cloud is minimized at an optimal mirror current. For even $N = 102$ the optimal current is $I_{opt} \sim 1$ A and for odd $N = 101$ it is $I_{opt} \sim 1.5$ A, as shown in Fig. 6.3. From Fig. 3.4 we can understand that the mirror will be least corrugated when the current is approximately adjusted to give a turning point in the smoothest magnetic field contour region, and that the mirror with even N will have a lower optimal current than the mirror with odd N. The estimated height of the turning point above the top of the wires is $z_{turn} \approx 1/k \ln(B_o / B_{th})$ (Eqn. 3.1.1), where B_o is the surface field (Eqn. 2.3.3); for even $N = 102$, we find $z_{turn} \approx 40$ μm for $I_{opt} = 1$ A and for odd $N = 101$ we find $z_{turn} \approx 50$ μm for $I_{opt} = 1.5$ A. The increase in measured width w_{rms} above the width w_o for perfect specular reflection provides an upper bound to the angular spread: $\Delta\theta_{max} = \left(w_{rms}^2 - w_o^2\right)^{1/2} / 2v_z t$, where v_z is the average vertical speed and t is the time interval; we estimate $\Delta\theta_{max} \approx 16$ mrad for $N = 101$ at $I \sim I_{opt}$. This upper bound to the angular spread is comparable to calculations of the rms angular spread $\Delta\theta_{rms} \sim 10$ mrad for finite sized micro-electromagnet mirrors with $N = 101$ wires at optimum current. In previous experiments the reported angular spread was 5 mrad for evanescent wave mirrors [Landragin A. *et al.*,

1996], 6 mrad for permanent magnet mirrors [Hughes I.G. *et al.*, 1997; Saba C.V. *et al.*, 1999], and 45 mrad for electromagnet mirrors [Lau D.C. *et al.*, 1999].

(iii) Figure 6.3 compares reflected atom cloud widths at various currents from mirrors with even $N = 102$ and odd $N = 101$ numbers of wires. The only difference between the two mirror configurations came from energizing one of the additional wires at the end. We observe a clear difference in specularity between the two mirrors, the specularity being higher for odd $N = 101$. From Fig. 3.4 (Chapter 3) we can see that odd N mirrors have a larger region of more nearly straight equipotentials than even N mirrors and thus are expected to be smoother.

Reflection of atoms was also observed from a smaller mirror with active area 2 x 2 mm^2 of the serpentine pattern, $N = 83$, $a = 48$ μm, $w \approx 20$ μm, and $h \approx 3$ μm. The mirror resistance was $R = 60\ \Omega$ at room temperature and $R = 20\ \Omega$ at $T \sim 100$ K. For this small mirror the measured threshold current $I_{th} \approx 90$ mA is smaller than that for the large mirror due to the stronger fields produced near wires with smaller cross sectional area and spacing. The threshold estimated from the computed magnetic field 2.6 mT for I_{th} at the top of 20 x 3 μm^2 rectangular wires using the Biot-Savart law agrees well with the threshold computed from the atom energy and with the threshold observed for the larger mirror. The measured optimum current was $I_{opt} \approx 600$ mA, although reflection from this small mirror is difficult to analyze in more detail because the atom cloud was comparable in size to the mirror.

6.4 Minimization of the Mirror Corrugations

In this section, we show the reflection results when the two added wires along the edges (Fig. 6.1(b)) were used to compensate for the detrimental effect of the finite number of wires. Figure 6.4 shows a schematic diagram of the same wire pattern as in

Fig. 6.1(b) with the current directions and magnitudes as indicated. The current in the mirror is *I*, while the current in the end segments is *I/2*. As discussed in Chapter 3, the purpose of the added wires to mimic the field of an ideal infinitely large mirror. For an infinitely large mirror, the mirror specularity increases as a function of distance from the wires.

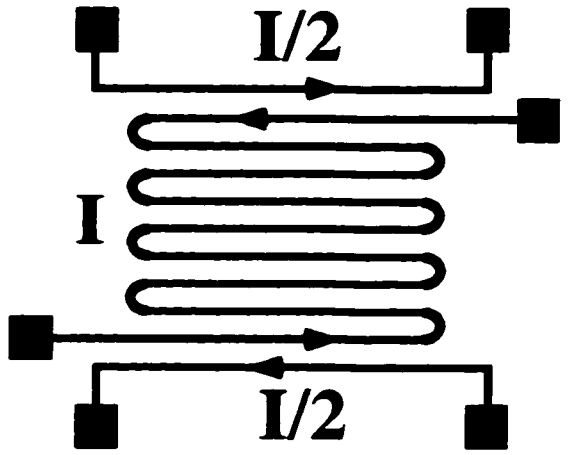

FIG.6.4 Wire pattern of the 'compensated mirror' with an odd number of wires. The current directions and magnitudes are indicated. The two added wires along the mirror edges compensate for the detrimental effect of the finite number of wires.

Figure 6.5 shows the measured angular deviation $\Delta\theta_{max}$ for a mirror with the compensating wires energized (N = 103), together with the data for the uncompensated mirror with N= 101 (see section 6.3). Because the purpose of the added wires in the

compensated mirror is to mimic the field of an ideal infinitely large mirror, we expect to observe the angular deviation $\Delta\theta_{max}$ decreasing as a function of current. This behavior for a compensated mirror is shown in Fig.6.6. The minimum mirror corrugation measured in this way is $\Delta\theta_{max}$ = 13 mrad for I = 2.8 A (Fig.6.5). In contrast, the minimum mirror corrugation for the uncompensated mirror is obtained at an optimal current I_{opt} ~ 1.5 A, as described in section 6.3.

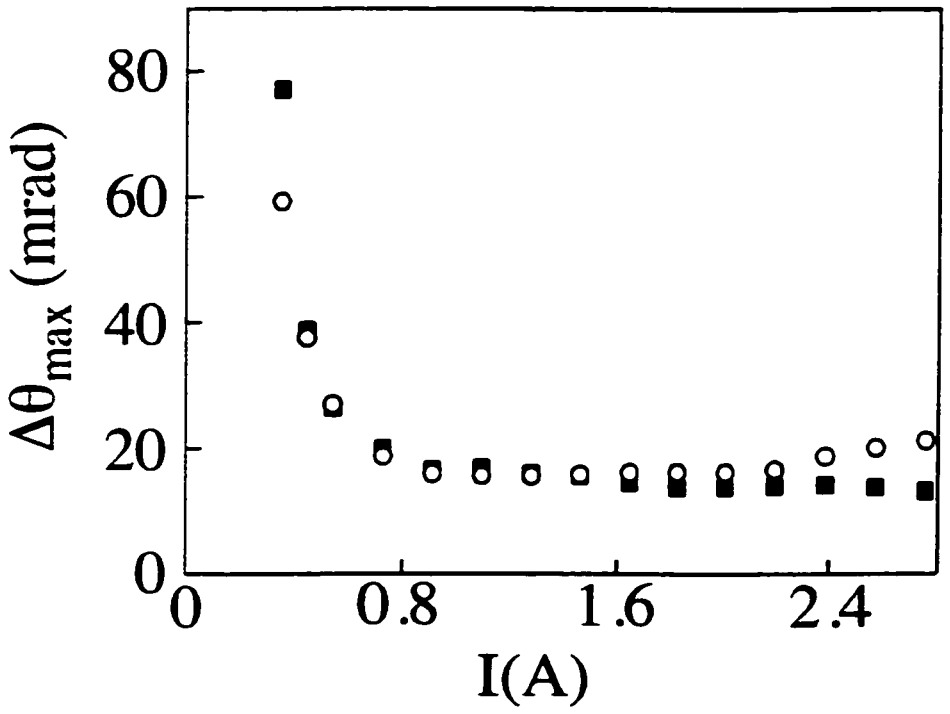

FIG. 6.5 Angular deviation $\Delta\theta_{max}$ from specular reflection as a function of mirror current I for a mirror with compensating wires (■) shown in Fig. 6.5 (N = 103), together with the data for uncompensated mirrors (○) with N= 101. Every point is a result of 20 averages.

The mirror in Fig. 6.1 was also used to reflect unpolarized Rb atoms in all the positive magnetic sublevels $m_F = 3$, $m_F = 2$ $m_F = 1$, and $m_F = 0$ [Cognet L. *et al.*,1999]. The $m_F = 0$ state was reflected due to the quadratic Zeeman term in the potential (Eqn. 2.1.3). The number of reflected atoms as a function of the mirror current formed a series of steps corresponding to the thresholds I_{th} for different m_F states given by $m_F\, g_F\, I_{th} \approx E/(\mu_B \alpha)$ = constant, where $E = mgH$ is the atomic energy (m is the Rb atom mass, H is the initial height above the mirror), and $\alpha = B_o/I$ is defined in Eqn. (2.3.3). The steepness of these steps depends on the magnetic field configuration close to the mirror surface and is related to the shape of the wires. More studies are needed to understand the details. The mirror corrugations were also studied as a function of the background magnetic field [L. Cognet *et al.*, 1999].

In conclusion, we have 1) reflected cold atoms from micro-electromagnet mirrors with odd and even numbers of wires, 2) demonstrated the existence of finite currents which optimize the reflective mirror properties, 3) shown that mirrors with an odd number of wires are smoother than mirrors with an even number of wires and 4) shown how to reduce the mirror roughness by adding compensating wires along the edges of mirrors with an odd number of wires to mimic the field of an ideal infinite mirror. Improvements of reflective properties might be possible by tailoring the wire shape and geometry, and by exploiting time-dependent currents, as described in Chapter 5. It is important to note that presently attainable currents are already sufficient to exceed the current required for minimum roughness as shown in Fig. 6.3, and that larger currents are not necessary.

Chapter 7

THREE-DIMENSIONAL (3D) MICRO-ELECTROMAGNET TRAPS FOR NEUTRAL PARTICLES WITH SPIN

In this Chapter, we describe three-dimensional (3D) micro-electromagnets developed to control particle motion in electromagnetic field landscapes in vacuum near a chip. Three-dimensional micro-electromagnets consist of multiple layers of micron-scale conductors separated by transparent insulators to create particle containers with deep, symmetric and time-dependent potentials, suitable for integration in quantum circuits. In section 7.1, we describe 3D traps, integrated 3D traps with a mirror, and 3D guides for neutral particles with spin. Traps can be used to study quantum systems of one or many particles. Possible applications extend to nuclear magnetic resonance and biological systems.

In section 7.2 we show that stronger traps and guides are formed by 3D micro-electromagnets than 2D micro-electromagnets of comparable size and power dissipation. In section 7.3 we describe a method to fabricate three-dimensional micro-electromagnets based on multiple-step optical lithography. Using modern fabrication techniques, three-dimensional micro-electromagnets can be precisely designed and constructed. A transparent polymer that can be optically patterned is used to insulate the metal wires and create micro-cavities for particle motion. Finally, in section 7.4 we describe how two three-dimensional traps could be integrated into a double trap with an adjustable trap coupling.

7.1 Introduction

Three-dimensional structures are interesting for the field of particle manipulation because they can create stronger confinement potentials, and higher gradients and curvatures of the potential than planar structures. Three-dimensional traps and guides can confine particles more tightly than planar traps and guides. Particle confinement in planar structures is typically weakest perpendicular to the plane [Weinstein J.D. and Libbrecht K.G., 1995]. This can be seen in Figs. 2.4 and 2.5 in Chapter 2, for the magnetic field configurations produced by planar micro-electromagnet traps and guides. In contrast, particle confinement in three-dimensional structures can be several times stronger, as will be discussed in section 7.2. The condition for quantum behavior of particles inside the traps $\Delta E > k_B T$, with ΔE the energy level separation in the traps and $k_B T$ the thermal smearing of the energy levels, is easier to realize for three-dimensional traps. Finally, three-dimensional structures can create spatially-symmetric trapping potentials, which is more difficult to accomplish with planar structures.

In the rest of this section we describe several three-dimensional micro-electromagnets for neutral particle manipulation. Figure 7.1 shows schematic diagrams, magnetic field profiles, and micrographs of three 3D micro-electromagnets for neutral atoms. Figure 7.1(a) shows a quadrupole microtrap consisting of two stacked current loops with a circular hole through the trap center. This is a miniature anti-Helmholtz configuration trap [see for review Phillips W.D., 1998]. Figure 7.1(b) shows a 3D atom guide consisting of two stacked pairs of parallel conductors. Figure 7.1(c) presents a 3D trap with an additional pair of rings to create the bias magnetic field, placed on top of a micro-electromagnet mirror, which can help load the trap as described below.

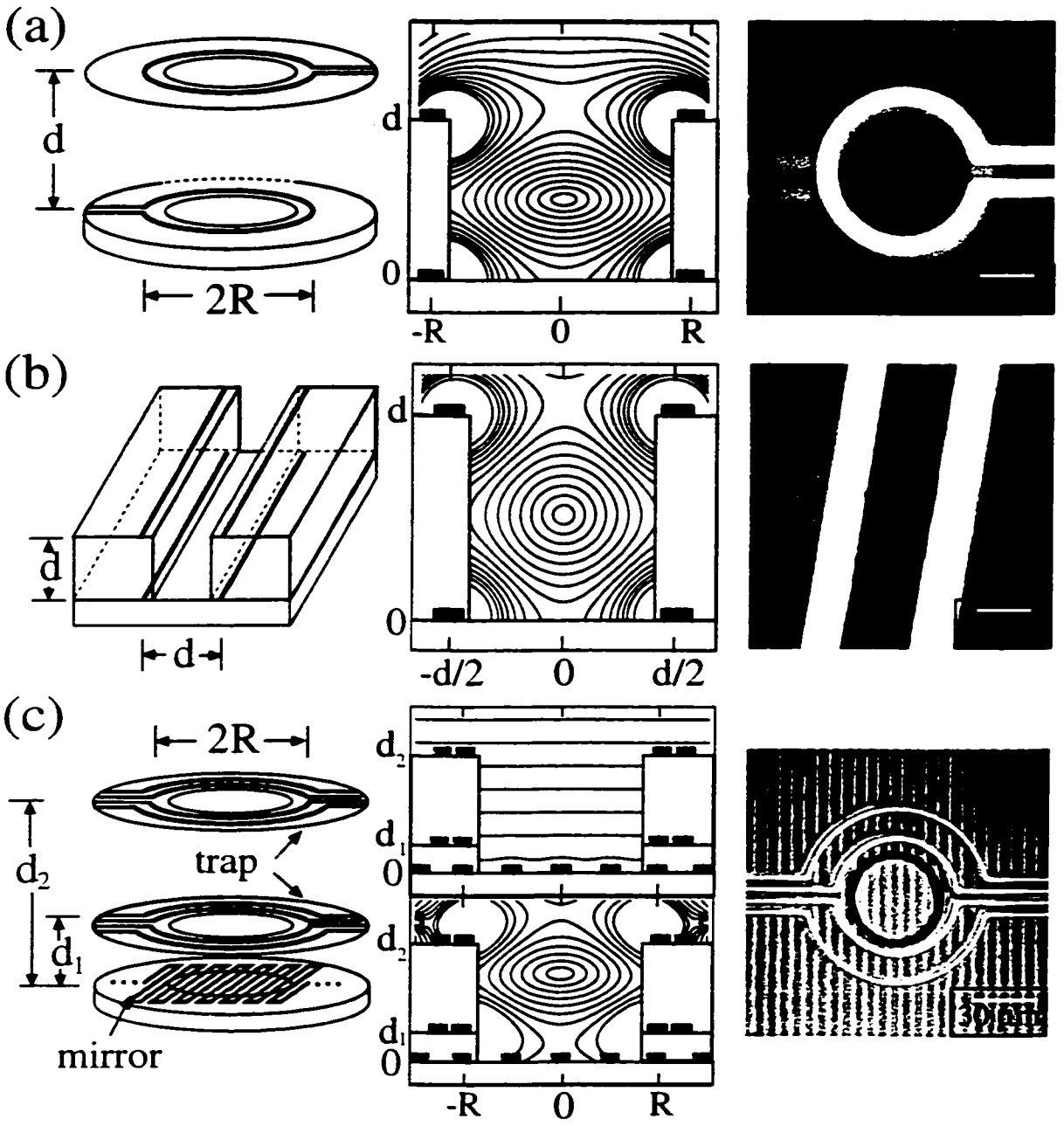

FIG. 7.1 Three-dimensional micro-electromagnet schematic diagrams, contours of constant magnetic field magnitude B about the trap or guide center, and device photographs for (a) trap with two rings of radii R and separation d, with opposite currents I, (b) guide with four conductors, (c) trap with bias field coils above a mirror, $d_1 = 0.25R$, $d_2 = 1.5R$; upper contour plot for trap off, mirror on, lower contour plot for trap on, mirror off. Magnetic field contours are spaced by (a) $\Delta B = (0.03\mu m/A)\, I/R$ (T); (b) $\Delta B = (0.05\mu m/A)\, I/R$ (T) and (c) (above) $B_{n+1}/B_n = 0.8$ where n = 1 to 20, (below) by $\Delta B = (0.03\ \mu m/A)\, I/R$ (T), where I is given in A, and R in μm.

Magnetic field profiles which determine the particle potential are shown for three structures in Fig. 7.1. As introduced in Chapter 2, the potential energy is $U = g_F m_F \mu_B B$, with magnetic field magnitude B, Bohr magneton μ_B, Landé g-factor g_F, and magnetic quantum number m_F, which remains constant for the adiabatic case where particle motion is slow enough to prevent spin flip. Weak-field seeking particles ($m_F g_F > 0$) are attracted to B-field minima.

Figure 7.1 (a) shows magnetic field contours for a 3D trap with two conductor loops of radius R and a distance d apart. The trap depth B_{max} = (0.5μm/A) I/R (T) is greatest for d =1.25R, corresponding to maximum particle temperature $T_{max} = \mu_B B_{max}/k_B$ = (0.3μm/A) I/R (K) for a particle magnetic moment $\mu = \mu_B$; the current I is expressed in A, and the radius R in μm. The field gradient and curvature scale as I/R^2 and I/R^3 respectively. Figure 7.1 (b) shows field contours for a guide with four conductors a distance d apart. The guide depth is B_{max} = (0.64μm/A) I/d (T) corresponding to T_{max}= (0.4μm/A) I/d (K) for $\mu = \mu_B$; I is expressed in A, and the size d in μm.

The magnetic fields from micro-electromagnets can be changed very rapidly, creating new possibilities for particle manipulation. Figure 7.1 (c) illustrates a time dependent micro-electromagnet structure consisting of a 3D micro-electromagnet trap, with an additional pair of coils to produce a bias magnetic field, placed on top of a micro-electromagnet mirror. By modulating the mirror current, this structure can cool atoms and load them into the trap. Adiabatic compression of atoms into small volumes increases their temperature because the magnetic potential is conservative. However, a receding mirror can cool atoms before loading into a trap. A ball bouncing elastically from a hard wall moving away will stop when the wall velocity is $v/2$, where v is the incoming ball velocity. For a micro-electromagnet mirror this velocity is achieved by decreasing the mirror current exponentially $I(t) = I_o e^{-\pi t/a}$, where $a/2$ is the distance between mirror wires. The time required to cool is ~ 70 μs for a mirror with a = 200 μm (see Chapter 6) and initial atom velocity v = 1 m/s for atoms dropped from a larger

magneto-optical trap above. The mirror current can be modulated in other ways at high speed to manipulate trapped atoms, including periodic kicks to study the nonlinear dynamics of atom motion [Saif F. *et al.*, 1998].

Three-dimensional micro-electromagets can be used for other applications. Coils like those in Fig. 7.1 (a) could be used in nuclear magnetic resonance experiments [Olson D.L. *et al.*, 1995] at large field gradients ~ 10^4 T/m. Arrays of 3D micro-electromagnets could arrange small biological organisms whose population and characteristics depend on the local magnetic field. Three-dimensional micro-electromagnets with voltage electrodes could be used for trapping and guiding of ions and electrons using Paul [Brewer R.G. *et al.*, 1992] and Penning [Brown L.S. and Gabrielse G., 1986] manipulation techniques, and polar molecules using electric-dipole interactions [Wark S. J. and G. I.Opat, 1992; Sekatskii S.K. and Schmiedmayer J., 1996]. Mirrors for polar molecules formed from interdigitated electrodes have been realized based on the linear Stark effect [Wark S. J. and G. I. Opat, 1992]. The interaction potential $U = -\vec{d} \cdot \vec{E}$, where $\vec{d}$ is the electric dipole moment and $\vec{E}$ is the electric field, is formally the same as in the case of magnetic mirrors for neutral particles.

7.2 Comparison with Planar Micro-Electromagnets

Stronger traps and guides are formed by 3D micro-electromagnets than by 2D micro-electromagnets of comparable size and power dissipation. Table 1 compares 3D and 2D traps and guides for cold Cs atoms, showing trap depth T_{max}, field gradients $\partial B/\partial z$ and $\partial B/\partial r$, and energy level spacings $\hbar\omega_z$ and $\hbar\omega_r$. The 3D traps and guides are shown in Fig.7.1. For 2D traps (Fig.2.4), two coaxial loops of radii R_1 and R_2 carry currents I_1 and I_2. The trap depth is maximum for $I_2/I_1 = 1.87$ and $R_2/R_1 = 2.66$ [Weinstein J.D. and Libbrecht K.G., 1995]. For 2D guides (Fig.2.5), four parallel wires separated by distance d carry currents I_1 in the inner pair and I_2 in the outer pair, optimized for

maximum depth ($I_2/I_1 = 2.1$). The power dissipation and size of 3D and 2D cases are the same ($R = R_1$). The field gradients are calculated for dimensions $R = d = 1$ μm, current $I = 0.1$ A and magnetic moment $\mu = \mu_B$. A bias field $B_{bias} = 1\ mT$ in the z direction ensures adiabaticity. Three-dimensional micro-electromagnets are favored over 2D micro-electromagnets for superconducting wires, because the critical current density ~ 10^7 A/cm^2 [*Materials at Low Temperatures* (eds. Reed R.P. and Clark A.F.), 1983] and magnetic field are lower than those achievable in gold.

TAB 7.1

	T_{max} (mK)	$\partial B/\partial z$ (10^4 T/m)	$\hbar\omega_z$ (10 μK)	$\partial B/\partial r$ (10^4 T/m)	$\hbar\omega_r$ (10 μK)
3D trap	30	10	16	5	8
2D trap	4.5	3	5	1	1.6
3D guide	40	15	23	15	23
2D guide	8	4	6	4	6

TAB.7.1 Trapping parameters for 3D and 2D micro-electromagnets. In the presence of a bias field B_{bias} in the z-direction to ensure adiabaticity, the frequencies in the z - and ρ-direction are $\omega_z = [(\mu(\partial B/\partial z)^2)/(m\ B_{bias})]^{1/2}$ and $\omega_r = [(\mu(\partial B/\partial r)^2)/(m\ B_{bias})]^{1/2}$. The field gradients $\partial B/\partial z$ in the z-direction and $\partial B/\partial r$ in the radial direction are calculated for $R = d = 1$ μm, for $I = 0.1$ A and $\mu = \mu_B$. The energy level separation $\hbar\omega_z$ and $\hbar\omega_r$ between the lowest-lying levels is calculated for Cs at $B_{bias} = 1$ mT.

7.3 3D Micro-Electromagnet Fabrication and Properties

In section 7.3, we describe the fabrication and testing of three-dimensional micro-electromagnets. Micrographs of fabricated 3D micro-electromagnets are shown in the right column of Fig. 7.1. Each structure consists of layers of metal conductors separated by transparent insulators, with cavities to permit atom motion. Devices were fabricated on sapphire plates using multiple steps of thin film deposition and optical lithography. The feature size can be as small as 150 nm. The transparent insulator films were spun-on polyimide (an organic polymer with magnetic permeability $\mu_r = 1$ and dielectric constant $\varepsilon_r = 3.3$) and the metal films were made using evaporated gold. The structures allow optical access to atoms through the transparent substrate and insulator layers, permitting detection, imaging, and laser manipulation of atoms and molecules. The fabrication method can integrate devices both horizontally along the chip and vertically to make circuits for particle motion. These circuits avoid atom heating by lasers, used for the optical manipulation of atoms [see for review Phillips W.D., 1998].

Polyimides are ideally suited to make insulators to separate layers of metal conductors. Polyimide layers are easily patterned, resistant to chemicals, and thermally stable to above 500 °C. Their thermal coefficient of expansion matches that of metals, and they provide an excellent planarization of the underlying surface. The magnetic permeability of polyimides $\mu_r = 1$, but it can be changed by incorporating inert magnetic fillers, such as iron compounds. Other specified properties of polyimides are[1]: thermal conductivity ~ 4×10^{-5} cal/(cm s °C), specific heat 0.6 cal/(g °C), electrical resistivity $>10^{16}$ Ωcm, dielectric breakdown field $> 2 \times 10^4$ V/cm and refractive index 1.7.

Different molecular compositions of polyimide are commercially available[1]. All polyimides can be patterned and thinned using wet and dry etches, while photosensitive

[1] Available from HD MicroSystems (enterprise of Dupont Electronics and Hitachi Chemical), Wilmington, DE 19880; Tel. 1-800-346-5656.

polyimides can be patterned using standard optical lithography. Polyimides used in this work were chosen from the manufacturer's[1] series PI 2500 and PI 2720. In particular, we have used polyimides PI 2525, PI 2556 and PI 2729. Polyimides from the PI 2500 series are not photosensitive, so they cannot be patterned using optical lithography. We have used these polyimides for the cases when we did not have to pattern the insulator. An example of a micro-electromagnet structure fabricated using PI 2556 is described below in Fig. 7.2. In contrast, polyimides from the PI 2720 series can be patterned using optical lithography. These polyimides were used to fabricate 3D micro-electromagnets shown in Fig. 7.1.

Polyimide thickness up to tens of μm can be achieved by controlling the spinning rate and the thermal curing time and temperature. Longer spinning times improve coating uniformity, but reduce the film thickness. The film thickness is also reduced by thermal curing. The thermal curing procedure depends on the polyimide composition, and on the final thickness that is desired[1]. The curing recipe for PI 2729 is outlined in the next paragraph.

The fabricated devices shown in Fig. 7.1 use polyimide PI 2729 that can be produced in a thickness range from 10 μm to 70 μm. Polyimide PI 2729 can be patterned using optical lithography. The fabrication procedure for 10 μm to 20 μm thick films of PI 2729 is as follows: clean the substrate in acetone, methanol and TCE as described in Chapter 4, spin polyimide for 30 s at 5000 rpm on a cleaned and completely dried substrate; soft bake on a hot plate for 3 min at 100 °C, expose to UV light for 40 s in the Karl Suss Stepper in the cleanroom, develop in DE 6180 for 40 s, and rinse vigorously in RI 9180 for 20 s, blow dry for 20 s; thermally cure on a hot plate (120 °C for 30 min, then ramp up to 260 °C at 2 °C/min, 260 °C for 100 min., then ramp down to 20 °C at 2 °C/min). Any subsequent polyimide layer is fabricated using the same procedure. The polyimide developer DE 6180 (cyclohexanone 70% and butyrolactone 30%) and rinse

RI 9180 (butyl acetate 85% and cyclohexanone 15%) can be used for all polyimides in the PI 2720 series.

The current density in fabricated three-dimensional structures like those in Fig. 7.1 at room temperature can reach $\approx 10^8 A/cm^2$. Cryogenic cooling can reduce wire resistance and power dissipation if necessary. Magnetic fields in micro-electromagnets are produced by electric currents and can be changed rapidly. For the 3D trap in Fig. 7.1(a) the current time constant is $L/R = 20$ ps, with inductance $L = 0.1$ nH and resistance $R = 5\ \Omega$. Fast modulation of the magnetic field is an advantage of micro-electromagnets over permanent magnet structures which require physical motion to generate time dependent fields.

In order to test thermal conductivity of polyimide and to measure the maximum current that can be supported by the top layer, we have fabricated a two-layer micro-electromagnet on a sapphire substrate shown in Fig. 7.2. The device consists of two mirrors with similar resistances fabricated one on top of the other and insulated with several layers of non-photosensitive polyimide PI 2525. The wire width was ~ 50 μm and the thickness was ~ 0.1 μm. The polyimide layer separating the two mirrors was ≈ 20 μm thick. The two mirrors were connected in series and a constant current was applied to them at room temperature. The top mirror failed[2] first at current $I \approx 1$ A, corresponding to ≈ 5 W of constant power dissipation.

[2] The resistance of the top mirror instanteneously jumped up four times.

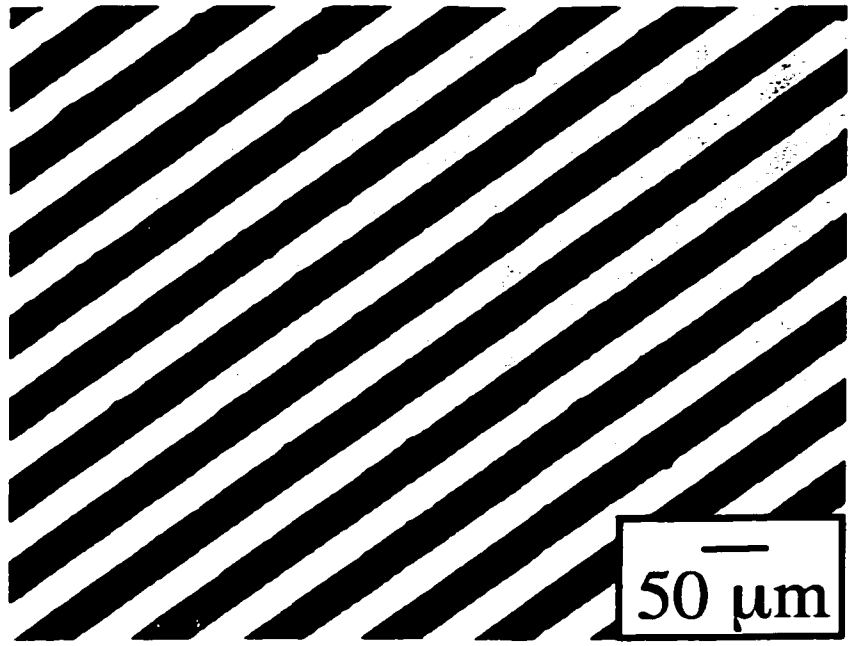

FIG.7.2 Two micro-electromagnet mirrors separated with a ≈ 20 μm thick layer of non-photosensitive polyimide PI 2556.

7.4 Coupled 3D Traps

Figure 7.3 shows a 3D micro-electromagnets which forms a double trap with adjustable trap coupling as well as a toroidal trap. Both structures are interesting for quantum computing [Jaksch D. *et al.*, 1999; Vernoy D.W. *et al.*, 1998]. As shown in Fig. 7.3(a) the trap is composed of three coaxial current loops of radius R separated by equal distances $d = R$. The evolution of trap geometry is shown by plots of magnetic field magnitude in Figs. 7.3(b) to 7.3(f) as the ratio I_1/I_2 is increased from 0.8 to 2.2, with I_1 the current in the top and bottom loops and I_2 the current in the middle loop. Particles are trapped in low magnetic field regions shown in red. Figures 7.3 (b) to 7.3 (d) show two traps coupled by adjustable inter-trap tunneling controlled by I_1/I_2, Fig. 7.3 (e) shows a single simply connected trap, and Fig. 7.3 (f) shows a single toroidal trap of variable aspect ratio.

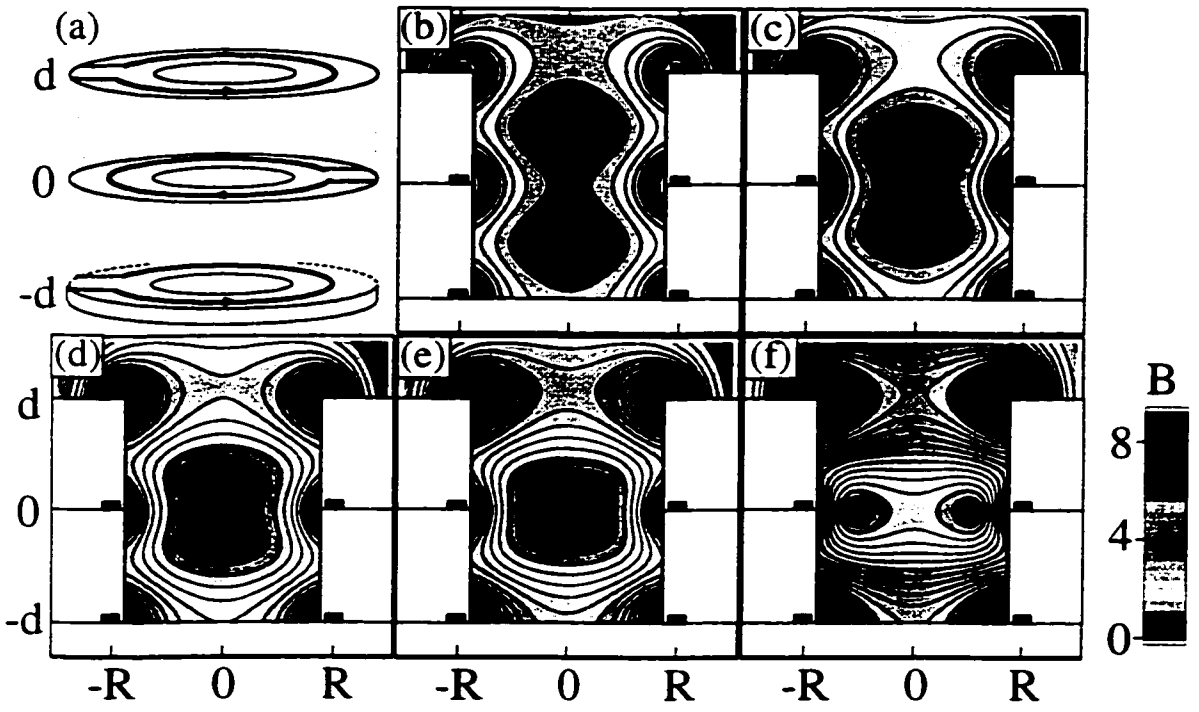

FIG. 7.3 Three-dimensional micro-electromagnet trap with three current loops: (a) schematic diagram, (b) to (f) contours of constant magnetic field magnitude B about the trap center. (b) to (d) Two coupled traps are formed with a variable barrier as the ratio of currents in the two outer rings I_1 and the middle ring I_2 is varied: (b) $I_1/I_2 = 0.8$, (c) $I_1/I_2 = 1.0$, and (d) $I_1/I_2 = 1.2$. (e) A single trap is formed for $I_1/I_2 = 1.4$. (f) A toroidal trap is formed for $I_1/I_2 = 2.2$. Magnetic field contours are spaced by $\Delta B = 10$ mT for $R = d = 1$ μm and $I_2 = 0.1$ A.

Adjustable double traps are a building block of quantum circuits for atoms. For the sequence of double traps Figs. 7.3 (b) to 7.3(d), the individual trap depth is largest for $I_1/I_2 = 0.73$ ($B_{max} \approx 30$ mT for $d = R = 1$ μm and $I_2 = 0.1$ A). The potential barrier is lowered in Fig. 7.3(d) where the traps are pushed together with increased inter-trap tunneling, forming states analogous to molecular bonds. Artificial molecules have been

formed in tunnel-coupled semiconductor quantum dots with electrons [Livermore C. *et al.*, 1996]. In the case of atoms, the formation of such bonds could be characterized spectroscopically. As in the NH_3 molecule, the lowest energy states are symmetric and anti-symmetric superpositions of the two single trap wavefunctions[3]. By adding more loops one can construct an array of coupled traps where particles can move from one trap to the next. These could be a new tool to entangle neutral atoms for quantum computation [Jaksch D. *et al.*, 1999].

Once the double traps join, a single trap is formed as shown in Fig. 7.3 (e). Here the field magnitude B increases quadratically away from the center, unlike the linear increase for single two-coil traps in Figs. 7.1(a) and 7.3(b). The trap depth for Fig. 7.3 (e) is $B_{max} \approx 80$ mT for $I_1/I_2 = 1.4$, $d = R = 1$ μm, and $I_2 = 0.1$ A. and $B = 0$ at the trap center. For higher ratios, $I_1/I_2 > 1.4$, B becomes nonzero at the center. A spherical hexapole three-coil trap with $B = 0$ in the trap center [Bergeman T. *et al.*, 1987] is obtained if the radius of the outer rings and the separation d are both $R/\sqrt{2}$, and $I_1/I_2 = 1$.

A toroidal trap occurs when the current ratio is $I_1/I_2 > 1.8$, as shown in Fig. 7.3 (f). Toroidal traps are a possible approach for quantum computers based on coupled ions [Vernoy D.W. *et al.*. 1998]. Micro-electromagnet toroidal traps could confine cold plasma into small volumes ~ 10^{-9} mm^3. Recently, cold neutral plasma consisting of electrons at 100 mK and ions at 10 μK has been produced [Killian T.C. *et al.*, 1999]. For

---

[3] The oscillation frequency can be estimated semi-classically using a simplified one-dimensional model of a symmetric double well in the z-direction to be $\omega = \Delta E/\hbar = (E/\pi\hbar)\exp[-\int_{z_1}^{z_2}\sqrt{2m(V(z)-E)}dz]$; ΔE is the energy level splitting between the asymmetric and symmetric states, E is the ground state energy in the upper and lower traps, $V(z)$ is the barrier potential; z_1 and z_2, defined by $E = V(z)$, determine the spatial extent of the coupling. For $R = 1$ μm, $I_1/I_2 = 0.14$, $I_2 = 0.1$ A, we estimate $\omega = \Delta E/\hbar \approx 4MHz$ (*or* $32\mu K$) (Fig. 3 (e)) for $E/\hbar \approx 56MHz$ (*or* $450\mu K$).

Fig. 7.3(f) the trap depth is $B_{max} \approx 16$ mT, with $R = 1$ μm, $I_1 = 0.1$ A and $I_1/I_2 = 2.2$. As the current ratio I_1/I_2 increases above 2.2, the trap is pushed further out and the trap depth and gradient increase.

In summary, we have designed and fabricated three-dimensional micro-electromagnets consisting of layers of metal wires separated by layers of transparent insulators. We have described the fabrication and magnetic field configurations of three-dimensional traps and three-dimensional guides. It was also illustrated how micro-electromagnets can be combined to make integrated devices: a three-dimensional trap on top of a micro-fabricated mirror, two micro-electromagnet mirrors one on top of the other, and two coupled 3D traps. Although we have not used these devices in actual experiments with neutral atoms, we expect that three-dimensional micro-electromagnets will be powerful new tools for experimental atom mesoscopics.

Chapter 8

MICROSCOPIC TRAPS FOR COLD ELECTRONS IN VACUUM

In this Chapter we describe how micro-electromagnets can be used for manipulation of electrons in vacuum using a combination of electric and magnetic fields. Small electron traps modeled upon a Penning trap are proposed. Possible approaches to design traps, and to integrate them with electron sources and electron detectors within a cryogenic system in vacuum are discussed.

8.1 Introduction

The interest in vacuum-based microelectronics has been growing with the capabilities to build vacuum devices to small sizes similar to those found in solid state devices. Unlike collision-dominated transport in semiconductors, electrons in vacuum can travel ballistically over long length scales. When the mean free path of an electron $\lambda > d$, where d is the device dimension, the electron scattering from the residual gas is negligible. Advantages of electron transport in vacuum are speed, insensitivity to ambient temperature, and insensitivity to radiation damage.

Vacuum microelectronic devices such as miniaturized vacuum-tubes, transistors and electron guns, as well as miniaturized electron sources have been successfully realized [see for review *Proceedings from the International Vacuum Microelectronics Conferences*]. Spindt-type field emitters consisting of ~ 1μm molybdenum cones were fabricated using electron beam lithography and metal evaporation three decades ago [Spindt C.A., 1968]. Nanofabricated emitters have been integrated into many small, vacuum-sealed devices.

In this work we are interested in controlling low energy electrons (E << 1 eV) which will permit the study of low-dimensional, tightly confined gases and open a range of possible mesoscopic experiments. Control of electron motion in vacuum tubes has been limited to higher electron energies E >1 eV, where high current densities and high electron energies[1] are preferable.

Micro-electromagnet traps can be constructed for electrons in vacuum, forming an "artificial atom" interesting for new experiments. Electrons trapped in vacuum potentially suffer less from interference from defects than quantum dots in semiconductors, and could permit the study of low-dimensional systems. The general idea behind the traps can be extended to other devices for electron manipulation. Control of electrons on microscopic scales opens applications including integrated electronic circuits in vacuum, quantum dots in vacuum, and possible implementation of quantum computers [Mancini S. *et al.*, 2000]. Due to their lower mass, electron motion in traps is 2 to 3 orders of magnitude faster than atoms, which can be advantageous for applications.

[1] E = 86 μeV corresponds to T = 1 K.

8.2 The Physics of Electron Trapping

Figure 8.1 illustrates a simple electron microtrap, composed of a conducting ring at $V_o > 0$ and a homogeneous magnetic field $\vec{B}$ along the z–axis. Near $z = 0$, this approximates a Penning trap [reviewed in Brown L.S. and Gabrielse G., 1986], consisting of a quadrupole electrostatic field binding the electron in the z- direction and a magnetic field creating a circular orbit about the z-axis. The electron is attracted to the space inside the positive ring and trapped when the magnetic field magnitude $B > B_{min} \approx 1/a\sqrt{2mV_o/e} = 3.2\sqrt{V_o}/a\ [T\,\mu m/\sqrt{V}]$. Inside the trap, the electron motion can be decoupled into three independent harmonic oscillators [see Brown L.S. and Gabrielse G., 1986]: axial, cyclotron and magnetron with frequencies ω_z, ω_c, ω_m and lifetimes Γ_z, Γ_c, Γ_m, respectively. Due to the dissipative magnetron motion, the trap is metastable and the electron will drift out of the trap after a magnetron lifetime Γ_m.

The equations to calculate the frequencies ω_z, ω_c, ω_m and lifetimes Γ_z, Γ_c, Γ_m of a single electron inside the trap are given in the rest of this section. In Table 8.1 we list the calculated frequencies and lifetimes for two traps with radii a = 1 μm and a = 10 μm, in external magnetic fields $B > B_{min}$, and a voltage V_o = 0.1 V applied to the traps. As indicated, the electron frequencies inside small traps are high, in the GHz range, and the calculated lifetimes can be long. For a trap with a = 1 μm, the magnetron lifetime $\Gamma_m \approx$ *5 hr* at B = 4 T, while for the larger trap with a = 10 μm, the magnetron lifetime $\Gamma_m \approx$ *7 months* at B = 0.7 T. The cyclotron and axial radiation can be in thermal equilibrium with the background radiation field.

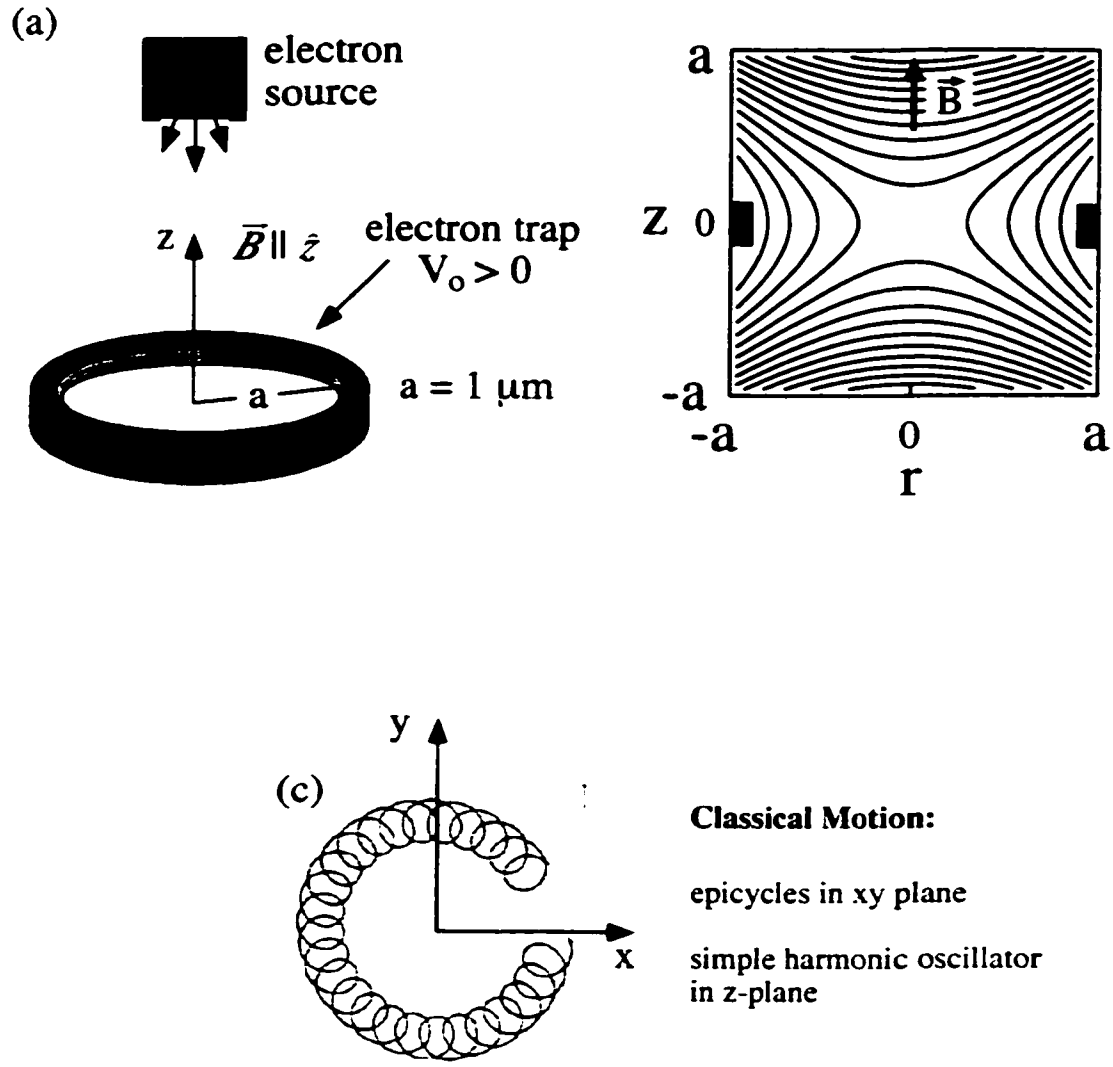

FIG. 8.1 (a) Schematic diagram of a simple micro-electromagnet electron trap consisting of a conducting ring of radius a held at voltage V_o in the external magnetic field along the z-axis, and (b) contours of constant electric potential for the conducting ring, (c) schematic diagram of classical electron motion. In the xy plane of the ring electrons move in epicycles with a small cyclotron orbit and a larger magnetron orbit; in the z-direction, the electron oscillates harmonically.

The Hamiltonian of a single electron inside the trap is

$$H = \left(\vec{p} - e\vec{A}\right)^2 / 2m + eV_o(z^2 - \rho^2/2)/2a^2 \tag{8.2.1}$$

The minimum B-field needed to trap an electron is derived from $\omega_c^2 - 2\omega_z^2 > 0$.

The axial, cyclotron and magnetron frequencies are

$$\omega_z = \sqrt{eV_o/ma^2} = 420\sqrt{V_o/a^2}\,[GHz\ \mu m/\sqrt{V}], \tag{8.2.2a}$$

$$\omega_c' = 1/2(\omega_c + \sqrt{\omega_c^2 - 2\omega_z^2}), \tag{8.2.2b}$$

$$\omega_m = 1/2(\omega_c - \sqrt{\omega_c^2 - 2\omega_z^2}), \tag{8.2.2c}$$

where $\omega_c = eB/m = 176\ B$ [GHz/T],and B is the magnitude of the external magnetic field. The axial, cyclotron and magnetron lifetimes are

$$\Gamma_z = 2\Gamma_z(\omega_c'/\omega_z')^2, \tag{8.2.3a}$$

$$\Gamma_c' \approx 8\ 10^4(\omega_c' - \omega_m)/\omega_c'^3\ (GHz^2 s), \tag{8.2.3b}$$

$$\Gamma_m = (\omega_c'/\omega_m)^3\Gamma_c'. \tag{8.2.3c}$$

The energy eigenstates including spin motion are

$$E_{nkls} = \hbar\omega_c'(n + 1/2) + \hbar\omega_z(k + 1/2) + \hbar\omega_m(l + 1/2) + s/2\hbar\omega_s. \tag{8.2.4}$$

TAB. 8.1

a [μm]	V_0 [V]	B_{min} [T]	B [T]	$\omega_c/2\pi$ [GHz]	$\omega_z/2\pi$ [GHz]	$\omega_m/2\pi$ [GHz]	Γ_z [s]	Γ_{c^-} [s]	Γ_m
1	0.1	1	4	110	20	2	8	0.2	5 *hr*
10	0.1	0.1	0.7	20	2	0.1	900	5	7*mths.*

Table 8.1 Calculated frequencies ω_z, ω_{c^-}, ω_m, and lifetimes Γ_z, Γ_{c^-}, Γ_m, for two micro-electromagnet electron traps, with radii a = 1 μm and a = 10 μm, in the external magnetic field B; the minimum magnetic field to trap one electron is B_{min}.

8.3 Electron Sources

Electrons are available from a variety of sources: photo-, thermal-, electric field-emission, and even radioactive sources have all been successfully used in a low temperature environment. For example, in studies of two-dimensional electron gases (2DEGs) formed on liquid helium surfaces, electrons are deposited on a liquid helium film either by charging a thermionic filament, by photo-emission from materials with a low work function, or by field-emission from a sharp tip [for review see *Two-dimensional Electron Systems: on Helium and Other Cryogenic Substrates*, (ed. Andrei E.Y.), 1997]. In the rest of this section, we give a short overview of electron sources.

Field-emission is commonly used to load electrons into macroscopic Penning traps. High electric fields (~ 100 V/μm) applied between a sharp tip and the anode produce high-energy electrons (E ~ keV) [see for review Brodie I, Schwoebel P.R., 1994]. These high-energy electrons cause a secondary emission of low-energy electrons from the surrounding surfaces and the residual gas that will get trapped into a Penning trap[2].

[2] G. Gabrielse, personal communication.

Electrons can be also generated by heating and illuminating surfaces to form an electron space charge around the emissive material [see for review Klemperer O., 1953; Van der Bijl, H.J., 1920]. Photoemissive materials have low work functions A. Alkali metals like Na, K and Cs are the usual constituents of photoemissive materials. Normal metals like Zn, Cu and Au have relatively low work functions and emit electrons when illuminated with UV light. Other photoemissive materials include semiconductors (GaAs, InGaAs, Sb) activated with alkali metals, sensitive to infrared radiation, and other engineered materials (such as multialkali) to achieve a desired sensitivity to a particular range of wavelengths. The difficulty in using alkali-based materials is their reactivity. Once these materials are activated, they have to be kept in vacuum. Normal metal films are easy to deposit and handle and require UV light.

We have tested Sb doped with a combination of alkali metals (Na, K and Cs)[3], illuminated with a red He-Ne laser and measured electron current densities ~ $\mu A/cm^2$. Arrays of nanofabricated photocathodes using cesiated GaAs that emit polarized electrons when illuminated with polarized light have been developed[4].

Thermal emitters generate high electron densities saturating at $i \propto T^2 e^{-A/k_B T}$, where k_B is the Boltzmann constant, T is the emitter temperature and A is the work function. Among the different electron sources, we have tested tungsten filaments[5] in the low temperature setup, shown in Fig. 8.2. This setup could also be extended to integrate the electron source with micro-electromagnet electron traps in an external magnetic field[6] .

---

[3] Available from Hamamatsu Photonics, http://www.hamamatsu.com/.

[4] John Wiener, Universite Paul Sabatier, France, communication. The dots of cesiated GaAs are produced using standing optical waves above a substrate to focus a slow beam of Cs atoms.

[5] The filaments (Ta, BaO, W, LaB_6) and electron optics are available from Kimball Physics, Inc., Wilton, NH, 03086; Tel. (888) 546-7497; http://www.kimphys.com/. Tungsten filaments generate the highest electron densities.

[6] The magnetic field is generated by a water-cooled electromagnet with coils carrying electrical current up to I = 35 A, manufactured by *Walter Scientific, Inc.*. The maximum field produced depends on the magnet pole separation d; for d = 3.75 cm and I = 35 A, the measured field is B = 0.7 T.

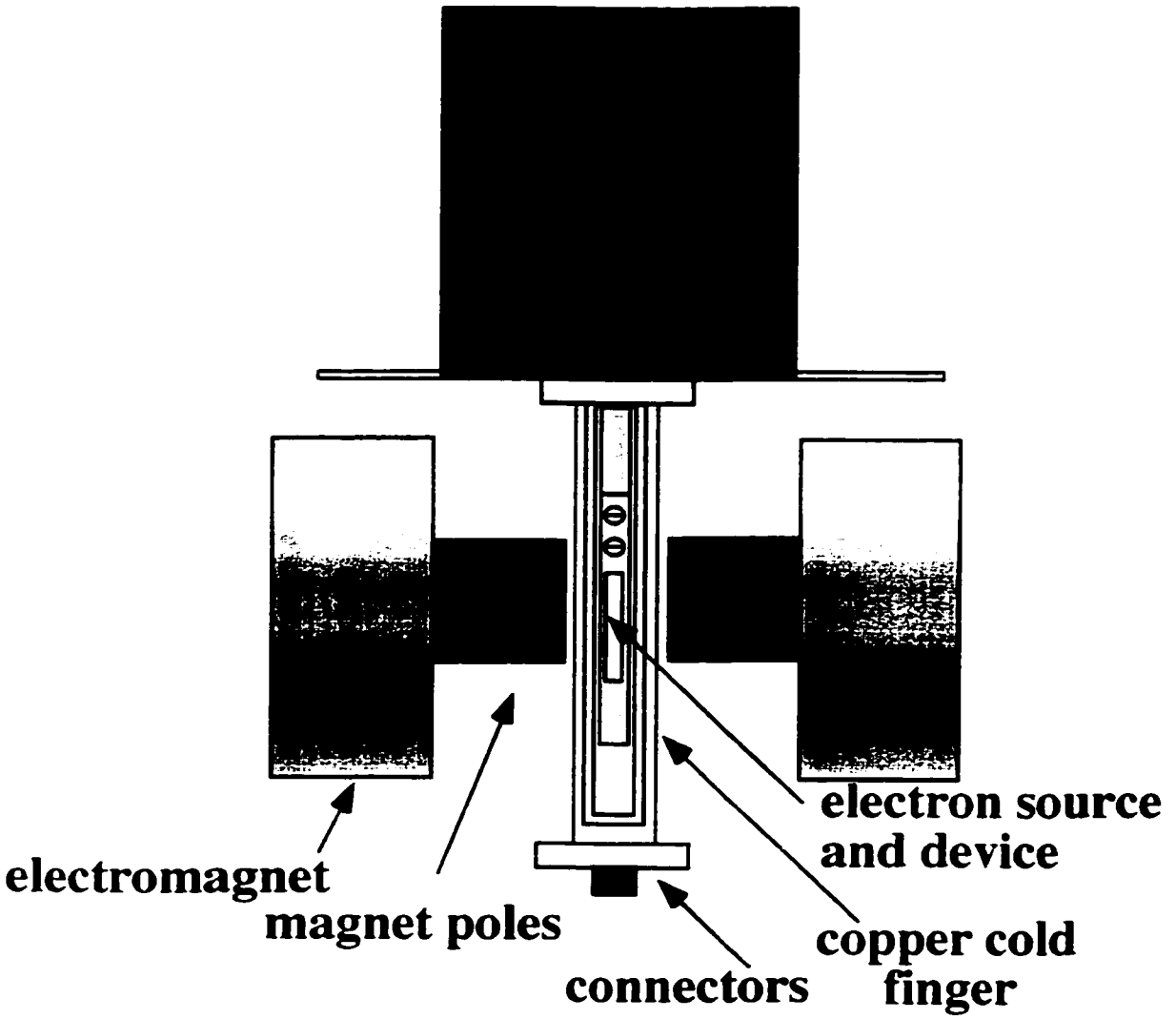

FIG.8.2 Schematic diagram of the experimental setup built to test electron filaments. This setup can be also used to integrate an electron source with a micro-electromagnet trap in vacuum. A copper cold finger is used for cooling to LHe temperatures using the same dewar as in Chapter 5. The cold finger is placed inside an external magnetic field produced by a water-cooled electromagnet.

The box shown in Fig.8.3 (a) is located on a copper cold finger 12 cm below the LHe bath (see also Fig. 8.2) and surrounded by a copper shield at 77K. The filament is supported with a ceramics mount and a teflon spacer. The electron collector is a Au/Cr square deposited on a GaAs/AlGaAs chip mounted inside the box at 4K. The inner cold

finger radius is 3/8", and it is surrounded by a copper radiation shield cooled to 77K. The vacuum space is defined within a narrow stainless steel tube with diameter $d = 3.75$ cm and length $L = 15.5$ cm (see Fig. 8.2). Vacuum levels down to 10^{-8} torr have been obtained.

A silicon diode thermometer, GE varnished on a sapphire substrate near the collector, is used to monitor the temperature of the cold finger four-terminally. The collector, thermometer and filament leads are connected on the bottom of the vacuum space through a multi-connector cable, which gives us electrical access to the devices. The total resistance between the two pins on the connector at the bottom of the vacuum space that connect in series to the copper leads and the tungsten filament is $R < 1\ \Omega$. Special care has to be taken to heat sink the collector and thermometer leads at 4K and then at 77 K. The electron filament leads are thermally isolated from the 4K box and heat sunk at 77K.

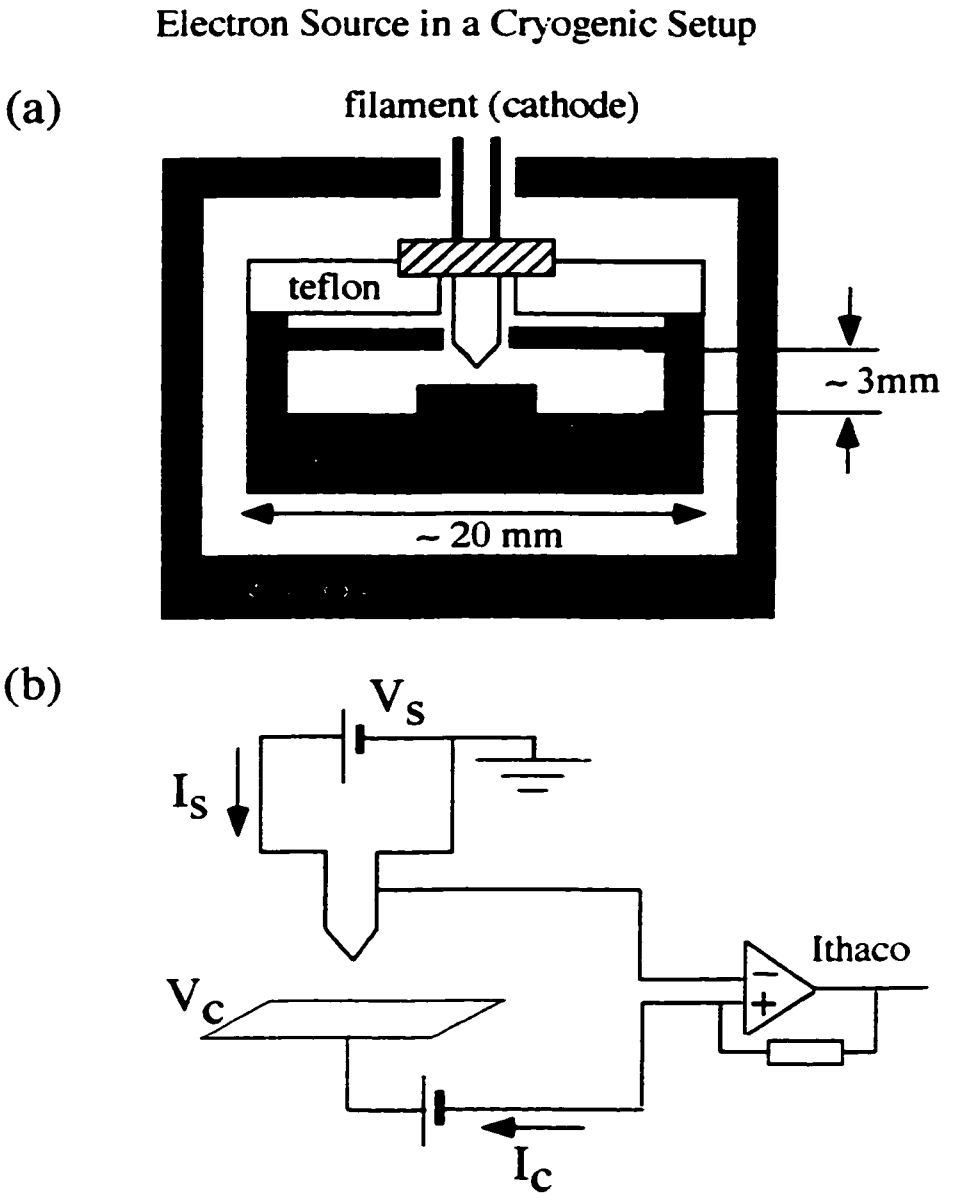

FIG.8.3 (a) Close-up view of the setup built to integrate an electron filament and collector at 4 K. The filament is insulated from the cold finger with a ceramic mount and teflon spacer, and the contact area with copper has been minimized. The box at 4 K is surrounded by a 77 K copper shield, and a collector is placed below the filament to measure the electron current. The micro-electromagnet electron trap could be implemented in this setup instead of the collector. (b) Circuit diagram to energize the electron source with voltage V_s and measure the electron current reaching the collector I_c, as a function of the collector potential V_c and the current passing through the source I_s. The electron current I_c is amplified using an Ithaco preamplifier.

The electron current reaching the collector I_c was measured as illustrated schematically in Fig.8.3 (b). Current I_s was applied to the tungsten filament and the current of emitted electrons I_c was measured as a function of the voltage V_c between the collector and the filament. The measured emitted current I_c increases sharply for filament currents above the threshold $I_s > I_{th} \sim 2$ A, and saturates as a function of collector voltages V_c, for a fixed filament current I_s. Current densities up to ~ 1 mA/cm^2 have been measured. Even a much smaller current density of 1 pA/cm^2 corresponds to a large number of electrons $N = 6 \times 10^8$ hitting a 1 μm^2 area per second. To load an electron trap, it is sufficient to operate the filament at small I_s, close to the threshold I_{th}.

When a negative voltage V_c is applied between the filament and the collector, the electron current I_c, for a fixed I_s, can be tuned down to zero. The emitted electron energies estimated in this way are $E \sim 0.1$ eV ($T \sim 1000$ K) for $I_s \sim 2$A. The filament current I_s can also be pulsed using a function generator and a Kepco power supply. The measured thermal time constant of the tungsten filament is $\tau \sim 1$ s, limiting the shortest pulse duration.

8.4 Electron Detectors

Trapped electrons could be detected and measured using a variety of techniques ranging from capacitance and charge measurement [*Mesoscopic Electron Transport* (eds. Sohn L.L., Kouwenhoven L.P., Schon G), 1996], to resonant frequency measurements, as in macroscopic Penning traps [Brown L.S. and Gabrielse G., 1986]. In semiconductor quantum dots, electron charge detection is effective using single-electron transistors [Duncan D. *et al.*, 1999]. In macroscopic Penning traps, electron detection is achieved by driving the axial motion along $\vec{B}$ with an alternating voltage applied to the trap electrodes and observing the resulting driven oscillation with phase-sensitive detection. Because the electron frequencies in a small, micro-electromagnet trap are high (in the GHz range), resonant frequency measurements are more difficult than for macroscopic Penning traps. In this work we propose an approach based on single electron detection in semiconductor microstructures [*Mesoscopic Electron Transport* (eds. Sohn L.L., Kouwenhoven L.P., Schon G), 1996].

A quantum point contact (QPC) [van Wees B.J. *et al.*, 1988] formed on a 2DEG subsurface contained in a GaAs/AlGaAs heterostructure and placed near the electron trap can be sensitive to the presence of electronic charges in the trap. The signature of trapped electrons would be the change in the QPC conductance G_{SD} due to capacitive coupling between the electrons in the trap and those in the two-dimensional electron gas (2DEG). The point contact schematic and scannning electron microscope (SEM) micrograph of a fabricated device are shown in Figs. 8.4 (a) and (b), respectively. Etching the heterostructure depletes the 2DEG underneath, and allows us to define narrow point contact channels. The QPC will be electrically isolated from the surrounding 2DEG reservoir by the etched regions. Fabrication consists of electron beam lithography, evaporation, thermal annealing, and ion milling, details of which are described in Appendix *C*.

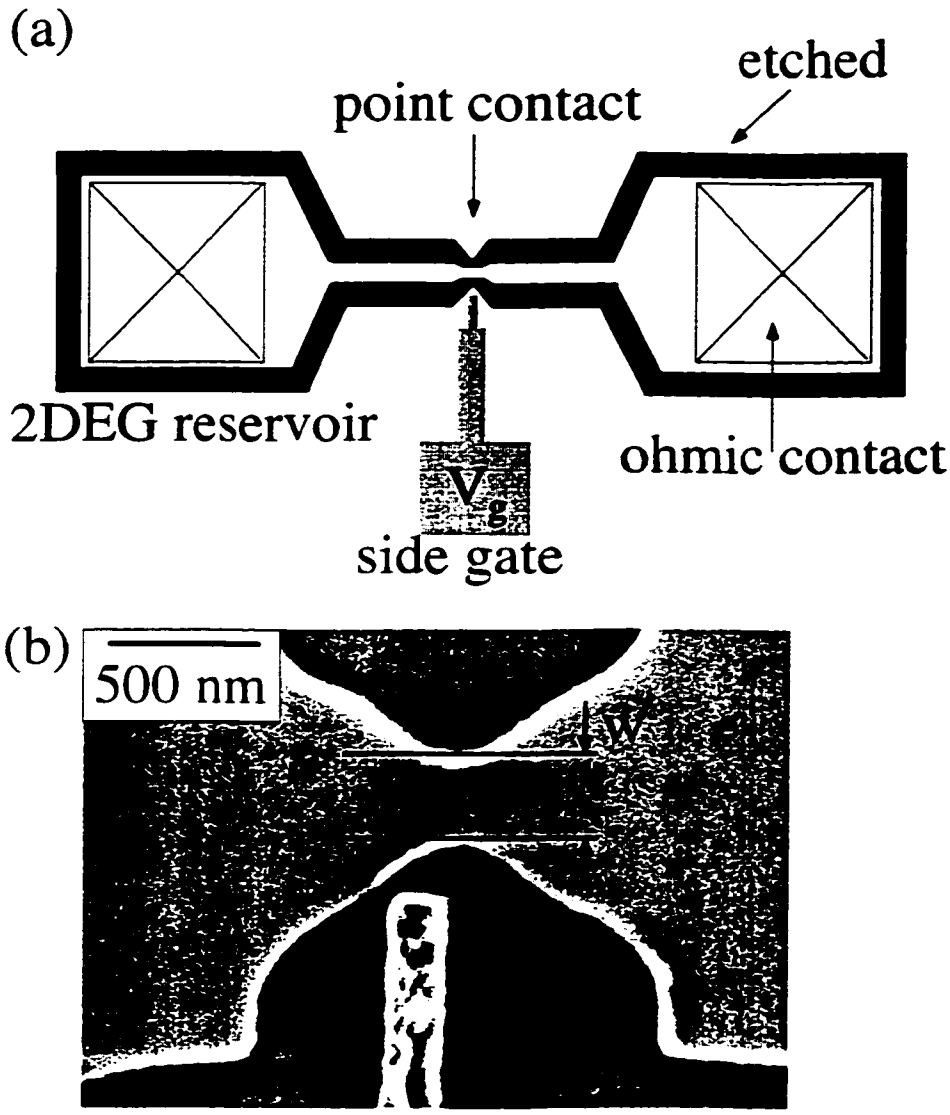

FIG.8.4 (a) Schematic diagram of a quantum point contact defined by an etched trench (black line) to separate the 2DEG from the surrounding 2DEG reservoir. A metal gate at negative voltage V_g (with respect to the ohmic contact) is used to tune the electron sheet density in the point contact. (b) SEM picture of a fabricated point contact with width w = 280 nm and etch depth z = 40 nm.

Figure 8.5 shows the conductance G_{SD} between the source and the drain vs. the gate voltage V_g, in units of the conductance quantum $2e^2/h$, for QPCs with different width w and trench depth z, fabricated in two different GaAs/AlGaAs wafers with triangular (wafer A) and square (wafer B) electron wells[7]. The conductance G_{SD} is measured at 4.2 K by biasing the QPC at low voltages (V_{sd} = 10 μV) with a ν=13 Hz sinusoidal signal. As shown, G_{SD} exhibits steps at $G_{SD} = N\,2e^2/h$ where N is the number of transverse modes in the QPC [Beenaker C.W.J. and van Houten, H., 1991].

The metal gate next to the quantum point contact (QPC) can be used to control the QPC conductance G_{SD}. As seen in Fig. 8.4 (a), a metal gate is fabricated to the side of the QPC. By varying the voltage V_g on this side gate, we can control the QPC conductance G_{SD}. Specifically, the conductance can be tuned to lie in between the plateaus. Here, the conductance changes sharply, and the QPC is sensitive to external electric charges [Field M. *et al.*, 1993]. A QPC can be then used to detect trapped electrons.

An electron trap illustrated in Fig.8.1 could be integrated with a QPC in Fig.8.4. The integrated device could consist of a metal ring, to trap the electron, surrounding a point contact below the trap center to detect the electron. Because the trap would be close to the dielectric surface of the GaAs/AlGaAs substrate, the simple picture of a metal ring presented in section 8.2. has to be corrected. For example, the presence of image charges in the dielectric can attract the electrons toward the surface and destroy the trap. The image charge of an electron in vacuum above the GaAs surface (ε_r = 13) is q = + (6/7) e, which corresponds to an attractive potential of ~ 10 mV at a distance z = 50 nm above the surface. This effect can be reduced by making the ring tall, adding an insulating layer, or adding a negative electrode to repel the electrons from the surface.

[7] wafer A: # 990924A, wafer B: # 990942B. The wafers were grown by Kevin Maranowski at UCSB.

The trap geometry and other surrounding metal and dielectric surfaces must be carefully designed in order to trap electrons.

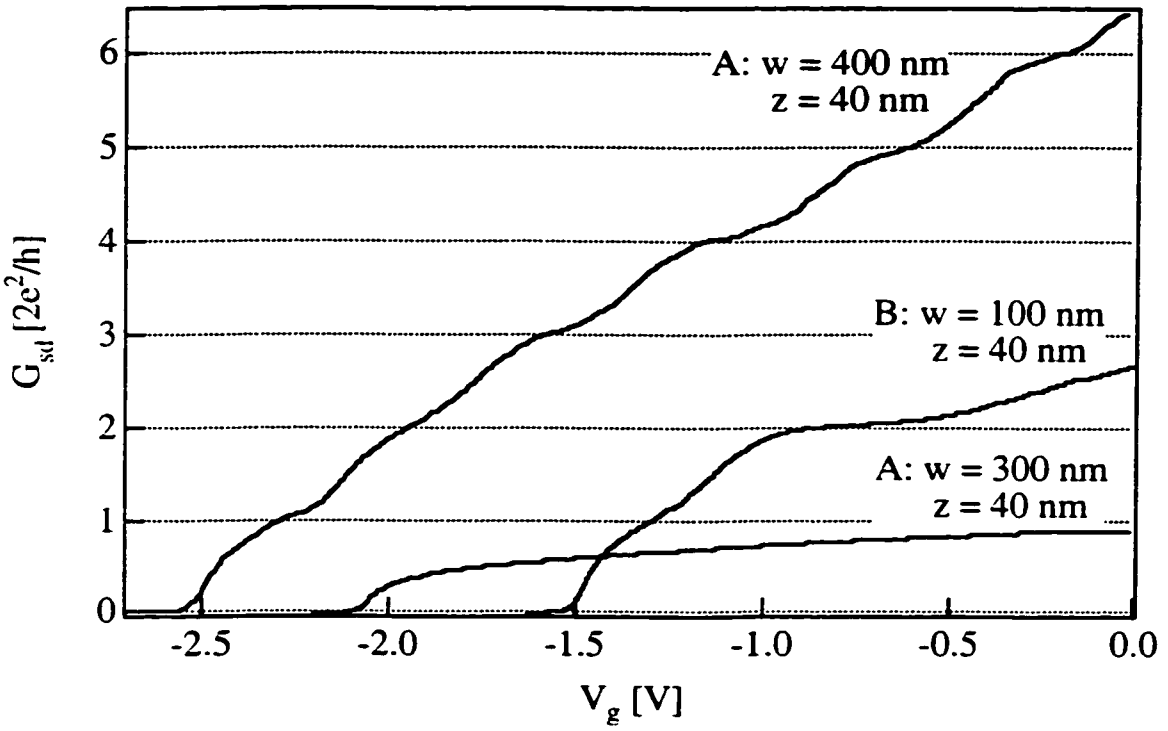

FIG.8.5 Conductance G_{SD} of point contacts at 4.2 K as a function of gate voltage V_g for different widths w, and etch depths z, in two wafers with a triangular well (A) and square well (B).

In summary, it might be possible to realize micro-electromagnet traps for electrons in vacuum based on small microfabricated wires. The proposed electron trap is modeled upon a Penning trap and consists of a metal ring held at a positive voltage inside an external magnetic field. The estimated lifetimes of electrons inside a small trap can be long, up to several months, while the estimated electron frequencies are high, in the GHz range. We also proposed how to integrate electron traps with electron sources and

electron detectors inside a vacuum system at liquid Helium temperatures. In this work, we have used thermal emitters to generate electrons. Possible approaches to detect electrons using quantum point contacts were discussed.

Chapter 9

Conclusions and Future Directions

In this Chapter we summarize the major results described in previous chapters, and present some ideas for future work. The major result of this Thesis is the development of novel micro-electromagnet devices [Drndic M. *et al.*, 1998] for the control of neutral particles with spin, such as neutral atoms and molecules. Micro-electromagnets consist of small current-carrying wires and generate magnetic field configurations that can be used to reflect, trap and guide atoms. The control of atom motion using micro-electromagnets is based on the magnetic-dipole interaction between the magnetic moment of the atom, and the magnetic field produced by current-carrying wires.

In this Thesis we have described the design, fabrication and properties of micro-electromagnet mirrors. They consist of serpentine wire patterns and produce exponentially decaying magnetic fields to reflect neutral particles with spin. We have described the mirror design in Chapter 3, and the mirror fabrication, as well as the electrical and thermal properties of the mirrors, in Chapter 4. Micro-electromagnet mirrors were successfully used to deflect fast He atoms (Chapter 5) [Drndic M. *et al.*, 1998; Johnson K.S. *et al.*, 1998] and to reflect slow Rb atoms (Chapter 6) [Drndic M. *et al.*, 1999; Cognet L. *et al.*, 1999]. The important mirror properties are summarized below.

(*i*) The first important property of micro-electromagnet mirrors is the maximum magnitude of the magnetic field produced at the surface of the micro-electromagnet mirror. This maximum B-field magnitude determines the maximum energy of atoms that can be reflected from the mirror. For the fabricated micro-electromagnet mirrors,

described in Chapter 4, the maximum surface field achieved is ~ 0.1 T. This means that the fabricated mirrors can reflect cold atoms moving at velocities up to v ~ 10 m/s. Indeed, the atomic reflection was experimentally confirmed in Chapter 6, in the example of cold Rb atoms reaching the mirror at velocities v ~ 1 m/s. For fast atoms at room temperature, moving at high speeds v ~ 1000 m/s, the magnetic field produced by the fabricated mirrors is not sufficient to reflect atoms at normal incidence. In this case, atoms can be deflected from the mirror at grazing incidence. The experimental results confirming the deflection of He atoms travelling at v ~ 1800 m/s were described in Chapter 5.

(*ii*) The second important micro-electromagnet mirror property, described in Chapters 3 and 6, is the mirror specularity. The specularity of a mirror can be defined as the angular spread in the reflection angles of an atomic beam that is being reflected from the mirror at normal incidence. If the mirror is perfectly specular, it will not introduce any additional angular spread in the atom distribution being reflected. In practice, every mirror is corrugated to some extent. In the case of micro-electromagnet mirrors, we have measured the angular spread ~ 10 mrad for the reflected Rb atom distributions. This was described in Chapter 6.

The micro-electromagnet mirror specularity depends in a nontrivial way on the details of the mirror geometry. In this Thesis, we have identified several factors that strongly affect the mirror specularity and are related to the finite size of the micro-electromagnet mirrors. In Chapter 3 we showed that the mirror is most specular if the number of wires in the serpentine mirror array is odd, rather than even. This was confirmed experimentally in Chapter 6, when Rb atoms were reflected from micro-electromagnet mirrors with odd and even numbers of wires.

The mirror specularity also depends strongly on the cross-sectional shape and separation of the microfabricated wires. This was a surprising theoretical result

[Zabow G. *et al.*, 1999] that can be understood from the magnetic field calculations above the wires with different shapes. In Chapter 3, we have described that oval-shaped wires can produce up to two orders of magnitude more specular mirrors than rectangular wires with the same wire spacing. The fabrication of oval-shaped wires is achieved using electroplating, as described in Chapter 4.

Finite-sized micro-electromagnet mirrors are most specular at an optimal finite height above the surface of the wires. As described in Chapters 3 and 6, this is a consequence of the finite number of wires in the serpentine array. The optimal height above the wires where the mirror is most specular, depends on the number of wires and on the cross-sectional shape of the wires. In Chapter 6, we have described the experimental results demonstrating this effect.

The specularity of finite-size mirrors can be improved by adding compensating wires to mimic the behavior of a perfectly specular mirror. This idea comes from the work on compensated mirrors formed from an array of permanent magnets [Sidorov A.I. *et al.*, 1996]. As described in Chapter 6, we have fabricated micro-electromagnet mirrors with the additional compensated wires and we have demonstrated the improvement of mirror specularity over the uncompensated mirrors.

(*iii*) The third important property of micro-electromagnet mirrors, which sets them apart from permanent-magnet structures, is their capability to produce rapidly changing time-dependent magnetic fields. This is possible because the magnetic fields in micro-electromagnets are produced by current-carrying wire patterns with small electrical and thermal time constants. In Chapter 5, we have applied linearly ramped electrical current pulses to the mirror in order to narrow the spatial distributions of the deflected He atoms. In a similar way, the mirror specularity could be improved by exploiting time-dependent currents. It would be also interesting to use time-dependent currents to

experimentally study the nonlinear dynamics and the chaotic behavior of atoms periodically kicked by the micro-electromagnet mirror.

Micro-electromagnet geometries can be easily varied and used for a variety of other manipulation schemes such as trapping and guiding. Micro-electromagnet guides, described in Chapter 2, and Chapter 3, have been successfully used to guide cold Cs atoms [Dekker N.H. *et al.*, 2000]. Recently, atomic beamsplitters [Mueller D. *et al.*, 2000; Folman R. *et al.*, 2000], and traps [Reichel J. *et al.*, 2000] have been demonstrated using microfabricated current-carrying wires.

The last two Chapters (Chapters 7 and 8) of this Thesis describe the theoretical and experimental work that can serve as a basis for future experiments.

In Chapter 7, we propose new, three-dimensional micro-electromagnets for manipulation of neutral particles with spin. We have fabricated three-dimensional micro-electromagnets using multiple steps of optical lithography and metal evaporation. The fabricated structures include three-dimensional quadrupole traps and guides, as well as an example of a three-dimensional trap fabricated on top of a micro-electromagnet mirror. Such devices can produce stronger magnetic field magnitudes, gradients, and curvatures and can be used to realize quantum wires and dots for atoms, more easily than with planar micro-electromagnets. An interesting direction would be to use coupled three-dimensional traps with an adjustable trap coupling, as described in Chapter 7, to entangle neutral atoms.

Micro-electromagnets can be also used to manipulate electrons, ions and polar molecules, because micro-electromagnets can carry electric currents as well as voltages to produce magnetic, as well as electric fields. The manipulation of polar molecules would be based on the electric-dipole interaction. Charged wires have been already used to confine atoms with electric-dipole moments [Sekatskii S.K. and Schmiedmayer

J.,1996], and electrostatic mirrors for polar molecules have been made from interdigitated electrodes [Wark S. J. and G. I. Opat, 1992].

In the last Chapter (Chapter 8), we proposed a method to trap electrons in vacuum using micro-electromagnet traps. A trapped electron could be considered as an 'artificial atom' in analogy to quantum dots in semiconductors. Electrons trapped in vacuum would potentially suffer less from interference from defects than quantum dots in semiconductors, and could permit the study of low-dimensional systems. We have described the theory of electron trapping based on Penning traps [Brown L.S. and Gabrielse G., 1986], and the experimental setup that could be used to integrate micro-electromagnet electron traps with electron sources and electron detectors. Even though there are several experimental issues to be surmounted in order to trap electrons, I find this work to be an exciting future direction.

References

Adams C.S., Sigel M., and Mlynek J. (1994), Phys. Rep. **240**, 143 and references therein.

American Institute of Physics Handbook (1982), ed. Gray D.E., (McGraw-Hill).

Atom Interferometry (1997), ed. Berman P., Academic Press.

Beenaker C.W.J. and van Houten, H. (1991), *Quantum Transport in Semiconductor Nanostructures*, Sol. State Phys. 44, eds. Ehrenreich H. and Turnbull D., Academic Press, San Diego, CA.

Bergeman T. *et al.* (1987), Phys. Rev. A. 35(4), 1535.

Brewer R.G., Devoe R.G., and Kallenbach R. (1992), Phys. Rev. A 46 (11), R6781.

Brodie I., Schwoebel P.R. (1994), Proc. of the IEEE 82, 1006.

Brown L.S and Gabrielse G. (1986), Rev. Mod. Phys. 58 (1), 233.

Cassettari D., Hessmo B., Folman R., Maier T., Schmiedmayer J. (2000), quant-ph/0003135.

Chern J.W.E. and Cheh H.Y. (1992), Chem. Eng. Comm. 114.

Chern J.W.E. and Cheh H.Y. (1996a), J. Electrochem. Soc. 143, 3139.

Chern J.W.E. and Cheh H.Y. (1996b), J. Electrochem. Soc. 143, 3144.

Cognet L., Savalli V., Featonby P., Westbrook N., Westbrool C., Helmerson K., Phillips W.D., Zabow G., Drndic M., Lee C.S., Westervelt R.M., Prentiss M. (1999), Europhys. Lett. 47 (5), 538.

Dekker N.H., Lee C.S., Lorent V., Thywissen J.H., Smith S.P., Drndic M., Westervelt R.M., Prentiss M. (2000), Phys. Rev. Lett. 84, 1124.

Devoe R.G., Brewer R.G. (1996), Phys. Rev. Lett. 76 (12).

Dowling J.P. and Gea-Banacloche J. (1996), Adv. At. Mol. Opt. Phys. **37**, 1.

Drndic M., Johnson K.S., Thywissen J.H., Westervelt R.M., Prentiss M. (1998), Appl. Phys. Lett. 72, 2906.

Drndic M., Zabow G., Lee C.S., Thywissen J.H., Johnson K.S., Prentiss M., Westervelt R.M., Featonby P.D., Savalli V., Cognet L., Helmerson K., Westbrook N., Westbrook C.I., Phillips W.D., Aspect A. (1999), Phys. Rev. A 60 (5), 4012.

Duncan D.S., Livermore C., Westervelt R.M., Maranowski K.D., Gossard A.C. (1999), Appl. Phys. Lett. 74 (7), 1045.

Dukovic J.O. (1993), IBM J. Res. Develop., 37 (2).

Ekstrom C.R., Keith D.W., and Pritchard D.E. (1992), Appl. Phys. B **54**, 369.

Electroplating Engineering Handbook (1994), ed. Durney L.J., Van Nostrand Reinhold, New York.

Field M., Smith C.G., Ritchie D.A., Frost J.E.F., Jones G.A.C., Hasko D.G. (1993), Phys. Rev. Lett. 70, 1311.

Folman R., Krüger P., Cassettari D., Hessmo B., Maier T., Schmiedmayer J. (1999), quant-ph/9912106.

Fundamentals of Electrochemical Deposition (1998), Paunovic M. and Schlesinger M., John Wiley & Sons, Inc. (1998).

Gradshteyn I.S., and Ryzhik I.M. (1994), *Table of Integrals, Series and Products*, ed. Jeffrey A., Fifth Edition, Academic Press.

Hazlebeck D.A. (1989), J. Electrochem. Soc. 136, C215.

Hazlebeck D.A. and Talbot J.B. (1991), J. Electrochem. Soc. 138,1998.

Hinds E.A., Hughes I.G (1999), J. Phys. D: Appl. Phys. 32, R119.

Hughes I.G., Barton P.A., Roach T.M., Boshier M.G., Hinds E.A. (1997a), J. Phys. B **30**, 647.

Hughes I.G., Barton P.A., Roach T.M., Boshier M.G., and Hinds E.A.(1997b), J.Phys.B **30**. 2119.

Jaksch D., Briegel H.J., Cirac J.I., Gardiner C.W., Zoller P. (1999), Phys. Rev. Lett. 82,1975.

Johnson K.S., Drndic M., Thywissen J.H., Zabow G., Westervelt R.M., Prentiss M. (1998), Phys. Rev. Lett. **81**, 1137.

Kaenders W.G., Lison F., Muller I., Richter A., Wynands R., and Meschede D. (1996), Phys. Rev. A **54**, 5067.

Killian T.C., Kulin S., Bergeson S.D., Orozco L.A., Orzel C., Rolston S.L. (1999), Phys. Rev. Lett. 83, 4776.

Klemperer O. (1953), *Electron Optics*, 2nd ed., Cambridge University Press.

Kondo K., T. Miyazaki T. and Tamura Y. (1994), J. Electrochem. Soc. 141, 1644.

Kondo K., Fukui K., Uno K. and Shinohara K. (1996), J. Electrochem. Soc. 143, 1880.

Kondo K., and Fukui K. (1998), J. Electrochem. Soc. 145, 3007.

Kong L., and Chou Y.S. (1997), Appl. Phys. Lett. 70 (15).

Landragin A., Labeyrie G., Henkel C., Kaiser R., Vansteenkiste N., Westbrook C.I., Aspect A. (1996), Opt. Lett. **21**, 1591.

Lau D.C., Sidorov A.I., Opat G.I., McLean R.J., Rowlands W.J., Hannaford P. (1999), Eur. Phys. J. D **5**. 193.

Lawall J. (1993). PhD Thesis, Harvard University.

Lawall J.and Prentiss M. (1994), Phys. Rev. Lett. **72**, 993.

Livermore C., Crouch C.H., Westervelt R.M., Campman K.L., Gossard A.C. (1996), Science 20. 1332.

Mackay K., Bonfim M., Givord D., Fontaine A. (2000), J. Appl. Phys. 87(4), 1996.

Mancini S., Martins A.M., and Tombesi P. (2000), Phys. Rev. A 6001 (1), 2303.

Materials at Low Temperatures (1983), eds. Reed R.P. and Clark A.F., American Society for metals, Metal Park, OH.

Mesoscopic Electron Transport (1996), eds. Sohn L.L., Kouwenhoven L.P., and Schon G., Kluwer Academic Publishers.

Metcalf H., van der Straten P. (1994), Phys. Rep. 244, 203.

Meschede M. *et al.* (1997) in *Atom Optics*, M. Prentiss and W.D. Phillips editors, SPIE Proc. **2995**.

Migdall A.L., Prodan J.V., Phillips W.D., Bergman T.H., and Metcalfe H.J. (1985), Phys. Rev. Lett. **54**, 2596.

Mueller D., Anderson D.Z., Grow R.J., Schwindt P.D.D., Cornell E.A. (1999), Phys. Rev. Lett. 83, 5194.

Mueller D., Cornell E.A., Prevedelli M., Schwindt P.D.D., Anderson D.Z. (2000), physics/0003091.

Nanev C., Mirkova L., Rashkov S., and Kaischev R. (1975), Electrodeposition and Surface Treatment 3, 179.

Nanostructures and Mesoscopic Systems, eds. Kirk W.P. and Reed M.A., Academic Press, Inc., San Diego, CA 92101.

Olson D.L, Peck T.L., Webb A.G., Magin R.L., Sweedler J.V. (1995), Science 270, 1967.

Opat G.I.,Wark S.J., and Cimmino A. (1992). Appl. Phys. B **54**, no. 5, 396.

Phillips W.D. (1998). Rev. Mod. Phys. 70, 721.

Proceedings from International Vacuum Microelectronics Conferences (IVMCs): 7th IVMC (1995). J. Vac. Sci. Technol. B 13, 402; 6th IVMC (1994), J. Vac. Sci. Technol. B 12, 628; 5th IVMC (1993), J. Vac. Sci. Technol. B 11, 351.

Reichel J., Hansell W., Hansch T.W. (1999), Phys. Rev. Lett. 83. 3398.

Rimberg A.J. (1993), PhD Thesis, Harvard University.

Roach T.M., Abele H., Boshier M.G., Grossman H.L., Zetie K.P. and Hinds E.A. (1995), Phys. Rev. Lett. **75**. 629.

Saba C.V., Barton P.A., Boshier M.G., Hughes I.G., Rosenbusch P., Sauer B.E., Hinds E.A. (1999). Phys. Rev. Lett. **82**. 468.

Schmiedmayer J. (1998), Eur. Phys. J. D 4, 57.

Schmidt W.U., Alkire R.C. and Gewirth A.A. (1996), J. Electrochem. Soc. 143, 3122.

Schwoebel P.R. and Brodie I. (1995), J. Vac.Sci. Technol. B 13(4).

Sekatskii S.K. and Schmiedmayer J. (1996). Europhys. Lett. 36 (6), 407.

Shenoy R.V., M. Datta M. and Romankiw L.T. (1996), J. Electrochem. Soc. 143, 2305.

Sidorov A.I., McLean R.J., Rowlands W.J., Lau D.C., Murphy J.E., Walkiewicz M., Opat G.I., and P. Hannaford P. (1996), Quant. Semiclass. Opt. **8**, 713.

Sidorov A.I., Lau D.C., Opat G.I., McLean R.J., Rowlands W.J., Hannaford P. (1998), Laser Phys. **8**, 642.

Spindt C.A. (1968), J. Appl. Phys. **39**, 3504.

Thywissen J.H., Olshanii M., Zabow G., Drndic M., Johnson K.S., Westervelt R.M., Prentiss M. (1999a), Eur. J. Phys. D 7 (3), 361.

Thywissen J.H., Westervelt R.M., Prentiss M. (1999b), Phys. Rev. Lett. 83, 3762.

Two-dimensional Electron Systems: on Helium and Other Cryogenic Substrates (1997), ed. E.Y.Andrei, Boston, Mass.: Kluwer Academic Publishers.

Van der Bijl. H.J. (1920), *The Thermionic Vacuum Tube and its Applications*, 1st ed., New York, McGraw-Hill book company, inc.

Van Wees B.J. *et al.* (1988), Phys. Rev. Lett. 60, 848.

Vernoy D.W. *et al.* (1998), Phys. Rev. A, 57(4), R2293.

Vladimirskii V.V. (1961), Sov. Phys. JETP **12**,740.

Wark S.J. and Opat G.I. (1992), J. Phys. B: At. Mol. Opt. Phys. **25**, 4229.

Weinstein J.D. and Libbrecht K.G. (1995), Phys. Rev. A 52 (5), 4004.

Zabow G., Drndic M., Thywissen J.H., Johnson K.S., Westervelt R.M., Prentiss M. (1999), Eur. Phys. J. D 7(3), 351.

APPENDICES

APPENDIX A

Magnetic Field Calculations (using Mathematica)

EXAMPLE 1:

```
(*Field from a quadrupole trap with two concentric coplanar rings with currents I1 and I2
and radii r1 and r2; the ratio I1/I2 and r1/r2 is chosen to optimize the trap depth*)
r1 = 1;
r2 = 2.66;
I1 = -1;
I2 = 1.87;
b = 0;

(*Calculating the z-component of the field*)
Bz[r_, z_] := 2*10^(-1)*I1/Sqrt[(r1 + r)^2 + z^2]*(EllipticK[4r*r1/((r + r1)^2 + z^2)] +
(r1^2 - r^2 - z^2)*EllipticE[4r*r1/((r + r1)^2 + z^2)]/((r1 - r)^2 + z^2))
 + 2*10^(-1)*I2/Sqrt[(r2 + r)^2 + (z + b)^2]*(EllipticK[4r*r2/((r + r2)^2 + (z + b)^2)]
+(r2^2 - r^2 - (z + b)^2)*EllipticE[4r*r2/((r + r2)^2 + (z + b)^2)]/((r2 - r)^2 + (z + b)^2));

(*Calculating the radial component of the field*)
Br[r_, z_] := 2*10^(-1)*I1*z/(Sqrt[(r1 + r)^2 + z^2]*r)*
(-EllipticK[4*r*r1/((r + r1)^2 + z^2)] +(r1^2 + r^2 + z^2)/((r1 - r)^2 +
z^2)*EllipticE[4r*r1/((r + r1)^2 + z^2)]) + 2*10^(-1)*I2*(z + b)/(Sqrt[(r2 + r)^2 + (z +
b)^2]*r)*(-EllipticK[4r*r2/((r + r2)^2 + (z + b)^2)] +
(r2^2 + r^2 + (z + b)^2)/((r2 - r)^2 + (z + b)^2)*EllipticE[4r*r2/((r + r2)^2 + (z + b)^2)]);

(*Total field magnitude*)
B[r, z] := Sqrt[(Bz[r, z])^2 + (Br[r, z])^2];

(*Contours of constant field magnitude above the trap in the zr plane*)
ContourPlot[Sqrt[(Bz[r, z])^2 + (Br[r, z])^2], {r, -3, 3}, {z, 0, 3}, ContourShading ->
False, PlotPoints -> 100, AspectRatio -> 0.5. ContourStyle -> Thickness[0.004],
Contours -> {0, 0.05, 0.1, 0.15, 0.2, 0.25, 0.3, 0.35, 0.45, 0.6, .75, 0.9, 1.05, 1.2, 1.35,
1.5, 1.75, 1.9, 2.05, 2.2, 2.35, 2.5},FrameTicks -> {{-4, -2, {-1, ""}, {-3, ""}, 0, {1, ""},
2, 4, {3, ""}}, {0, 1.00, 2, 3}, {{0, ""}, {-1, ""}, {-2, ""}, {-3, ""}, {-4, ""}, {0, ""},
{1,""}, {2, ""}, {3, ""}, {4, ""}}, {{0, ""}, {1.0, ""}, {2.0, ""}, {3, ""}}}];
```

EXAMPLE 2:

```
(*Field from a mirror with rectangular wire cross-sections*)

ClearAll[u, v, x, y, a, iterations, p, q, bp];
u = 0;
v = 0;
a = 50;
iterations = 40;

For[i = -iterations, i <= iterations, i++;
            u = 1000/30.625*(-1)^(i + 1)Integrate[(y -q)*((x - (i*a/2 - p))^2 +
              (y - q)^2)^(-1), {p, -35/4, 35/4}, {q, -0.0001, 3.5/2 - 0.0001}] + u;

            v = 1000/30.625*(-1)^(i)* Integrate[(x - (i*a/2 - p))/((x - (i*a/2 - p))^2 +
              (y - q)^2), {p. -35/4, 35/4}, {q, -0.0001, 3.5/2 - 0.0001}] + v;

      ];

bp = ContourPlot[Sqrt[u^2 + v^2], {x, 0, 125}, {y, -3, 48},
Contours -> {0.76, 0.99, 1.28, 1.67, 2.17, 2.82, 3.67, 4.77, 6.19, 8.05,
     10.47, 13.61, 17.7, 23, 30, 39, 50.7, 65.91, 85.68, 111.39, 144, 8},
  ContourShading -> False, PlotPoints -> 100, AspectRatio -> 1.1]
Show[bp, x{0, 10}];
```

APPENDIX B

Magnetic Force Microscopy of Micro-Electromagnets

Magnetic force microscopy (MFM) is a useful tool to characterize the magnetic field configurations above micron-scale objects. Standard atomic-force microscopes (AFMs) can be used to image magnetic fields by using magnetized cobalt tips and operating the AFM in the Tapping mode.

An MFM toolkit has been purchased to do MFM measurements with the atomic-force microscope from Park Scientific Instruments, on the second floor of McKay. This toolkit consists of a tip magnetizer, a non-magnetic sample holder, and a set of MFM ultra- or micro-levers. We have measured the MFM response above several micro-electromagnet mirrors. This data, as shown below, has only given us some qualitative information about the magnetic field. Calibrating the MFM signal and obtaining quantitative information is much more difficult [Kong L., and Chou Y.S., 1997]. The MFM signal should dominate over the topographic signal at distances of several hundred nanometers above the surface. When the MFM signal is measured at smaller heights, it will be convolved with the topographic signal.

Magnetic-force microcopy measurements of magnetic mirrors have been perfomed by [Hughes I.G. *et al.*,1997b] for a magnetized floppy disk mirror.

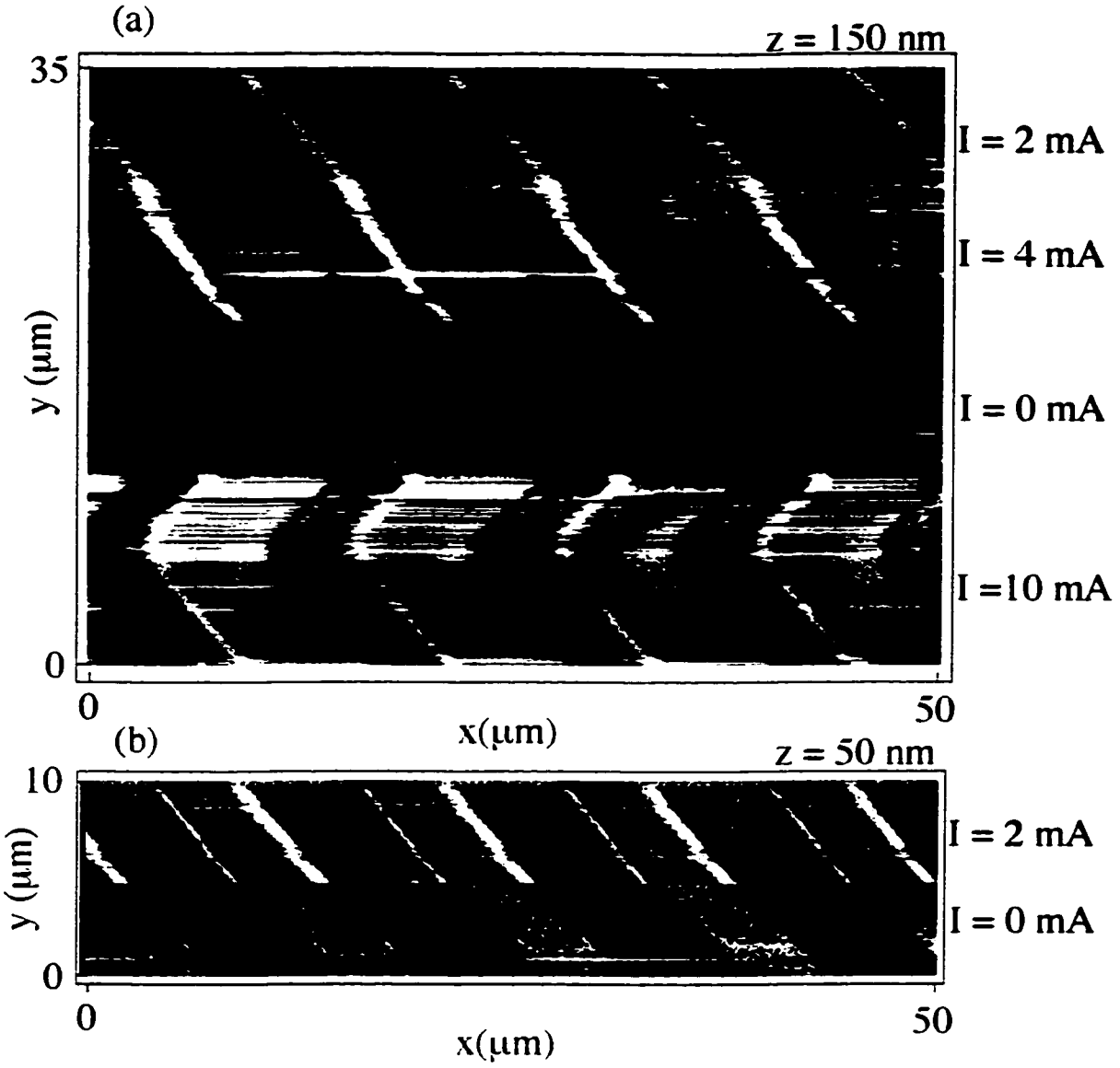

Fig. B.1 Magnetic force microscopic (MFM) signal measured above a micro-electromagnet mirror at distances z = 150 nm (a), and z = 50 nm (b) above the mirror surface. The mirror current I, was changed during the scannning, as indicated on the right axis. Mirror period a = 18 μm , wire width w = 3 μm , and wire height h = 0.3 μm.

The measured MFM signal is proportional to $\partial^2 B_z / \partial^2 z$ where z is the direction perpendicular to the surface that is being measured [see Hughes I.G. *et al.*,1997b; Kong L., and Chou Y.S., 1997]. At distances $z >> a/2\pi$ from the mirror surface, this signal should be a sinusoidal curve along the x-direction perpendicular to the mirror wires. On the other hand, close to the mirror surface, higher harmonics should be included.

Figure B.1 shows the MFM signal at a height z above the surface of the niobium micro-electromagnet mirror with period a = 18 μm , wire width w = 3 μm , and wire height h = 0.3 μm, for mirror currents from I = 0 to I = 10 mA, at heights z = 150 nm (a) and z = 50 nm (b) above the surface. As shown, the signal looks different for different currents in the mirror. Notice the white and black edges of the wires when the mirror current I is increased. These are the points where the curvatures $\partial^2 B_z / \partial^2 z$ are high, and low, respectively. Because this measurement is taken close to the surface, the signal consists of the MFM signal due to the magnetic interaction superimposed onto a topographic signal due to the Van der Walls interaction. That is why at I = 0 the MFM signal is similar to the topographic signal. At nonzero mirror currents I, the dominating MFM signal is very different from the topographic signal.

Using the MFM could be useful to gather a qualitative information about the magnetic field. However, for a more detailed quantitative analysis of the magnetic field, the MFM measurements seem too complicated, i.e. the signal is difficult to calibrate. A possible way to calibrate the MFM signal using small current-carrying wire loops has been described by [Kong L., and Chou Y.S., 1997].

APPENDIX C

Device Fabrication Procedure

- cleave the GaAs/AlGaAs wafer into small chips approximately 3 x 3 mm.

Fabrication of ohmic contacts:

- clean the chips in boiling TCE (T = 150 °C) on a hot plate for 10 minutes, in acetone with ultrasounding for 10 min, and in methanol with ultrasounding for 10 min.
- spin PMMA 496 K for 60 s at 5000 rpm, bake on a hot plate for 1 min at T = 180 °C;
- spin PMMA 960 K: apply it on the chip while spinning at slow speed ~ 100 rpm then after ~ 10s, move to 5000 rpm and spin for 60 s; bake on a hot plate for 1 min at T = 180 °C.
- spin one more layer of PMMA 960 K as described above.
- write Ohmic contacts and alignment markers using SEM.
- develop in PMMA developer for 30 s; stop the development in isopropanol; dry off.
- immerse chip in NH_4OH for 10 s to clean the GaAs/AlGaAs surface before evaporation.
- evaporate Ni (5 nm) /Au (5 nm)/ Ge (25 nm) /Au (40 nm) /Ni (10 nm) /Au (40 nm) in the thermal evaporator.
- lift in acetone.
- anneal the ohmic contacts in the thermal annealer in the nitrogen gas flow; ramp to 110 °C for 1 min, then to 250 °C for 40 s and then to 410 °C for 30 s.

Fabrication of etch trenches:

- clean the chips in boiling TCE (T = 150 °C) on a hot plate for 10 minutes, in acetone (no ultrasound) for 10 min, and in methanol (no ultrasound) for 10 min.

- spin two layers of PMMA 960 K for 60 s at 5000 rpm, bake on a hot plate for 1 min at T = 180°C; the second layer is spun as described for the ohmic contact fabrication.
- Write etch trenches with SEM; use alignment markers to align.
- develop in PMMA developer for 30 s; stop the development in isopropanol; dry off.
- immerse chip in NH_4OH for 10 s to clean the GaAs/AlGaAs surface before evaporation.
- etch in the ion miller for 30 s: this etches 40 nm below the surface.
- lift in acetone.

Fabrication of electron trap rings and gates:

- clean the chips in boiling TCE (T = 150 °C) on a hot plate for 10 minutes, in acetone (no ultrasound) for 10 min, and in methanol (no ultrasound) for 10 min.
- spin two layers of PMMA 960 K for 60 s at 5000 rpm, bake on a hot plate for 1 min at T = 180°C; the second layer is spun as described for the ohmic contact fabrication.
- write trap rings and gates with SEM; use alignment markers to align.
- develop in PMMA developer for 30 s; stop the development in isopropanol; dry off.
- immerse chip in NH_4OH for 10 s to clean the GaAs/AlGaAs surface before evaporation.
- evaporate Cr (10 nm) /Au (90 nm) or other desired Au thickness in the thermal evaporator.
- lift in acetone.

Wire bonding:

- place chip on a copper sample mount made for the experiment.
- place sample mount in a stainless steel jig made for fitting the sample mount in the wirebonder.

- make sure the bonding pads are grounded during bonding; ground yourself with a grounding strip to the wire bonder.
- wire bond at T ~ 80 °C.